TROPOSPHERIC CORRECTION FOR LONG-RANGE HIGH PRECISION GNSS POSITIONING WITH REGIONAL NUMERICAL WEATHER PREDICTION MODELS

MIN LIU

Ph.D

The Hong Kong Polytechnic University

2018

The Hong Kong Polytechnic University

The department of Land Surveying and Geo-Informatics

Tropospheric Correction for Long-Range High Precision GNSS Positioning with Regional Numerical Weather Prediction Models

Min Liu

A Thesis Submitted in Partial Fulfillment of the

Requirements for the Degree of Doctor of Philosophy

January 2016

CERTIFICATE OF ORIGINALITY

I hereby declare that this thesis is my own work and that, to the best of my knowledge and belief, it reproduces no material previously published or written, nor material that has been accepted for the award of any other degree or diploma, except where due acknowledgement has been made in the text.

_____(Signed)

Min Liu (Name of student)

ABSTRACT

Static positioning, Precise Point Positioning (PPP) and Real-Time-Kinematic (RTK) positioning are three main high-precision positioning techniques used for Global Navigation Satellite Systems (GNSS). As current models for tropospheric delays are not accurate, sufficient long observation time is required by static positioning and PPP to estimate tropospheric delay parameters directly from GNSS observation, and network-based RTK is normally limited to tens of km for the interpolation of tropospheric delays from reference stations. In this research, we try to use regional Numerical Weather Prediction (NWP) models, the meteorological (MET) data from ground, and GNSS real-time tropospheric delays estimated at reference station to generate tropospheric correct model for precise positioning for PPP and network RTK with long baseline separation (i.e. 200-300 km). In this way, we can significantly improve GNSS positioning efficiency and the cost of network RTK for wide area coverage.

Firstly, the accuracy of tropospheric delays derived from a regional NWP model is evaluated using long-term GNSS and Radiosonde data in East China region. A new Fast and Accurate Iterated Ray Tracing (FAIRT) algorithm is developed to estimate the tropospheric delays along with the GPS signal path from the NWP model. As a by-product, the precision of the tropospheric delay mapping functions are also evaluated. In general, the NWP derived tropospheric delays agree with GPS and MET data derived delays, with the accuracy of 20 mm. The accuracy of the tropospheric delays is better in dry seasons than that in wet seasons. Using real-time wet pressure observations on the ground and GNSS derived tropospheric delays at reference stations, the tropospheric delay estimation can be further improved with a new data assimilation method developed in this study.

The tropospheric delay models developed in this study is also evaluated by applying them to GNSS positioning. With the model, GNSS positioning accuracy of centimeter and decimeter level can be achieved in horizontal and vertical components respectively. To further improve positioning accuracy, the NWP derived tropospheric model is used as initial value and a new tropospheric search algorithm is proposed to improve GNSS positioning convergence time.

ACKNOWLEDGMENTS

I would like to thank my chief supervisor, Professor Wu Chen, for his continued guidance and support during my studies.

Special thanks to Professor Haojian Yan and Dr. Peng Guo of Shanghai Astronomy Observation, Professor Congwei Hu of Tongji University, for their constant supports and many fruitful discussions.

Thanks also go to my colleagues and friends. In particular, I deepest appreciate Dr.Ying Xu, Dr. Qiong Ding, Dr. Duojie Weng, Dr. Shengyue Ji and Dr. Chisheng Wang for their assistance in school studies.

Finally, very special thanks go to my parents and husband for their unconditional support, concern and understanding through my Ph. D studies.

TABLE OF CONTENTS

LIST OF FIGURES

LIST OF TABLES

Chapter 1 Introduction

1.1 Research Background

The Global Positioning System (GPS) is the first navigation system developed by the United States (US), which was followed by other systems, such as the Russian GLONASS and Chinese Beidou systems. In past decades, with the development of satellite techniques and computers, significant improvements have been achieved in positioning accuracy, operation efficiency and cost (Boucher, 1994; Zamberge, 1993; 1995a; 1995b; Teunissen, 1996; Ashkenazi, 2006, European Space Agency, 2005c). For high precision applications, different positioning techniques have been developed, for example, the static positioning with double-differenced phase data is used to achieve millimeter (mm) level products; the Precise Point Positioning (PPP) technique supported by highly accurate orbit and clock products to achieve centimeter level accuracy; and the real-time-kinematic (RTK) systems for some time-critical applications, such as engineering surveying (Rizos, 2007; Zou et al., 2013; Li et al., 2014).

The error sources of GNSS positioning include orbit error, the ionospheric effect, the tropospheric effect, and the multi-path error (Kouba et al., 2001; Chen et al., 2009). As the satellite orbit can be well predicted and ionospheric effects can be eliminated with the ionosphere free combination, the main challenge in GNSS data processing is how to further reduce the tropospheric delay and the multi-path errors (Yao et al., 2017). If the tropospheric delay error can be significantly reduced, the ambiguities will be resolved faster, and the convergence period during GNSS data processing will decrease significantly (Gao and Shen, 2001; Heroux, 2004; Xu, 2017).

To achieve high precision (i.e., cm level or above), tropospheric corrections are normally estimated together with other unknown parameters in the static positioning mode. However, to obtain precise tropospheric delay estimation, long observation time (i.e. 2 hours) is needed. In the PPP technique where non-differential observations is used, all errors affecting GNSS measurements need to be taken account, including the tropospheric effect and GNSS satellites related errors. With current PPP processing method, the positioning accuracy is lightly lower than the static positioning mode and the convergence time for data processing is more than 30 minutes (Heroux, 2004, Chen et al., 2009). For higher precision and less observation time, network corrections are used to improve the performance of PPP to achieve real-time PPP (Li et al., 2011; Zou et al., 2013; Li et al., 2014). RTK positioning uses a differential technique between the reference and the roving receivers to achieve a higher accuracy. Common errors for these two receivers can be cancelled out through the differential process. However, as the correlations of tropospheric delays are normally within the distances of a few tens kilometers, a quite dense reference network is required for this positioning mode, which makes it very expensive for large area coverage, i.e. for a whole continent (Rizos, 2006; Zou et al., 2013; Li et al., 2015).

In recent years, Continuously Operating Reference Station (CORS) networks have been established at the global and regional level (Rizos, 2007; Shen et al., 2013; Nardo, et al. 2014; Li et al., 2015) to provide better services for GNSS applications. In China, CORS networks have been established since 1992. The crustal movement observation network of China was established in 2012 which includes 260 stations (www.neiscn.org). Up to 2016, there were 360 stations for the national CORS networks in China (Chen et al., 2016). The national CORS networks are also established in other countries, with more than 100 continuously operating stations in Germany and approximately 1200 stations for the GEONET in Japan (Li, 2014). In addition, many regional CORS networks

have been established in many cities in China, such as Beijing, Shanghai, and Hong Kong. In Hong Kong, the spatial resolution of the CORS network (SatRef) is 10-15 km, and it is dense enough for real-time PPP and regional RTK positioning (Li, 2014). However, the average spatial resolution of a regional CORS network is 40-70 km, and the resolution is much lower in the western China area. Moreover, there is no CORS network in some areas, such as Tibet (data from the National Geomatics Center of China, 2017).

Thus, if we can provide high precision tropospheric delay models to cover wide areas (i.e. the whole China), the number of reference stations in the regional coverage CORS network can be significantly reduced. For example, if we can extend the baselines of CORS reference stations from 100 km to 300 km, only one ninth of GNSS reference stations are required, compared with the existing CORS network. Moreover, the high precision tropospheric models can also be used in PPP processing to significantly reduce the observation time for convergence (Alber, 1997; Chen, 1997; Kouba, 2001; Rizos, 2007).

1.2 Objectives and Contributions

The aim of the research is to develop high precision tropospheric delay models for wide area coverage (i.e. 300-500 km) through the integration of latest NWP models, real-time tropospheric estimation from GNSS reference stations, and surface meteorological measurements. To achieve this, three main objectives are given as follows:

- **To evaluate tropospheric delay correction accuracy using the latest NWP models**

  Many empirical and semi-empirical models have been developed for tropospheric corrections. Widely used models include the Saastamoinen,

EGNOS and Black and UNB3 models, among others (Hopfield, 1971; Saastamoinen, 1973; Collins, 1999; Mendes, 1999). Marini (1972) was the first to develop and describe the tropospheric delay with the zenith total delay (ZTD) and mapping function (Yan, 2000). For empirical and semi-empirical tropospheric models, errors in the ZTD from models were approximately 1 decimeter (Mendes 1999; Wang, 2009) which are not accurate enough to support GNSS centimeter level positioning. On the other hand, NWP models have been widely used for weather forecasting and the accuracy is getting higher. In this study, we will firstly evaluate tropospheric delay accuracy from the latest NWP model in East China region through the comparison with GNSS and Radiosonde observation in the region. To obtain tropospheric delay along all GNSS signal paths requires intensive ray tracing computation. For the applications on GNSS data processing, more efficient ray tracking algorithms will be developed to support real-time operation of GNSS positioning.

- **To assimilate GNSS/NWP data to further improve tropospheric delay accuracy**

It has been demonstrated that the integrated Zenith Total Delay (ZTD) based on the NWP models is more accurate than the empirical tropospheric models (Boccolari, 2006; Nievinski, 2005). Regional NWP models with a 0.3 ° resolution are used to integrate the ZTD for 41 GPS stations over six months and the results show a clear seasonal change that has higher scattering during the summer (Haase et al., 2000). A similar experiment was performed in Finland over 4 days in 2006, where NWP models with a 1 ° resolution were used, and the RMSE of the integrated ZTD was approximately 50 mm (Andrei et al., 2007). In the previous research, the integrated delays were either not analyzed long enough, or

the precision of the integrated delays was not good enough. The reliability and applicability of the integrated delays were not analyzed either. In this study, based on long term (one year) data analysis, we will analyze the NWP-ZTD in different seasons and the causes of errors. Then NWP derived tropospheric delays will be further integrate ground meteorological data and GNSS derived tropospheric delays at reference station to generate an improved tropospheric delay model for regional coverage.

- **To assess the improvement of GNSS positioning accuracy and ambiguity convergence time with better tropospheric delays**

The use of 3-D meteorological data provided by the NWP models can be more effective for estimating tropospheric delay than surface meteorological data (Vedel et al., 2001; Gutman and Benjamin, 2001; Jensen, 2002). The NWP models can be directly used to reduce tropospheric delay residuals to improve ambiguity resolution (AR) and positioning accuracy (Alves et al., 2004; Ahn et al., 2006; Monico et al., 2006). Recent studies show that with baselines of hundreds of kilometers, residual tropospheric delay errors at the zenith angle can be as small as 1 to 2 cm after correction with the NWP models and double differencing (Jensen et al., 2002; Nievinski et al., 2005; Santos et al., 2005; Boccolari et al., 2006). This clearly demonstrates the potential for direct corrections of tropospheric residuals using the NWP models to enhance AR. The improved integrated delays from NWP models are used with high accuracy GPS positioning for long range RTK positioning to evaluate the performance improvement with the new tropospheric models developed in this study.

1.3 Thesis outline

The rest part of the dissertation is organized as follows:

In Chapter 2, all major GNSS systems and their development are reviewed. Various high precision positioning techniques and error correction methods for GNSS data processing are also summarized in this chapter.

The troposphere and its characteristics are briefly described in Chapter 3. Various atmospheric and tropospheric delay models are introduced and evaluated in the chapter.

In Chapter 4, a new ray tracing algorithm (FAIRT) for tropospheric correction based NWP model is proposed. The advantages of the algorithm are discussed, and the accuracy of the algorithm is evaluated as well.

The evaluation results of NWP based ZTD accuracy are given in Chapter 5. The errors of NWP-ZTD are analyzed in details. New methods are proposed to further improve the accuracy of NWP derived ZTD through GNSS observations and ground meteorological (MET) data.

In Chapter 6, the new ZTD models developed in this study will be evaluated through GNSS positioning processing, such as positioning accuracy and the ambiguity resolution convergence time.

The conclusions and recommendations for future work are presented in Chapter 7.

Chapter 2 The GNSS System and positioning techniques

The Global Navigation Satellite System (GNSS) is a system using to provide high precision positioning, navigation and time service. As of 2017, there are four main systems, including US's Global Positioning System (GPS), Russian GLONASS, EU's Galileo and Chinese BeiDou Navigation Satellite System (BDS). The GPS and GLONASS are fully operational, while Galileo is not. And China is in the process of expanding the BDS to global by 2020. Other systems are developed for regional navigation, such as Indian and Japanese navigation system. In this chapter, we review the development of the main navigation systems and high precision positioning techniques (Shaw, 2005; Falcone, 2006; Januszewski, 2009; Wei et al, 2017).

2.1 GNSS system

2.1.1 GPS systems

The GPS consists of 24 satellites, distributed in six orbital planes about the globe. Each satellite orbit is nearly circular, with an inclination of ~55 °, a period of 11h 58m (half sidereal days) and an altitude of about 20,200 km. This orbit configuration insures that at least four (and often much more) satellites are visible at any time, at any position on the Earth in the condition of open sky view. The observed simultaneously four or more satellites insure a reasonable configuration to measure position with three freedom degrees and time. For GPS constellation orbit, the repeat period keeps a constant of about 23h 56m (a sidereal day) (Hofmann-Wellenhof et al., 2001; 2003).

The first GPS satellite, PRN 4, was launched on 22 February 1978. PRN 4 belongs to the so-called Block I satellites. The orbital planes of the Block I

satellites have an inclination of about 63 degrees with respect to the Earth's equator. In February 1989 the first Block II satellite was launched. The Block II satellites were arranged in six orbital planes separated by about 60 ° on the equator, and inclined by about 55 °with respect to the Earth equator (Shaw, 2005; Hein et al. 2006a; 2006b). The Block II satellite launched in 1989 was arranged as the first formal operational satellite. There are two operational capabilities for GPS constellation: the initial operational capability (IOC) and the full operational capability (FOC). IOC was attained in 1993, when 24 (Block I/II/IIA) GPS satellites were operating and were available for navigation. FOC was achieved when 24 Block II and Block IIA satellites were available in 1994 (Prasad et al., 2005; Hofmann-Wellenhof et al., 2008).

For a better applicability, a higher accuracy, and a strong competition with other GNSS systems, the GPS modernization program has done since 1999. The first Block IIR-M (M, modernized) satellite was launched on September 25, 2005. The characteristic features of this satellite class are the new GPS civil L2C-code on the L2 frequency, and the new military M-code on L1 and L2 (Prasad et al., 2005; Hothem, 2006). After Block IIR-M, the new generation satellites Block IIF were launched in 2008, which are added with the third civil signal designated as named L5C-code, as well as with two military M-code signals. The satellite Block IIF-12 was launched in February 2016, and the satellites of IIA series were replaced. The satellite Block IIF-12 is last one of Block IIF series and next satellite will be launched for next generation satellites.

The next generation satellites are so called Block III satellites, which may be available in 2030s (Shaw 2005). It will need a substantial redesign of the system architecture , which might accommodate GLONASS- and Galileo-like three-plane constellation, observe simultaneously with about 27 to 33 satellites, (inclination of about 55 °, and an altitude of 20,196 km). The fourth civil signal

L1C will be provided in the near future, which will not replace the C/A-code for the backward compatibility reasons. And the M-code signal with the higher power will be provide to improve the resistance against interference for military requirements (Prasad et al., 2005; Hothem, 2006). The highlights of GPS III involve the characteristics of anti-jamming capabilities, improved system security, higher accuracy and reliability. In addition, integrity (also one of the European key arguments to claim for Galileo) will be a remarkable new property compared to the existing satellite system. And the first GPS III satellite is expected to be launched not before 2020 (www.insidegnss.com).

While the new generation system is developed, the civil signals are also expanded for the better GPS service, including bands L2C, L5 and L1C. The civil signals are not introduced too much in the thesis, and the two basic carrier signals and their combination are given as follow:

- GPS Signals and observations

Each GPS satellite continuously transmits right-hand circularly polarized carrier signals at two L band frequencies, which is for normal geodetic applications, f_1 = 1575.42 MHz (L1) and f_2 = 1227.60 MHz (L2), corresponding to wavelengths of 19.0 cm and 24.4 cm, respectively. These signals are modulated by a frequency of 10.23 MHz known as pseudo-random precision ranging code (P- code). The L1 carrier signal is also modulated by a frequency of 1.023 MHz known as coarse/acquisition (C/A) ranging code. The received L1 and L2 carrier signals $S_{L1}(t)$ and $S_{L2}(t)$ transmitted from each GPS satellite can be written as (Spilker, 1996a; 1996b):

$$S_{L1}(t) = \sqrt{2C_{c/A}}D(t)X(t)\sin(2\pi f_1 t + \theta_1) + \sqrt{2C_{P1}}D(t)P(t)\cos(2\pi f_1 t + \theta_1) \quad (2.1.1)$$

$$S_{L2}(t) = \sqrt{2C_{P2}}D(t)P(t)\cos(2\pi f_2 t + \theta_2) \quad (2.1.2)$$

in which

$C_{C/A}$, C_{P_1}: the received power of the in-phase and quadrature components of the L1 signal, respectively;

C_{P_2}: the received power of L2;

$D(t)$: an amplitude modulation for L1 and L2 containing navigation data;

$X(t)$: a pseudo-random sequence of L1, known as clear acquisition or C/A code-modulating the in-phase component of L1 at a rate of 1.023 MHz;

$P(t)$: a pseudo-random sequence of L1 and L2, known as P-code-modulating the quadrature component of L1 and L2 at a rate of 10.23 MHz;

$\theta_i (i = 1, 2)$: the initial phase for L1 and L2 carriers at epoch $t = 0$.

The pseudorandom code observations (C/A, P1, and P2) can be directly used to make the pseudo-range measurements. It is the travel time measurement between the satellite and the receiver, which typically has a precision of the orders of about 10 meters for C/A code and of about 1 meter for P-code, or better. In addition, the two carrier frequencies (L1 and L2) can be used to make the phase measurements, which has a measurement precision of the order of 1~2 mm (Braun, 2004). The signals of L-band frequency are tracked in atmospheric condition, which makes GPS an all-time instrument. But the received signals are delayed and bent according to the refractive index distribution of the atmosphere and the observational elevations. It will be discussed in details in Chapter 3.

- Linear Combinations of Observables

The structure of the Earth ionosphere has quick variations with observation time and locations of stations. Therefore it is rather difficult to model and estimate the refractions from the ionosphere. Owing to the dispersion of the ionosphere, the combination of the carrier frequencies is commonly adopted to remove or weaken the influence from the Earth ionospheric refraction.

Under the assumptions of that the split between the signal paths of L1 and L2 carriers can be ignored in the ionospheric propagations and of that the terms higher than the quadratic are also omitted, some particular linear combinations of the carrier phases and/or code measurements are used for either zero- or double-difference measurements in applications of satellite geodesy, geosciences and atmospheric inversion (Beutler et al., 2007).

Some linear combinations of carrier phases are listed as follows:

a. Ionosphere-Free Linear Combinations

Double frequency combination is often called "ionosphere-free linear combination" because the ionospheric path delay is virtually eliminated. The corresponding combinations of phase L_3 and code measurements P_3 are written as:

$$L_3 = \frac{1}{f_1^2 - f_2^2}(f_1^2 L_1 - f_2^2 L_2)$$

and

$$P_3 = \frac{1}{f_1^2 - f_2^2}(f_1^2 P_1 - f_2^2 P_2) \qquad (2.1.3)$$

in which f_1 and f_2 are the frequencies of two basic carrier signals L1and L2, respectively, L_1 and L_2 are their phase observables, P_1 and P_2 are the corresponding code observables.

One of the disadvantages of above linear combination is that the noise from the L1 and L2 carrier phase combination measurements is enlarged when it is used in geodetic and atmospheric inverse applications. For a network stations with short distance the ionospheric refractive effects can be fairly eliminated through the iono-free linear combination (Braun, 2004).

b. Geometry-Free Linear Combination L_4

The geometry-free linear combination phase measurement L_4 is defined as that, it is independent of receiver clock, satellite clock, tropospheric delay, and geometry (satellite orbits, station coordinates), and it only contains the differences of the ionospheric delays and of the initial phase ambiguities for two carrier signals. The corresponding combination of the phases L_4 is simply written as:

$$L_4 = L_1 - L_2 \tag{2.1.4}$$

The geometry-free linear combination is commonly used to estimate global and regional high-resolution ionospheric models (Rocken et al., 2000).

c. Wide-Lane Linear Combination L_5

The wide-lane linear combination L_5 is used in the double-difference phase measurements, which is to fix the cycle slips and to resolve their integer ambiguities. The corresponding combination L_5 of the phase measurements is represented as:

$$L_5 = \frac{1}{f_1 - f_2}(f_1 L_1 - f_2 L_2) \tag{2.1.5}$$

The combined wavelength of the phase measurements L_5 is 84 cm, which can simplify ambiguity resolution procession. The wide-lane linear combination is widely used in the analysis of the station coordination determinations, which are separated by more than a few tens of km (Beutler et al., 2007).

d. Melbourne-Wübbena Linear Combination L_6

Melbourne-Wübbena linear combination L_6 is a linear combination of both the basic carrier phase (L_1 and L_2) and the code observations (P_1 and P_2), and it eliminates the effects from the ionosphere, the geometry, the clocks, and the troposphere (Wübbena, 1985; Melbourne, 1985). The corresponding combination measurement L_6 is written as:

$$L_6 = \frac{1}{f_1 - f_2}(f_1 L_1 - f_2 L_2) - \frac{1}{f_1 + f_2}(f_1 P_1 - f_2 P_2) \tag{2.1.6}$$

2.1.2 GLONASS systems

GLONASS is a global satellite navigation system by Russia, which provides a real time position and velocity determination for military and civilian users. The satellites are located in middle circular orbit at 19,100 km altitude with a 64.8 degree inclination and a period of 11 hours and 15 minutes. GLONASS' orbit makes it to be especially suited for usage in northern latitudes, where getting a GPS signal can be problematic. The GLONASS constellation operates in three orbital planes, with 8 evenly spaced satellites on each orbit plane. A fully

operational constellation with a global coverage consists of 24 satellites, while 18 satellites are necessary for covering the territory of Russia. Over the three decades of development, the satellite designs have gone through numerous improvements, and can be divided into three generations: the original GLONASS (since 1982), GLONASS-M (since 2003) and GLONASS-K (since 2011) (Januszewski, 2009; R Dach et al, 2011).

GLONASS satellites transmit two types of signal: a standard precision (SP) signal and an obfuscated high precision (HP) signal. The HP signal is broadcast in phase quadrature with the SP signal, effectively sharing the same carrier wave as the SP signal, but with a ten times higher bandwidth than the SP signal. According Russian System of Differential Correction and Monitoring's data, as of 2010, precisions of GLONASS navigation definitions for latitude and longitude were 4.46 and 8.38 m, respectively, while the same time precisions of GPS navigation definitions were 2.00-8.76 m. Civilian GLONASS used alone is therefore very slightly less accurate than GPS. On northern latitudes, GLONASS' accuracy is better than that of GPS due to the orbital position of the satellites.

2.1.3 GALILEO systems

GALILEO is a navigation system currently being built by the EU and European Space Agency (ESA). One of the political aims with GALILEO is to provide a high-accuracy positioning system, upon which European nations can rely independent from the Russian GLONASS and US GPS systems, which can be disabled for commercial users in times of war or conflict. The GALILEO consists of 30 satellites (including 3 spares), distributed in three orbital planes, with an inclination of ~56 ° and an altitude of 23,222 km(European Space Agency, 2005c). The first experimental satellite, GIOVE-A, was launched in 2005 and was followed by a second test satellite, GIOVE-B, launched in 2008.

The first four operational satellites for navigation were launched in 2011 and once this In-Orbit Validation (IOV) phase had been completed, additional satellites were launched in the following five years. As of 2017, the Galileo system includes 18 satellites (total 30 satellites in plan), and it is expected to fully operated in 2020 (www.insidegnss.com).

The GALILEO navigation system is intended to provide measurements down to the meter range as a free service including the height above sea level, and to reach better positioning services at high latitudes compared to GPS and GLONASS. As a further feature, GALILEO will provide a global Search and Rescue (SAR) function. To do so, each GALILEO satellite will be equipped with a transponder, which is able to transfer the distress signals from the user's transmitter to the Rescue Co-ordination Centre, which will then initiate the rescue operation. At the same time, the system will provide a signal to the user, informing him that his situation has been detected and that help is on the way. This latter feature is new and is considered a major upgrade compared to the existing GPS and GLONASS navigation systems, which do not provide feedback to the user. The use of basic (low-accuracy) Galileo services will be free and open to everyone worldwide. The high-accuracy capabilities will be available for paying commercial users and for military uses (European Space Agency, 2006; Falcone, 2006).

2.1.4 BDS systems

The BDS systems are developed by three steps: the first generation is a two-way ranging regional system, named beidou-1, and has been realized in 2003 (Bian et al., 2005); the second is named Beidou-2, referred to as Compass. It is a regional navigation system that has been realized for Asian-Pacific region in the end of the year 2012; the third is named Beidou-3, it will be expanded to a global system around 2020. (www.beidou.gov.cn).

The finally system of BDS will be a constellation with 35 satellites, which include 5 GEO-stationary orbit (GEO) satellites, 27 Medium Earth Orbit (MEO) satellites and 3 Inclined Geosynchronous Satellite Orbit (IGSO) satellites, that will offer a complete coverage for the global utilities. The MEO satellites will have an average satellite altitude of 21,500 km. A number of 24 satellites will be evenly distributed in 3 orbital planes with an inclination angle of 55 °. The additional satellites are presumably spare ones. The IGSO satellites have a satellite altitude of 35 785 km, and the inclination angle corresponding to 55 ° (Tang, 2013).

Frequencies of BDS are allocated in three bands: B1, B2 and B3. B1 signal uses modulation with 4.092 megahertz bandwidth centered at 1561.098 MHz, while B2 signal is at1207.14 MHz and B3 is at 1268.52 MHz. As same as with other GNSS systems, BDS will supply two levels of positioning service: the open and the restricted (military) (Han et al., 2017). The civilian open service of Beidou-2 is designed to be provided a position accuracy about 10m, a velocity accuracy about 0.2m/s, and a timing accuracy about 50 ns (Ji et al., 2014; Xu, 2017).

The first MEO satellite of BDS has been launched on April 14, 2007. And it started to transmit navigation signals in three frequencies after few days later. At the end of 2017, 16 satellites had been launched for navigation system and 14 of them worked for the Beidou-2 (5 GEO, 5 IGSO and 4 MEO satellites) (Tang, 2013). The first two BeiDou-3 satellites were launched in November 2017, and they loaded the new accurate rubidium atomic clocks. It will improve the positioning accuracy of the BeiDou-3 to 2.5 to 5 meters. 18 new satellites will be launched before the end of 2018, and more than 30 satellites will be launched for Beidou-3 before 2020. It will expand the BDS system to global coverage (Wei et al., 2017; www.beidou.gov.cn).

2.2 High precision positioning techniques

Four main navigation systems were introduced in the former section, where the GPS system is the first fully operational system. Many high precision positioning techniques are developed based on GPS, including Precise Point Positioning (PPP), Real-Time Kinematics (RTK), kinematic PPP and static positioning. Static positioning uses observations that are more than 2 hours long, and the tropospheric correction is solved together with those coordinates; this will not be discussed in this Chapter. Other positioning techniques increasingly affected by the troposphere will be discussed then (Kleusberg, 1990; Witchayangkoon, 2000; Rizos, 2006).

2.2.1 Precise Point Positioning (PPP)

PPP technique uses a non-differential observation mode, which processes observation data from a single station to obtain the station positions with centimeter precision. As opposed to difference applications, the satellite clock corrections are not estimated in PPP but assumed to be known with some other parameters such as orbit information and EOPs. The parameters to be estimated in PPP are the station clock corrections and the station coordinates. Therefore, it seems that the combination of precise GPS orbits and clocks is essential for PPP weighted according to their corresponding accuracies. In fact, PPP takes an advantage of the application of the highly accurate global reference frame through the IGS orbit products (the satellite orbit error is better than 5cm, and clock error is better than 0.1ns) (Kouba et al.,1995; Zumberge et al., 1997).

PPP technique does not need to acquire the simultaneous tracking data from a network of stations. That makes easy to collect the observation data, and has no limitation of the baseline, and reduces the computation burden for applications. PPP can be not only widely used in the crustal deformation monitoring, and in

the near real-time GPS meteorology and orbit determination of low Earth orbiting (LEO) satellites, but also applied in the precise positioning of mobile objects. PPP becomes an important tool while the more and more dense networks are deployed for the regional seismic activity and the meteorological monitoring (Ge et al., 2008).

PPP algorism is first developed by the Zumberge et al. (1997) in the Jet Propulsion Laboratory (JPL), and added to their software GIPSY. They first determine precise GPS satellite positions and clock corrections from a globally distributed network of GPS receivers. Then data from the local network are analyzed by estimating receiver specific parameters with receiver-specific data; satellite parameters are held fixed at their values determined in the global solution. Muellerschoen (2001) uses the PPP for the global real-time positioning, with non-differential carrier phase based observations, and the accuracy is 10-20 cm in horizontal coordinates. Gao et al. (2002) develop a new method for the Carrier Phase Based PPP, using the P1-P2-CP model. The model uses the combination of the carrier phase and code to eliminate the ionosphere effect, which is different from the traditional IF combination. They also develop the commercial software of PPP, named P3. Zhang (2006) develops the software for the PPP, named Tri-P. He selects the data from aviation Lidar for near 4 hours, 1s-tracking, and uses the Tri-P to get the position of airplane, the RMSE of the 3D coordinates is better than 2.5 cm. The same way is used for a static station, and the RMSE is better than 1.5 cm. Li et al. (2011) first mentioned that the CORS could be used to improve the performance of PPP. It used the CORS based network to derive atmospheric errors and other GNSS errors in real-time, and it improved the positioning accuracy of PPP (Li et al., 2011; Zou et al., 2013; Li et al., 2014).

- Precise Point Positioning Observation Equations

The ionospheric-free combinations of dual-frequency GPS pseudo-range (P) and carrier-phase observations (Φ) are related to user position, clock, troposphere and ambiguity parameters according to the following simplified observation equations:

$$\ell_P = \rho + c(\mathrm{d}t - \mathrm{d}T) + T_r + \varepsilon_P \tag{2.2.1}$$

$$\ell_\Phi = \rho + c(\mathrm{d}t - \mathrm{d}T) + T_r + N\lambda + \varepsilon_\Phi \tag{2.2.2}$$

where, ℓ_P is the ionosphere-free combination of L1 and L2 pseudo-ranges, ℓ_Φ is the ionosphere-free combination of L1 and L2 carrier-phases, $\mathrm{d}t$ is the station clock offset from GPS time, $\mathrm{d}T$ is the satellite clock offset from GPS time, c is the vacuum speed of light, T_r is the signal path delay due to the neutral-atmosphere (primarily the troposphere), λ is the carrier, or carrier-combination, wavelength, N is the ambiguity of the carrier-phase ionosphere-free combination, ε_P and ε_Φ are the relevant measurement noise components, including multi-path.

Symbol ρ is the geometrical range computed as a function of satellite (Xs, Ys, Zs) and station (x, y, z) coordinates according to:

$$\rho = \sqrt{(Xs - x)^2 + (Ys - y)^2 + (Zs - z)^2} \tag{2.2.3}$$

Expressing the tropospheric path delay (T_r) as a function of the zenith path delay (zpd) and mapping function (M) and removing the known satellite clocks ($\mathrm{d}T$) gives the following mathematical model in the simplest form:

$$f_P = \rho + Cdt + M_{zpd} + \varepsilon_P - \ell_p = 0 \tag{2.2.4}$$

$$f_\Phi = \rho + Cdt + M_{zpd} + N\lambda + \varepsilon_\Phi - \ell_\Phi = 0 \tag{2.2.5}$$

Linearization of observation equations (2.2.4) and (2.2.5) around the a-priori parameters and observations (X^0, ℓ) becomes, in matrix form:

$$A\delta + W - V = 0 \tag{2.2.6}$$

$$X = [x, y, z, dt, zpd, N]^T \tag{2.2.7}$$

where A is the design matrix, δ is the vector of corrections to the unknown parameters X, $W = f(X^0, \ell)$ is the misclosure vector and V is the vector of residuals. X is the observation vector, consisting of four types of parameters: station position (x, y, z), clock (dt), troposphere zenith path delay (zpd) and (non-integer) carrier-phase ambiguities (N).

The least squares solution with a-priori weighted constraints (P_x) to the parameters is given by:

$$\delta = -\left(P_{X^0} + A^T P_\ell A\right)^{-1} A^T P_\ell W \tag{2.2.8}$$

so that the estimated parameters are:

$$\hat{X} = X^0 + \delta \tag{2.2.9}$$

with covariance matrix:

$$C_{\hat{X}} = P_{\hat{X}}^{-1} = \left(P_{X^0} + A^T P_\ell A\right)^{-1} \tag{2.2.10}$$

- Precise Point Positioning error Corrections

The non-differential observation is used in the PPP, and all the corrections in the GPS positioning need to be concerned for the pseudo-range or carrier-phase observations. The errors are corrected by two different ways, one is correction model, for the errors which could be modeled accurately, like phase center corrections, tides, relativity effects. The other is parameter estimation, for the errors which could not be modeled accurately, like the tropospheric effects and receiver clocks.

Some effects are quite large, exceeding several meters, like special and general relativity, Sagnac delay, satellite clock offsets, atmospheric delays, etc.. They must be considered even for pseudo-range positioning at the meter precision level. When attempting to achieve a few centimeters with ionospheric-free carrier phase observations, it is important to account for some effects, like Satellite Attitude Effects (satellite antenna offsets and phase wind-up), Site Displacements Effects (ocean loading, solid earth tides and earth rotation parameters) and Compatibility Considerations, which may not have been considered in pseudo-range or precise differential phase processing modes.

a. Satellite Antenna offsets

GPS satellite center of mass is used for the orbit, while the phase center of its antenna used for the satellite coordinates and clock products. The separation between the GPS satellite center of mass and the phase center of its antenna make the satellite based corrections. When measurements depending on the

antenna phase center, the satellite antenna offset are (0.279, 0.000, 1.023) m for the Block II/IIA, and need no corrections for Block IIR (Kouba, 2001).

The correction for a satellite coordinate can be expressed as (Xu, 2003):

$$\Delta \mathrm{r}_{sat} = x_{sat}\mathrm{e}_x + y_{sat}\mathrm{e}_y + z_{sat}\mathrm{e}_z \tag{2.2.11}$$

where, $\mathrm{e}_z = -\mathrm{r}_{sat}/|\mathrm{r}_{sat}|$, $\mathrm{e}_y = (\mathrm{e}_z \times \mathrm{e}_{sun})/|\mathrm{e}_z \times \mathrm{e}_{sun}|$, r_{sat} and r_{sun} are the geocentric coordinate of the satellite and sun, $\mathrm{e}_x = \mathrm{e}_y \times \mathrm{e}_z$, $\mathrm{e}_{sun} = (\mathrm{r}_{sun} - \mathrm{r}_{sat})/|\mathrm{r}_{sun} - \mathrm{r}_{sat}|$

b. Phase Wind-Up Correction

GPS satellites transmit right circularly polarized (RCP) radio waves, and the observed carrier-phase has the same orientation, which change it up to one cycle (one wavelength). This effect is so called phase wind-up, and it can reach up to 4 cm for a baseline of 4000 km (Wu et al., 1993). The phase wind-up correction is always neglected for double difference positioning when baselines up to a few hundred kilometers, however, it is important for un-differenced point positioning since it can reach up to one half of the wavelength.

The phase wind-up correction can be written as follows (Wu at al., 1993):

$$\Delta\phi = sign(\zeta)\cos^{-1}(\vec{D}' \cdot \vec{D} / |\vec{D}'||\vec{D}|) \tag{2.2.12}$$

where $\zeta = \hat{k} \cdot (\vec{D}' \times \vec{D})$, $\hat{k}$ is the satellite to receiver unit vector, $\vec{D}' = \hat{x}' - \hat{k}(\hat{k} \cdot \hat{x}') - \hat{k} \times \hat{y}'$, $\vec{D} = \hat{x} - \hat{k}(\hat{k} \cdot \hat{x}) - \hat{k} \times \hat{y}$ are the effective dipole vectors of the satellite and receiver computed from the current satellite body

coordinate unit vectors $(\hat{x}', \hat{y}', \hat{z}')$ and the local receiver unit vectors $(\hat{x}, \hat{y}, \hat{z})$.

Continuity between consecutive phase observation segments must be ensured by adding full cycle terms of $\pm 2\pi$ to the correction.

c. Solid Earth Tides

Earth tide is the sub-meter motion of the Earth of about semi-diurnal, diurnal and long term caused by moon and sun, while semi-diurnal amplitude of terrestrial tides can reach about 55 cm at the equator. The periodic vertical and horizontal site displacements are affected weakly by station latitude and tidal frequency and need to be taken into account when an accuracy of 1 mm is desired in determining station positions. Moreover, for differential positioning over short baseline (<100km), both stations have almost identical tidal displacements so that the relative positions over short baselines will be largely unaffected by the solid Earth tides

The correction of coordinates could be written as (McCarthy, 1996):

$$\Delta\vec{r} = \sum_{j=2}^{3} \frac{GM_j}{GM} \frac{r^4}{R_j^3} \left\{ \left[3l_2 \left(\hat{R}_j \cdot \hat{r} \right) \right] \hat{R}_j + \left[3\left(\frac{h_2}{2} - l_2 \right) \left(\hat{R}_j \cdot \hat{r} \right) - \frac{h_2}{2} \right] \hat{r} \right\} + \left[-0.025m \cdot \sin\phi . \cos\phi . \sin\left(\theta_g + \lambda \right) \right] \cdot \hat{r} \tag{2.2.13}$$

Where GM, GM_j are the gravitational parameters of the Earth, the Moon ($j = 2$) and the Sun ($j = 3$); r and $\hat{R}_j$ are geocentric state vectors of the station, the Moon and the Sun with the corresponding unit vectors r and $\hat{R}_j$, respectively; l_2 and h_2 are the nominal second degree Love and Shida dimensionless numbers (0.609, 0.085); φ, λ are the site latitude and longitude

(positive east) and θ_g is Greenwich Mean Sidereal Time.

d. Ocean Loading correction

Ocean loading results from the load of the ocean tides, and does not have a permanent part. Because of its diurnal and semi diurnal periods, the ocean loading could be neglected when the station is far away from the oceans, and static positioning with mm precision over 24h, or single epoch positioning with 5 cm precision. It should be taken into account, however, when the tropospheric ZTD or clock errors be estimated, unless the station is far way than 1000km from the oceans (Dragert, 2000).

The ocean loading correction model can be described as (McCarthy, 1996):

$$\Delta c_i = \sum_{j=1}^{n} f_j A_{ij} \cos\left(\omega_j t + \chi_j + u_j - \Phi_{ij}\right) \qquad (2.2.14)$$

where, Δc_i ($i = 1,2,3$) represent the displacement in the radial, west, and south components respectively; j ($j = 1,2,...,11$) represent 11 various waves groups of ocean loading effect; A and Φ are the amplitude and phase; ω and χ are the angular velocity and astronomical arguments at time $t = 0^h$; f and u depend on the longitude of the lunar node.

Other site displacement effects, such like the Earth Rotation Parameters, they could be neglected when positioning direct in the ITRF frame with orbit fixed or constrained strictly, and required when in an inertial frame, the more details could be found in Kouba (2001).

- What effect PPP performance

The baselines are estimated by the differenced positioning, which is so-called relative positioning, while PPP is the absolute positioning. Many errors could be eliminated by dual-frequency differenced observations in the differenced poisoning, like receiver clocks. All the observation errors should be taken into account in the PPP with zero-difference observations, however, using the correction models or estimated as the parameters.

The IGS products are used for the PPP, while satellite orbit, clock errors and EOPs assumed to be known. All these parameters could be estimated in the differenced poisoning with a long-range baseline (about several kilometers). A network or at least two stations need to be used in the differenced poisoning, while PPP technique processing data from a single station to obtain positions. So the measurement using PPP is independent and not affected by with other stations. The ambiguity parameters are integers in double-differenced GPS processing, while not integers in PPP with un-differenced observations, as they are corrupted by the initial fractional phase bias in the satellites and receivers.

The error correction models and ambiguity resolutions will be discussed, when we describe the performance of PPP. Both of them are related with the poisoning precision and the convergence period of the PPP. PPP is the processing of pseudo-range and carrier phase measurements from a single GPS receiver, using satellite precise orbits and clock offsets, which usually from IGS products. In the PPP performance, linear combination of dual-frequency code and phase could be used to remove the effect of ionospheric refraction. The tropospheric refraction and ambiguity parameters from the measurements are estimated together with the position.

To achieve a precise position from PPP, the other effects, such as Satellite

Attitude Effects (satellite antenna offsets and phase wind-up), Site Displacements Effects (ocean loading, solid earth tides and earth rotation parameters) must be taken into account and corrected with accuracy models. More discussion about the effects of errors could be found in Kouba (2001) and Chen (2009). Residual terms, however, are generally ignored, such as receiver noise and multi-path effect.

PPP convergence as a function of time depends on initial parameter variances and the synergy of GPS pseudo-range and carrier phase observations. The convergence period could be affected by a number of factors, such as the number and geometry of visible satellites, user environment and dynamics, observation quality and sampling rate. Therefore, the convergence time varies from the same processing in the different days and different user locations (Heroux et al., 2004). However, the tropospheric effects and the ambiguities are the main problems in the data process in PPP, which determining the convergence period.

At the initial epoch, because of unknown carrier-phase ambiguities, the solution relies entirely on the pseudo-range observations and the quality of the position reflects GPS receiver code resolution and the multi-path environment at the tracking station. As time passes and phase observations are added to the solution, the ionospheric free ambiguities and station position components (in static mode) converge to constant values while the tropospheric ZTD and receiver clock parameters vary as a function of their assigned process noise.

For tropospheric effect, initial station coordinates differ from the known values by as much as 50 cm. The convergence period, from a cold start to a decimeter-level positional solution, is typically about 30 min under normal conditions and will be significantly longer to the few centimeter-level (Gao and Shen, 2001; Heroux et al., 2004). With high-rate satellite clocks at 30-second

interval, this convergence time can be further reduced to less than 30 minutes (Kouba et al., 2001).

2.2.2 Real-Time Kinematics (RTK)

The concept of GPS kinematic positioning was introduced in the middle 1980s and GPS Real Time Kinematic positioning (RTK) equipment was available in early 1990s. RTK is a real time differential technique providing positions with cm accuracy in real time, which is widely used in surveying and high precision navigation (Rizos, 2007; Zou et al., 2013; Li et al., 2015). Based on double differencing, the common errors between the reference and the roving receiver could be negligible, like orbit and atmospheric errors. But the residual errors will increase when the distance increases, which will degrade the positioning precision. So the technique is limited in shorter distances (10 km or less) between the reference and the rover receiver (Rizos, 2006).

Network RTK is developed to solve the problem of long distance positioning, it is a method to use a group of spatially distributed GPS reference stations to model the spatially partly correlated errors in the covered region to increase the distances of users to the references stations (normally less than 100 km). Observations from multiple reference stations are gathered and processed in a common adjustment process where corrections for code and phase observations logged at the reference stations and in the rover are determined.

The purpose of the corrections is to reduce the influence of the spatially correlated errors. This means that when the corrections are applied to the rover code and phase observations, the position is determined using the position error and the atmospheric errors will be smaller, which results in an improved positioning performance (Wübbena et al. 2001). Various methods have been developed to establish these regional GPS errors models. On the other hand, due

to the improvements on GPS error modeling, the Precise Point Positioning (PPP) techniques have been rapidly developed over last 10 years. Compared with RTK technology, PPP technology does not require a nearby reference station and therefore it can be used to provide precise positioning accuracy anywhere in the world. However, due to ambiguity and tropospheric delay estimation in the PPP observation model, to achieve RTK positioning with PPP is still a difficult task.

- RTK error corrections

When using dual frequency GPS receivers in connection with network RTK, the ionospheric error can be handled by introducing the ionosphere free linear combination of the phase observations into the processing. Hereby the first order ionospheric effects are removed. The higher order effects of the ionosphere will still be present. For baselines of a 50 – 100 km their influence is relatively small, but for longer baselines the higher order effects should be considered (Rizos, 2006)

The orbit error can be reduced by using orbit parameters with a better quality than the broadcast orbits. The best orbit product presently available is the Ultra Rapid Precise Orbits from the IGS. These orbits have been available since March 2000. The orbits are determined twice a day (03 and 15 UTC) based on data collected up to 3 hours before the processing is done. The orbit files cover 48 hours where the first 24 hours are based on actual GPS observations and the next 24 hours are the predicted (extrapolated) orbits (Beutler et al., 2007). Daily estimates of the accuracy can be found on the web site of the University of Bern. The largest remaining error in the positioning process is now the tropospheric delay. Good modeling of the tropospheric delay is important in order to reduce the residual part of the tropospheric delay, which is the part of the delay that the RTK corrections must be accounting for.

2.2.3 Kinematics PPP

The Kinematics PPP is the processing of moving receivers, which may be similar with the RTK, while the RTK using differential observations with two receivers and the PPP just using only receiver. The same problems in the Kinematics PPP are tropospheric corrected model and ambiguity resolution.

- Ambiguity resolution

Many reasons lead to the lower precision, such like the impossibility to resolve phase ambiguities and the neglect of correlations between stations and clock corrections (Ge et al., 2008). The poisoning precision can be improved significantly by resolving the integer carrier-phase ambiguities. Such fixing is even more important for kinematic applications or static positioning with short-time observations, where results are improved dramatically. In expecting a similar improvement for PPP, which can not be removed the fractional-cycle biases (FCBs) from differenced observations, its ambiguity fixing is considered as one of the innovative issues for GNSS research and applications in the next ten years (Rizos, 2006).

It is found that the FCBs are stable in time and space, and could be estimates from a network. The integer carrier-phase ambiguity resolutions in could be achieved by applying improved satellite products to the separated FCBs from the integer ambiguities. Many studies have done recently, such as Ge et al. (2008), Collins (2008), Laurichesse et al. (2009), and Geng et al. (2009).

The single difference between satellites is usually used to remove the receiver-dependent FCBs. Then, the undifferenced ambiguities are divided into wide-lane and narrow-lane. Wide-lane FCBs are very stable over several days, or even a few months (Ge, 2008). In the research of Ge (2008), wide-lane FCBs

are determined by averaging the fractional parts of all pertinent wide-lane ambiguity estimates, from a global network of reference stations, using the Melbourne–Wübbena combination measurements (Melbourne 1985; Wübbena 1985). Narrow- lane FCBs are got in the similar way, but 15- min mean values are used to achieve high-precision solutions, due to the temporal instability of narrow-lane FCBs. Finally, these wide-lane and narrow-lane FCBs are used to correct non-integer ambiguities and fix the integer solutions. On average, more than 80% of the independent ambiguities could be fixed reliably, which leads to an improvement of about 27% in the repeatability and 30% in the agreement with the IGS weekly solutions for the east component of station coordinates, compared with the real-valued solutions (Ge, 2008).

The wide-lane FCBs are determination in the same way by Laurichesse et al. (2009) and Collins et al. (2008). The narrow- lane FCBs are not determined, however, and assimilated into the clock estimates. To achieve this by a network of reference stations, narrow-lane ambiguities had to be identified as integers and fixed to these integers before estimating the clocks. In practice, the horizontal accuracy of hourly position estimates at a static receiver was better than 2 cm.

The above two different methods are compared in both theory and practice by Geng (2010). Theoretical equivalence is proved between the ambiguity-fixed position estimates derived from these two methods. Then, 350 referenced stations from a global network in 2008 are used to illustrate how their daily position estimates agreed in practice. It is found that mean RMSE statistics of ambiguity-fixed position estimates against the IGS weekly solutions are 2 mm and 1.9 mm in east component, respectively using above two methods. Furthermore, the former way from Ge et al. (2008) is a little better for dense networks, whereas the later method a little better for sparse networks. And the former method is compatible with current official clock-generation methods,

which could conveniently supplement current network solutions as an additional software module, while the later method is incompatible with current clock products.

Another experiment about the former method is tested for the real-time PPP (Geng, 2010c). It is found that at least 10 min of observations are required for most receiver types to reliably fix about 90% of wide-lane ambiguities corresponding to high elevations, and over 20 min to fix about 90% of those corresponding to low elevations. Moreover, several tens of minutes are usually required for a regional network before a narrow-lane ambiguities estimate stabilizes to an accuracy of far better than 0.1 cycles. Finally, for hourly data, ambiguity resolution can significantly improve the accuracy of epoch-wise position estimates from 13.7, 7.1 and 11.4 cm to 0.8, 0.9 and 2.5 cm for the East, North and Up components, respectively, but a few tens of minutes is required to achieve the first ambiguity-fixed solution. However, this model can still be potentially applied to some near-real-time remote sensing applications, such as the GPS meteorology.

- Tropospheric correction

PPP is a very fast and efficient means to generate good station coordinates, but it is not possible to reach a coordinate quality as obtained from a network analysis. And because of the tropospheric effect, there are more than 30 minutes to get the coordinate with centimeter. So there are two points concerned by most research, the accuracy of the positioning, and the real-time of the data process.

For the real-time process, the tropospheric effect may be the most important problem. The correction model for the troposphere is not good enough, and the tropospheric effect could not be eliminated by the combination observations. So it's usually estimated as a parameter in the PPP data process, but requires certain

period of observation time to achieve reliable. The atmospheric models and mapping functions are conventionally used (Hopfield, 1969; Saasmamoinen, 1973; Niell, 1996), but a new approach has developed in recent studies, which is to reduce the effect of the tropospheric delay by pre-eliminate the tropospheric STD before the GPS data process with NWP, and it make the real-time process possibly (Eresmaa et al., 2006; Nordman et al., 2007). The more details please see the second part of the review.

Another problem with GPS PPP may be the lack of the observations, because of the single station, like in the mountain area for the deformation. Some research studies are contributed to the combined observations of GPS and GLONASS (Wang, 2000; Bruyninx, 2007). There still many problems, the two navigation systems are similar, but the coordinate systems, time systems and the signal frequencies are different. And in order to deal with the both GPS data and GLONASS data, the new model is necessary for the PPP.

Chapter 3 Tropospheric Refraction and its Correction

Tropospheric refraction is one of the classical research topics in Astronomy and Geodesy. When the radio signal goes though the troposphere, it will be refracted. The presence of medium produces the delay of radio signal, and the inhomogeneity of medium yields bending of signal propagation path, that forms two different research aspects of refraction: astronomical refraction and tropospheric delay. The latter is the main field in the thesis, specifically for the satellite geodesy.

The satellite geodesy has been greatly developed since 1960s, Achievements both in science and technology, particularly in computer and artificial satellite, bring surveying technique new challenges and requirements. New generation of the space surveying, represented by artificial satellites and deep spacecrafts, appears. A most important feature of the modern space surveying is to change the traditional observation mode from the natural objects to the artificial spacecrafts which move in limited distances and possess much higher accuracy motions in the 3-dimension space (Yan, 1999).

For high accuracy, the refraction correction becomes one of the main errors in space technique data process, including the GNSS positioning. In order to eliminate the troposphere effect in the space technique data process, many models are developed. In this Chapter, we will introduce the classical tropospheric corrections in space technique, and the different atmospheric models and observations used for tropospheric correction.

3.1 Tropospheric Characteristic

For the measurement of tropospheric refraction, characteristics of the

troposphere will be introduced. According to electromagnetic characteristics, Earth's atmosphere is divided into the neutral atmosphere, ionosphere and magnetosphere. The neutral atmosphere extends from the ground to 60 km, and the ionosphere extends from 60 km to 1000 km. According to temperature characteristics, the atmosphere is divided into the troposphere, stratosphere, middle layer, thermal layer and escape layer. The troposphere is the lowest layer of Earth's atmosphere. It contains approximately 80% of the atmosphere's mass and 99% of its water vapor and aerosols (Janes et al., 1989); it is the main part of the neutral atmosphere, thus the troposphere is also taken account in the neural atmosphere.

The troposphere itself can be divided into three parts. The bottom of the troposphere is from the ground up to 2 km; this portion is full of water vapor and aerosols. Because it extends to the ground, temperature in the troposphere has diurnal variation characteristics. The middle of the troposphere extends from 2 km to 6 km; it is affected less by the ground, and clouds and precipitation exist in this layer. The upper troposphere is from an altitude of 6 km to the tropopause. The temperature is always under 0 ℃, and water vapor is very sacred in this layer. The tropopause is the layer between the troposphere and stratosphere, and temperature is stable in this region. The height of tropopause is approximately 12-13 km in mid-latitudes, approximately 18 km in equatorial regions, and approximately 8 km in polar regions. Vertical movement of the atmosphere occurs in the troposphere, and all weather phenomena occur only in the layer, such as rain, snow and fog.

The tropospheric delay is influenced by three atmospheric factors: pressure, temperature, and relative humidity. Pressure is caused by the weight of the air of the atmosphere, and it drops exponentially with a rise in altitude. At sea level, the pressure is on average 1013 hPa, which is commonly used as the standard atmospheric pressure. Temperature also drops with a rise in altitude above sea

level at an average rate of -6.5 degrees Celsius per km. However, up until the tropopause, the temperature remains steady, then begins to rise in the following atmospheric layers. The percentage of humidity is determined by the relative portion of water vapor in the atmosphere. Humidity decreases drastically above 3 km because water vapor mostly exists in the bottom of the troposphere. Approximately 50% of water vapor is concentrated under 1.5 km, and less than 5-6% of water vapor is above 5 km (Schuler, 2001).

3.2 Tropospheric Refractivity

In order to well modeled tropospheric correction, many basic definitions and equations are given to describe the tropospheric refraction, such as **Fermat Law, Snell Law and Smith-Weintraub Equation** et al. (Hotine 1969; Smith and Weintraub 1953).

The definition of refractive index and refractivity of troposphere is given first. The physical mechanism of refraction can be simply explained as that the velocity of electromagnetic wave is not equal to that in vacuum (the general relativity is not considered except there is a special demand). The refractive index n (or the index of refraction) is defined as the ratio of velocities of electromagnetic wave in vacuum c and in medium v (Green 1985)

$$n = \frac{c}{v} \tag{3.2.1}$$

which equals to a unit in vacuum. A radio wave with wavelength λ, frequency f propagates in space; its phase velocity v is defined as

$$v = f\lambda \tag{3.2.2}$$

In dispersive medium the phase velocity v (or the refractive index n) is related to the wave frequency f (or wavelength λ). For a group of waves with little different frequencies, that means the space is dispersive, the propagation velocity of energy is defined as the group velocity v_g

$$v_g = -\frac{\mathrm{d}f}{\mathrm{d}\lambda}\lambda^2 \tag{3.2.3}$$

or

$$v_g = \left[\frac{\mathrm{d}f(k)}{\mathrm{d}k}\right]_{k_0} \tag{3.2.4}$$

In which $k = 1/\lambda$ is defined as the wave number. The tropospheric group refractive index n_g is defined as

$$n_g = \frac{c}{v_g} \tag{3.2.5}$$

For the convenience of the theoretical analysis and computation, the tropospheric refractivity N is introduced

$$N = (n-1)\times 10^6 \tag{3.2.6}$$

3.2.1 Fermat Law

As a microscope feature of the tropospheric refraction, radio waves propagate in medium according to Fermat Law (Hotine 1969): the optical distance σ is the

shortest between two arbitrary space points A and B, and the propagating time t

$$t = \frac{1}{c}\int_A^B n\mathrm{d}l \tag{3.2.7}$$

is a minimum, in which $\mathrm{d}l$ is the line element on the signal path. Fermat law gives a direct result of distance measurement by electromagnetic wave between two arbitrary field points.

3.2.2 Snell Law

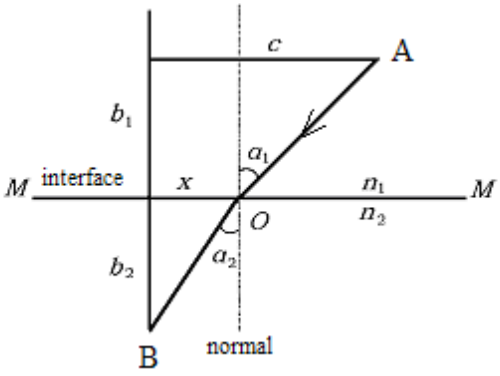

Figure 2.1: Diagram of Snell's Law

We apply Format law to a plane medium boundary MM, of which the refractive indexes on both sides are shown as n_1 and n_2, respectively, as shown in Figure 2.1. Fields A and B are in both side of the boundary MM, respectively. Signal propagates from A to B, the refractive point is assumed as O. Assuming:

$$BD = c, \quad EO = x, \quad DE = \mathrm{b}_1, \quad AE = b_2$$

AD is perpendicular to MM and BD, the optical distance σ between A and B is then written as

$$\sigma = n_2\sqrt{b_2{}^2 + x^2} + n_1\sqrt{b_1{}^2 + (c-x)^2} \tag{3.2.8}$$

Taking derivative of above expression to *x* and its minimum

$$\frac{\mathrm{d}\sigma}{\mathrm{d}x} = \frac{x}{\sqrt{b_2{}^2 + x^2}} n_2 + \frac{x-c}{\sqrt{b_2{}^2 + (x-c)^2}} n_1 = 0 \tag{3.2.9}$$

We have: $\dfrac{x}{\sqrt{b_2{}^2 + x^2}} n_2 = \dfrac{c-x}{\sqrt{b_2{}^2 + (x-c)^2}} n_1$

Using the angular relation we have the refraction law

$$n_1 \sin\alpha_1 = n_2 \sin\alpha_2 \tag{3.2.10}$$

in which α_1 and α_2 are the angles of the incidence and the emergence, respectively, n_1 and n_2 the index of refraction in medium 1 and 2, respectively, which are defined as the angles between the incidence or the emergence direction and the normal of the boundary. Eq. (3.2.10) is also called the Snell Formula or Snell Law.

3.2.3 Bouguer Formula

Under normal condition the Earth's atmosphere can be approximately considered as an ellipsoid in global. In local atmosphere the spherical symmetry can be adopted. Under the spherical symmetry, Bouguer Formula holds at the refractive boundary:

$$n_1 r_1 \sin\alpha_1 = n_2 r_2 \sin\alpha_2 \tag{3.2.11}$$

where r_1 and r_2 are the geocentric distances, respectively. For an arbitrary point along the ray Bouguer formula is written as:

$$nr\sin\alpha = \text{const} \equiv a \tag{3.2.12}$$

Where the a is called the refraction radius or the impact distance (Born and Wolf, 1980).

3.2.4 Smith-Weintraub Equation

Writing the refractivity as:

$$N = k_1 R_d \rho + k'_2 R_w + k_3 R_w \frac{\rho_w}{T} \tag{3.2.13}$$

where ρ and ρ_w are the densities of atmosphere and the water vapor (in kg/m^3), respectively; k_i are experimental constants (Thayer, 1974), $k'_2 = k_2 - (R_d / R_w)k_1$, R_d and R_w are the specific gas constants for dry air and water vapor, respectively; and T is atmospheric temperature (in K).

Take the atmosphere as the ideal gas, the equation (3.2.13) can be rewritten as:

$$N = 77.6\frac{P_d}{T} + 64.8\frac{P_{\mathrm{W}}}{T} + 3.776\times10^5\frac{P_{\mathrm{W}}}{T^2} \tag{3.2.14}$$

where P_d and P_{W} is the dry and the wet pressure respectively (in hPa). When $T = 280\mathrm{K}$, the last part of the equation (3.2.14) can be combined to

$$N = \frac{77.6}{T}(P + 4810\frac{P_W}{T}) = \frac{77.6}{T}P + 3.73\times10^5\frac{P_W}{T^2} \quad (3.2.15)$$

which is commonly called as Smith-Weintraub Equation**,** where P is the total pressure of the atmosphere (in hPa), and the first part on the right of equation is called the dry part of atmosphere, and the second part on the right equation is called the wet part of atmosphere. The error of equation (3.2.3) is less than 1%, when the frequency of the signal is lower than 100GHz (Smith and Weintraub 1953).

Moreover, in Eq. (3.2.3) the effect of particles are not taken into account, such as aerosols, sand, dust and volcanic ash etc.. And they produce a refractivity component on the order of 1-10 ppm (Solheim et el., 1999). Precipitating media, such as rain, snow and hail, produce essentially signal scattering which is responsible for a change in signal phase, In. terms of millimeter of path delay per km of propagation path, heavy rain, snow and hail, might produce delays up to 15, 7 and 0.75 mm/km, respectively (Solheim et al., 1999).

3.3 Atmospheric Model and Profile

Based on the equations for tropospheric refraction given in the Section 3.2, we find that the measurement of tropospheric refraction is highly related to the atmospheric parameters, like Pressure, Temperature and Humidity etc.. The modeling of the neutral atmosphere is the first goal of the refraction research.

In modern refraction research, the applied Earth atmosphere modeling can be assorted into two types. The first type is the atmospheric model, such as **Exponential model and Hopfiled Quartic profile**, which is mainly based on theoretic analysis. The second is the real atmospheric profile, like **Radiosonde**

profile and Numerical Weather Prediction (NWP) models, which is coming from measured models including predictive atmospheric models.

3.3.1 Exponential model

The hydrostatics equation and ideal gas equation of atmosphere can be written as:

$$\frac{\mathrm{d}P}{\mathrm{d}h} = -\rho g \tag{3.3.1}$$

And

$$\rho = \frac{PM_0}{TR} \tag{3.3.2}$$

where P is the atmospheric pressure, h is the altitude, ρ is the atmospheric density, g is the gravity acceleration, $M_0 = 28.970\mathrm{kg}\cdot\mathrm{kmol}^{-1}$ is the average molecular mass of the Earth' atmosphere, $R = 8314.34\mathrm{J}\cdot\mathrm{kmol}^{-1}\cdot\mathrm{K}^{-1}$ is the universal gas constant, T is the absolute temperature.

Supposed that the atmosphere is isothermal and static, the solutions of Eq. (3.3.1) and (3.3.2) are written as:

$$\frac{P}{P_0} = \exp\left[-\frac{g}{R_A T_0}(h - h_0)\right] \tag{3.3.3}$$

$$\rho = \frac{P_0}{T_0 R_A}\exp\left[-\frac{g}{T_0 R_A}(h - h_0)\right] \tag{3.3.4}$$

where T_0 is the constant temperature, $R_A = R/M_0$ is the gas constant of atmosphere, P_0 and h_0 are the pressure and altitude at station, respectively.

With help of the Smith-Weintraub Equation, the atmospheric refractivity of the exponential model can be written as:

$$N(h) = N_0 \exp\left(-\frac{h-h_0}{H}\right) \tag{3.3.5}$$

Where N_0 is the refractivity at observed station, and $H = \frac{R_A T_0}{\mathrm{g}}$, which is called the atmospheric effective height or the atmospheric scale height.

3.3.2 Hopfield Quartic profile

Assumed that, the temperature declines about 6.5℃ per kilometer in the troposphere, so:

$$\beta \approx 6.5^{\circ}\mathrm{C/km} \tag{3.3.6}$$

$$T(h) = T_0 - \beta(h-h_0) \tag{3.3.7}$$

With the hydrostatics equation (3.3.1) and ideal gas equation (3.3.2), the solutions of Eq. (3.3.1) is written as:

$$P = P_0\left[\frac{T_0 - (h-h_0)\beta}{T_0}\right]^{\frac{\mathrm{g}}{\beta R_A}} \tag{3.3.8}$$

With the Smith-Weintraub Equation, and make $\mu = \frac{g}{\beta R_A} - 1 = 4$ for both wet and dry part of the refractivity, the atmospheric refractivity of Hopfield quartic model could be written as:

$$N(h) = 77.6\frac{P_0}{T_0}\left(\frac{h_T - h}{h_T - h_0}\right)^4 + 3.73\times10^5\frac{P_{w0}}{T_0^{\,2}}\left(\frac{h_W - h}{h_W - h_0}\right)^4 \tag{3.3.9}$$

where, $H_T = 40136 + 148.72(T_0 - 273.15)$ m and $H_w = 11000$ m are the top of the dry and wet troposphere respectively; P_0, T_0, e_0 are the ground pressure, temperature (K) and water vapor pressure of station; h is the altitude of the station (Hopfield 1969). Customary, Eq.(3.3.9) is called Hopfield quartic profile.

But the real profile of atmospheric temperature is greatly different with the assumption in the Hopfield quartic model. A rather accurate atmospheric assumption is mentioned by Saastamionen (1972a, 1972b, 1973), which is the simplified model of standard atmospheric model (Allen, 1973). It is assumed that:

$$\begin{cases} T(h) = T_0 - \beta\,(h - h_0), & h \le h_t \\ T = \text{Constent}, & h > h_t \end{cases} \tag{3.3.10}$$

where h_t is the height of the tropopause.

3.3.3 The measured atmospheric profiles of Radiosonde

Today Radiosonde is one of the main tools to get high accurate atmospheric profiles. The first Radiosonde station was established by US Weather Bureau in 1936 (Rocken e al. 1997). Up till now there are thousands of Radiosonde

stations around the world, which give two experiments at Greenwich Time 0^h and 12^h.

The data from Radiosonde are the main sources for weather forecasting, climate analysis and atmospheric research. In the atmospheric refraction research the Radiosonde data are not only used to establish the local or global atmospheric refractive mapping functions, but also used to compare the accuracies of the different mapping functions. Recently they can be used to the atmospheric integrals, and to accurately correct the atmospheric refraction at low elevations on the real time. Under ideal conditions the Radiosonde accuracy is about 0.2K for temperature, 5 percent for relative humidity (up -25℃), 2hPa for pressure (down 500hPa).

The coverage of Radiosonde data in spatial and temperate is rather insufficient. The reasons are that its costs are higher and the general needs of personnel boarded the ground observation point. Twice-daily observations in the time domain are relatively sparse. The distributions of Radiosonde stations on the earth have considerable limitations and in the vast ocean, desert, mountains and other areas are relatively lacking. In developed areas, their distributions are relatively dense. The difference between south- and north- hemispheres is big. In any case, the application of Radiosonde data constitutes an important aspect in refraction studies.

10 05 31 08	471					
58362	121.46	31.41	5			
	1011	9999	19	14	90	3
	1000	10	18	12	85	5
	936	9999	13	12	9999	9999
	925	76	16	-3	45	2

			… …			
	150	1406	-58	9999	295	39
	113	9999	-65	9999	9999	9999
	105	9999	-66	9999	9999	9999
100	1655	-66	9999	310	32	
58150	120.25	33.77	7	150		
	1013	9999	18	15	70	3
	1000	11	17	14	70	4
			… …			
			… …			

Table 3.1: A profile sample of Radiosonde stations in China in 8:00, 31 May 2010

Table 3.1 gives a profile sample from China Meteorological Administration (CMA). This is a standard data format of Radiosonde measurements used in Chinese meteorological department, and it gives the data from ground to 100 (hPa), and the height is about from ground to 16 km.

The first line is the head of file, which gives the observation epoch on Beijing time (2000+year, month, day, hour) and the number of total Radiosonde stations in this file. Then second line gives the station information, the station number, longitude, latitude, and height. In the following lines the items are listed from ground to 100 (hPa) as: pressure (hPa), height ($\times$10m), temperature (^{o}C), temperature of dew point (^{o}C), wind azimuth (measured from the north to the east with degrees), wind velocity (m/s). Then is the next Radiosonde station, and the number of 9999 in box means there is no data recorded.

3.3.4 Numerical Weather Prediction (NWP) model

The Numerical Weather Prediction (NWP) model predicts weather from current weather conditions under certain initial and boundary values. The NWP model

represents data assimilation and a prediction system for the atmosphere. According to its operational use in weather forecasting, it is a divided global and regional mesoscale model.

The global NWP model describes movement in the troposphere over a relatively long period of time. The two most popular models are the European Centre for Medium-Range Weather Forecasts (ECMWF) and the Global Forecasting System (GFS) (Bock et al., 2009; Wang et al, 2017). The new generation of global NWP models developed by the China Meteorological Administration (CMA) is called the Global/Region Assimilation and Prediction System (GRAPES). The spatial resolution of GRAPES is 0.25 ° x 0.25 ° with 60 layers, and the rain forecast is very close to the ECMWF model (Shen et al., 2017).

The regional mesoscale model describes mesoscale movement in the troposphere for severe weather. The Weather Research and Forecasting (WRF) model, developed by the National Center for Atmospheric Research (NCAR), is currently used in many forecasting centers. The STI-WARMS (Shanghai Typhoon Institute-WRF ADAS Real-Time Modeling System) model is a regional model developed by the Shanghai Meteorological Bureau (SMB). It is based on the WRF system and the ARPS Data Analysis System (ADAS) from the University of Oklahoma (Li et al., 2016; Chen et al. 2013). Compared to the global model, it has a much higher spatial and temporal resolution. The model covers the East China area with a 9-km resolution; the products of the model include atmospheric parameters such as pressure and temperature, as well as weather system-related parameters. The NWP data used in this thesis are predicted from the STI-WARMS.

3.4 Tropospheric correction model

Tropospheric correction models are developed to eliminate the troposphere

effect for radio signal. As an electromagnetic wave propagates in the atmosphere, it is continuously refracted due to the varying index of refraction of the air between the top of the atmosphere and ground. There basically two effects on a ray path: bending and retarding. Both effects produce an excess path length with respect to propagation in a vacuum (Janes, 1991). For such excess path length, also called **Tropospheric delay**, we describe it by tropospheric refractivity as follow:

The optical distance of satellite and receiver σ can be written as:

$$\sigma = \int_l n \mathrm{d}l = \int_{r_0}^{r_T} \frac{n}{\sin\theta} \mathrm{d}r \tag{3.4.1}$$

where the n is the refractive index along the radio signal path l, r_0 is geocentric distance of station, r_T is geocentric distance of tropopause.

The atmospheric delay is defined as the differences between the optical distance σ and the geometric distance S :

$$\Delta\sigma = \sigma - S = \int_l n \mathrm{d}l - \int_S \mathrm{d}S \tag{3.4.2}$$

Equation (3.4.2) also could be rewritten as:

$$\Delta\sigma = \sigma - S = \int_l (n-1)\mathrm{d}l + \left(\int_l \mathrm{d}l - \int_S \mathrm{d}S \right) = \int_l (n-1)\mathrm{d}l + \delta\sigma \tag{3.4.3}$$

Where $\delta\sigma$ is the geometrical excess path length, called bending correction, and it is usually neglected of the total path delay (Ichikawa et al., 1995).

With **Bouguer formula**:

$$nr\cos\theta = const = n_0 r_0 \cos\theta_0 \tag{3.4.4}$$

Where n_0, θ_0 are the index of refraction and elevation angle of station, Equation (3.4.2) is rewritten as:

$$\Delta\sigma = 10^{-6}\int_{r_0}^{r_T} \frac{nrN\mathrm{d}r}{\sqrt{n^2r^2 - (n_0 r_0 \cos\theta_0)^2}} \tag{3.4.5}$$

The equation (3.4.3) and (3.4.5) of tropospheric path delay are unresolved, and series extension for the numerical solutions may be the proper way. The most widely used is Saastamionen Equation, which is used as the prior value in GNSS data process. Then tropospheric delay is defined as the Zenith Delay mapping to elevation angle since 1970s. Chao's Equation, Marini's Equation, Davis's Equation and UNSW931 model are developed for mapping function (Chao, 1970; Marini,1972; Davis, 1985; Yan, 1995). Herring (1992) first used the Radiosonde profile for the mapping function, but the Niell Mapping Function (NMF) is the most widely used in GNSS data process (Niell,1996).The details of these models are introduced in this section.

3.4.1 Saastamionen Equation

A correction of tropospheric path delay is mentioned by Saastamionen (1972a, 1972b, 1973), which is transferring integration to:

$$\Delta L = 0.002277\sec Z_0\left[P_0 + \left(\frac{1255}{T_0} + 0.05\right)P_{\mathrm{W}0} - B\tan^2 Z_0\right]w(\varphi, h_0) + \delta_g$$

(3.4.6)

Z_0 is the viewed zenith distance of observation, B and δ_g are the correction parameters (Table 3.2 and Table 3.3), $w(\varphi, h_0)$ is the gravity acceleration's correction for earth rotation.

$$w(\varphi, h_0) = 1 + 0.0026\cos 2\varphi + 0.00028h_0 \tag{3.4.7}$$

Where φ and h_0 are the latitude and altitude (km) of station respectively.

Altitude of Station	B (hPa)	Altitude of Station	B (hPa)
0 km	1.156	2 km	0.874
0.5 km	1.079	2.5 km	0.813
1.0 km	1.006	3 km	0.757
1.5 km	0.938	4 km	0.654
2 km	0.874	5 km	0.563

Table 3.2: The standard values of B

Viewed Zenith Distance	Altitude of Station							
	0km	0.5km	1km	1.5km	2km	3km	4km	5km
60°00'	0.003	0.003	0.002	0.002	0.002	0.002	0.001	0.001
66°00'	0.006	0.006	0.005	0.005	0.004	0.003	0.003	0.002
70°00'	0.012	0.011	0.010	0.009	0.008	0.006	0.005	0.004
73°00'	0.020	0.018	0.017	0.015	0.013	0.011	0.009	0.007
75°00'	0.031	0.028	0.025	0.023	0.021	0.017	0.014	0.011
76°00'	0.039	0.035	0.032	0.029	0.026	0.021	0.017	0.014
77°00'	0.050	0.045	0.041	0.037	0.033	0.027	0.022	0.018

78°00’	0.065	0.059	0.054	0.049	0.044	0.036	0.030	0.024
78°30’	0.075	0.068	0.062	0.056	0.051	0.042	0.034	0.028
79°00’	0.087	0.079	0.072	0.065	0.059	0.049	0.040	0.033
79°30’	0.102	0.093	0.085	0.077	0.070	0.058	0.047	0.039
79°45’	0.111	0.101	0.092	0.083	0.076	0.063	0.052	0.043
80°00’	0.121	0.110	0.100	0.091	0.083	0.068	0.056	0.047

Table 3.3: The values of δ_g (in meter)

There are three problems in the Saastamionen equation. First, it’s the function of viewed zenith distance; Second, it just could be used when elevation angle is bigger than 10^o; Third, the precision of the path delay is not very good, especially for the low elevation angles (near 10^o). So the Saastamionen equation for path delay correction is only used when elevation angle is bigger than 15^o in the GNSS data process. But the gravity correction in the equation is another important contribution of Saastamionen, which is widely used in many path delay models.

3.4.2 Zenith Delay, Mapping Function and Related Equations

With the symmetric assumption, and when $\theta_0 = 90°$, the equation (3.4.2) is defined as zenith delay:

$$\Delta\sigma_Z = \Delta\sigma(\theta_0 = 90°) \tag{3.4.8}$$

In most atmospheric models, the zenith delay could be integrated, and it is a function with the ground atmospheric parameters of station and geophysical parameters. With the relativity between the zenith delay and ground atmospheric parameters (P_0, T_0, P_{W0}), the tropospheric delay could be written as:

$$\Delta\sigma = \Delta\sigma_z(P_0, T_0, P_{W0}) \cdot m(Z_0, \mathbf{p}) \tag{3.4.9}$$

Where m is defined as mapping function, which means the tropospheric delay is mapped from the zenith to any elevation angle Z_0; $\mathbf{p}$ is related with the atmospheric and geophysical parameters.

a. **Chao's Equation**

In the early1970s, the tropospheric delay is described by Chao (1970) as:

$$\Delta\sigma = \Delta\sigma_Z \frac{1}{\sin\varepsilon + \dfrac{0.0043}{\tan\varepsilon + 0.0455}} \tag{3.4.10}$$

Where ε is the true elevation angle. The fraction of right equation is 1, when in the zenith.

In addition, the tropospheric delay with unsymmetrical atmosphere is got from ray tracing by Chao (1971); He tried to get tropospheric delay from Radiosonde data (Chao 1972a); and the wet mapping function was constructed by Chao (1972b):

$$\Delta\sigma_W = \Delta\sigma_{WZ} \frac{1}{\sin\varepsilon + \dfrac{0.00035}{\tan\varepsilon + 0.017}} \tag{3.4.11}$$

The related model could also be found in the early GAMIT software, the equation (3.4.10) and (3.4.11) are called dry and wet mapping function of **Chao's Equation**.

b. **Marini's Equation**

It is first developed by Marini (1972), that the tropospheric delay is described with Zenith Delay and Mapping Function. In the **Marini's Equation**, the mapping function is defined as continued fraction with constant parameters:

$$m(Z_0) = \cfrac{1}{\cos Z_0 + \cfrac{a_1}{\cos Z_0 + \cfrac{a_2}{\cos Z_0 + \cfrac{a_3}{\cos Z_0 + a_4}}}} \tag{3.4.12}$$

Where $a_1 = 0.00085599$, $a_2 = 0.0021722$, $a_3 = 0.0060788$, $a_4 = 0.11571$, and Z_0 is the viewed zenith distance.

Compared to the series extension, this method is more simply and can be used for lower elevation angle. But in the Marini's equation, the mapping function just a global and yearly averaged model, and have no relationship with true atmosphere (Yan, 1996; 1999).

c. **Davis's Equation**

Using the simplified standard atmospheric model (mentioned in sec 3.3.2) for atmospheric parameters, the mapping function defined by Davis is written as (Davis et al., 1985):

$$m(\xi_0) = \cfrac{1}{\cos \xi_0 + \cfrac{a_1}{\cot \xi_0 + \cfrac{a_2}{\cos \xi_0 + a_3}}} \tag{3.4.13}$$

Where,

$$a_1 = 0.001185[1 + 0.6071\cdot 10^{-4}(P_0 - 1000) - 0.1471\cdot 10^{-3} P_{W0} + 0.3072\cdot 10^{-2}(T_0'-20) + 0.01965(-\beta + 6.5) - 0.5645\cdot 10^{-2}(h_T - 11.231)]$$

,

$$a_2 = 0.001144[1 + 0.1164\cdot 10^{-4}(P_0 - 1000) + 0.2795\cdot 10^{-3} P_{W0} + 0.3109\cdot 10^{-2}(T_0'-20) + 0.03038(-\beta + 6.5) - 0.01217(h_T - 11.231)]$$

,

$$a_3 = -0.0090 \tag{3.4.14}$$

The atmospheric parameters, P_0, P_{W0} are ground pressure and water pressure (in hPa), and T_0' is the ground temperature (in ^{o}C).

d. UNSW931 and UNSW932 models

Based on the generator function theory, Yan and Ping (1995) developed UNSW931 for standard atmospheric profile and UNSW932 for Hopfield atmosphere. The mapping function in these models is written as (Yan et al., 1996; 1998; 2000):

$$m(\xi_0) = \cfrac{1}{\cos\xi_0 + \cfrac{D_1}{I^2\sec\xi_0 + \cfrac{D_2}{\cos\xi_0 + \cfrac{D_3}{I^2\sec\xi_0 + D_4}}}} \tag{3.4.15}$$

in the normalized effective zenith argument I is defined as

$$I = \sqrt{\frac{r_0}{2H}}\cot\xi_0 \tag{3.4.16}$$

and r_0 is the earth radius, ξ_0 is the true zenith of object, H is the effective height of the Earth atmosphere.

The coefficients for the standard atmosphere D_1, D_2, D_3, D_4 (UNSW931 model) are written as

$$
\begin{aligned}
D_1 &= 0.4613893 + 2.864\cdot10^{-5}(P_0 - 1013.25) + 8.99\cdot10^{-6}P_{W0} - 6.98\cdot10^{-6}{P_{W0}}^2 - \\
&\quad -1.0914\cdot10^{-4}(T_0'-15) + 1.30\cdot10^{-6}(T_0'-15)^2 + 9.4694\cdot10^{-3}(\beta + 6.5) - \\
&\quad -2.4946\cdot10^{-3}(h_T - 11.231) + 1.8072\cdot10^{-4}(h_T - 11.231)^2 \\
D_2 &= 0.8276476 + 2.056\cdot10^{-5}(P_0 - 1013.25) + 2.3820\cdot10^{-4}P_{W0} - 4.76\cdot10^{-6}{P_{W0}}^2 + \\
&\quad +5.1125\cdot10^{-4}(T_0'-15) + 1.23\cdot10^{-6}(T_0'-15)^2 + 3.6479\cdot10^{-2}(\beta + 6.5) - \\
&\quad -1.5321\cdot10^{-2}(h_T - 11.231) + 9.4802\cdot10^{-4}(h_T - 11.231)^2
\end{aligned}
$$

$$
\begin{aligned}
D_3 &= 2.531492 + 1.093\cdot10^{-4}(P_0 - 1013.25) + 2.6179\cdot10^{-3}P_{W0} + 1.33\cdot10^{-5}{P_{W0}}^2 + \\
&\quad +3.7103\cdot10^{-3}(T_0'-15) + 4.95\cdot10^{-6}(T_0'-15)^2 + 1.6022\cdot10^{-1}(\beta + 6.5) - \\
&\quad -8.9980\cdot10^{-2}(h_T - 11.231) + 4.9496\cdot10^{-3}(h_T - 11.231)^2 \\
D_4 &= 47.07844 + 1.595\cdot10^{-3}(P_0 - 1013.25) + 3.9026\cdot10^{-2}P_{W0} + 2.41\cdot10^{-4}{P_{W0}}^2 - \\
&\quad -4.1713\cdot10^{-2}(T_0'-15) + 2.16\cdot10^{-4}(T_0'-15)^2 + 1.6313(\beta + 6.5) - \\
&\quad -9.9757\cdot10^{-1}(h_T - 11.231) + 4.4528\cdot10^{-2}(h_T - 11.231)^2
\end{aligned}
\qquad (3.4.17)
$$

in which P_0 (hPa), P_{w0} (hPa) are pressure and wet partial at station, respectively, $T_0^{'}$ (oC) is ground temperature, β is the temperature lapse rate (K/km), h_T(km) is the height of tropopause.

And the coefficients for the Hopfield atmosphere $D_1^H, D_2^H, D_3^H, D_4^H$ (UNSW932 model) are written as

$$D_1^{\mathrm{H}} = 0.4460124 + 3.737\cdot10^{-5}(P_0 - 1013.25) + 1.0502\cdot10^{-4}P_{W0} - 1.52\cdot10^{-6}P_{W0}^{\ 2} - \\ - 2.6282\cdot10^{-4}(T_0' - 15) + 1.69\cdot10^{-6}(T_0' - 15)^2 - 5.8125\cdot10^{-3}(\beta + 6.5) - \\ - 3.955\cdot10^{-5}(\beta + 6.5)^2$$

$$D_2^{\mathrm{H}} = 0.7309351 + 2.897\cdot10^{-5}(P_0 - 1013.25) + 2.2\cdot10^{-7}(P_0 - 1013.25)^2 + \\ + 3.2562\cdot10^{-4}P_{W0} + 4.32\cdot10^{-6}P_{W0}^{\ 2} - 1.3335\cdot10^{-4}(T_0' - 15) + 1.36\cdot10^{-6}(T_0' - 15)^2 - \\ - 8.8333\cdot10^{-4}(\beta + 6.5) + 1.9974\cdot10^{-4}(\beta + 6.5)^2$$

$$D_3^{\mathrm{H}} = 1.953497 + 1.449\cdot10^{-4}(P_0 - 1013.25) - 2.0\cdot10^{-6}(P_0 - 1013.25)^2 + \\ + 5.4075\cdot10^{-3}P_{W0} + 8.61\cdot10^{-7}P_{W0}^{\ 2} - 1.937\cdot10^{-4}(T_0' - 15) + 4.90\cdot10^{-6}(T_0' - 15)^2 + \\ + 1.8434\cdot10^{-2}(\beta + 6.5) + 2.4630\cdot10^{-3}(\beta + 6.5)^2$$

$$D_4^{\mathrm{H}} = 39.76031 + 2.186\cdot10^{-3}(P_0 - 1013.25) - 2.91\cdot10^{-5}(P_0 - 1013.25)^2 + \\ + 8.4589\cdot10^{-2}P_{W0} + 1.19\cdot10^{-5}P_{W0}^{\ 2} - 7.2530\cdot10^{-2}(T_0' - 15) + 2.86\cdot10^{-4}(T_0' - 15)^2 - \\ - 2.7715(\beta + 6.5) - 0.16272(\beta + 6.5)^2$$

(3.4.18)

and the zenith delay for UNWS932 is written as

$$\Delta\sigma_z^H = \frac{10^{-6}}{5}N_0(h_{\mathrm{T}} - h_0) \qquad (3.4.19)$$

Under the normal meteorological conditions, the internal accuracy of UNWS models are about 1 cm above 2.5 elevation.

3.4.3 Applications of Radiosonde and Some Related models

In order to eliminate the differences between the model atmosphere and the true atmosphere, Radiosonde data is often used for the dry and wet delays' estimation. The tropospheric delay $\Delta\sigma$ is described by the sum of the dry partial $\Delta\sigma_d$ and

wet partial $\Delta\sigma_W$:

$$\Delta\sigma = \Delta\sigma_d + \Delta\sigma_W = \Delta\sigma_{dZ} m_d + \Delta\sigma_{WZ} m_W \tag{3.4.20}$$

Where m_d, m_W are the dry and wet mapping functions, respectively.

a. **MTT model**

Ten Radiosonde stations are used for the forming mapping functions by Herring (1992), which is named **MTT model**:

$$m_d(\varepsilon) = \frac{1 + a_d /[1 + b_d /(1 + c_d)]}{\sin\varepsilon + \dfrac{a_d}{\sin\varepsilon + \dfrac{b_d}{\sin\varepsilon + c_d}}} \tag{3.4.21}$$

$$m_W(\varepsilon) = \frac{1 + a_W /[1 + b_W /(1 + c_W)]}{\sin\varepsilon + \dfrac{a_W}{\sin\varepsilon + \dfrac{b_W}{\sin\varepsilon + c_W}}} \tag{3.4.22}$$

Where,

$$\begin{aligned}
a_d &= [1.2320 + 0.0139\cos\varphi - 0.0209h_0 + 0.00215(T_0' - 10)]\cdot 10^{-3} \\
b_d &= [3.1612 - 0.1600\cos\varphi - 0.0331h_0 + 0.00206(T_0' - 10)]\cdot 10^{-3} \\
c_d &= [71.244 - 4.293\cos\varphi - 0.149h_0 + 0.0021(T_0' - 10)]\cdot 10^{-3} \\
a_W &= [0.583 - 0.011\cos\varphi - 0.052h_0 + 0.0014(T_0' - 10)]\cdot 10^{-3} \\
b_W &= [1.402 - 0.102\cos\varphi - 0.101h_0 + 0.0020(T_0' - 10)]\cdot 10^{-3} \\
c_W &= [45.85 - 1.91\cos\varphi - 1.29h_0 + 0.015(T_0' - 10)]\cdot 10^{-3}
\end{aligned}$$

here ε is the true elevation angle; φ is the latitude of station; h_0 is the altitude of station (in km).

b. **NMF model**

A recently widely used mapping function is **NMF model** (Niell, 1996), which using the 26 Radiosonde data to fixing the constant parameters a,b,c :

$$a(\varphi,d) = a_{avg}(\varphi) - a_{amp}(\varphi)\cos\left(2\pi\frac{d-D_0}{365.25}\right) \tag{3.4.23}$$

where, φ is the latitude, d is the Day of Year (DOY), D_0 = 28, and the parameters b,c are similar to Eq.(3.4.24). The efficients $a_{avg}, a_{amp}, b_{avg}, b_{amp}, c_{avg}, c_{amp}$ are given in the tables in Niell (1996).

It should be noticed that there are some mistakes in the station height corrections in NMF model (Yan et al., 2000), which are not discussed further in this thesis.

c. **Mapping function based on NWP**

The NWP and Radiosonde data can be used to construct a new generation of the mapping function by numerical integration at real time, which can reach a more accurate degree than any mapping function model. The NMF and Radiosonde data are prepared by terms of station coordinates, meteorological parameters, and the time. There are some restrains in Radiosonde station position and time coverage. The next generation mapping functions can be based alone on high revolution NWP models, such as isobaric mapping function (IMF) by using intermediate parameters of NWP (Niell, 2001), Vienna mapping function (VMF) (Boehm and Schuh, 2004) and the improved version VMF1(Boehm et al., 2006a) are based on the ray tracing through the atmosphere. The Global mapping function (GMF) was then developed, which combined the accuracy of VMF1

and the coverage of NMF (Boehm et al., 2006b).

3.5 Tropospheric measurement from GNSS

The propagation process analysis for signals transmitted from satellite constellations allows us to inverse information from the Earth's atmosphere alone into signal paths. This inversion process forms a new aspect of meteorology – GPS meteorology, which is divided into ground-based and space borne types according to their operational modes (Bevis et al., 1992; Rashid et al., 2006).

Ground-based GPS networks are used to estimate the Zenith Total Delay (ZTD). The ZTD can be estimated every half hour, and spatial resolution depends on the density of the networks (Bevis et al., 1994; Kuo et al., 1996; Yang et al., 2008). The troposphere is formed by a dry part and a wet part. The Zenith Wet Delay (ZWD) temporal variations can exceed 10-20% in a few hours and are less predictable compared to surface measurements (Braun et al., 2001; 2003; 2004). Traditionally, in GPS measurements, tropospheric delays are taken as unknown parameters and estimated together with coordinates. Precipitable Water Vapor (PWV) is deduced from the ZWD, and the precision of PWV is approximately 2-3 mm when compared with the Radiosonde (Ware et al., 1996; Wang et al., 1999; Kuo et al., 2000).

For space-based GPS receivers, bending angles are retrieved from observations, and the refractivity profile is transformed from the bending angles by the Abel integration (Fjelbdo, 1971). The water vapor profile can be deduced if the temperature profile is known, and vice versa (Kursinski et al, 1996a; Kursinski et al, 1997; Kursinski et al, 2000; Hajj et al, 2002; Sokolovskiy et al, 2001). The precision of temperature could be achieved at 2 K, but the inversion of water

vapor may be not sufficient in the lower troposphere (Anthes et al., 2000; Guo et al, 2005; Kuo et al., 2000; Liu et al, 2006). The horizontal spatial resolution of water vapor is low, but the vertical resolution is very high. In addition, occultation points are globally distributed well.

Chapter 4 A Fast and Accurate Iterated Ray Tracing (FAIRT) Algorithms for Tropospheric Delays

4.1 Introduction

When the GNSS signal emits through the atmosphere, it is delayed and bent. The delays and bends along the GNSS signal path are defined as the Slant Total Delays (STDs). Ray tracing has been a common approach for addressing radio signal propagation through the atmosphere for a long time. Ray tracing is based on the Least Travel Time (LTT) principle. Many mathematic algorithms for ray tracing are developed to achieve a fast or accurate STD, including the 2-D and 3-D method. In the sophisticated ray tracing method, the atmosphere is divided into many layers between the surface and the satellite receiver. The atmospheric refractivity of each layer will be calculated, then the refractivity integral along the signal path will result in the STD.

For 2-D method, the simplest method is the linear method (Hobiger, 2008), where the ray path is linear between the two layers of the atmosphere, and the refractivity is only related to height. Vertical profiles of atmospheric parameters from data provided by sources such as the Numerical Weather Prediction (NWP) model or Radiosonde are used for estimating refractivity in each layer. Then, Snell's law is used to calculate the bending angle between the two layers. The linear method is the fastest way to get the STD but is also the least accurate. Thayer (1967) developed a rapid and more accuracy method; it is a more advanced way to take into account bending during each layer of the atmosphere. However, this method is still based on the assumption of spherical symmetry in the atmosphere.

For the 3-D method, the most used approach is to neglect the bending of the

signal; with 3-D meteorological data from the NWP model, refractivity can be calculated by the Smith-Weintraub equation. The ray path is a straight line between the receiver and the satellite in 3-D space. It is also fast, but if the bending is neglected, it will lead to an approximate 1% error in STD, causing a larger error at lower elevation angles. The 3-D Eikonal equation (Paris and Hurd, 1969) can be used to take into account bending in the 3-D ray path. Based on the NWP model, refractivity on a 3-D grid will solve the Eikonal equation with numerical solutions. Eikonal is more accurate than other methods, but it will take a long time to get achieve the solutions (Hobiger, 2008).

Bending is usually neglected in the total path delay (Ichikawa et al., 1995). However, for a 5 ° elevation angle, the effects of bending can be more than 20 cm, while for elevation angles larger than 15 °, the effects of bending are usually below 1 cm (Ghoddousi-Fard, 2009a; 2009b). The bending correction will be accounted for in the ray tracing algorithm in this study. We propose to develop a new Fast and Accurate Iterated Ray Tracing (FAIRT) algorithm that supports real-time high precision positioning. In this method, refractivity is taken into account in 3-D space based on the NWP model. Bending is not neglected, but it is taken into account in the 2-D method under the assumption of local spherical symmetry. Specifically, an iteration procedure is used for search accuracy refractivity on each integrated point. For an accelerated iteration speed, the exponential model for refraction distribution is used as the prior value.

The new ray tracing algorithm is used to integrate tropospheric delays from stations in the East China region. Apart from the ray tracing algorithms themselves, the accuracy, resolution, and proximity of these atmospheric parameters are the most important factors for achieving accurate results. The meteorological (MET) data for the experiment is obtained from the high spatial and temporal resolution regional NWP model, which was developed by the Shanghai Meteorological Bureau (SMB). The Zenith Total Delay (ZTD) is

obtained when the ray tracing path is along the zenith direction. The precisions of the ZTD and STD are analyzed, and the applications of STD are also discussed.

4.2 Fast and Accurate Iterated Ray Tracing (FAIRT) Method

The atmosphere is divided to many layers from the surface to satellite receiver From **Smith-Weintraub Equation** (3.2.3), the refractivity of each layer could be written as:

$$N_i = \frac{77.6}{T_i} P_i + 3.73 \times 10^5 \frac{P_{W_i}}{T_i^2} \tag{4.2.1}$$

From 10hPa to the up, the magnitude of STD is about 1% of the total delay (Eresmaa et al., 2006). The top of Radiosonde or NWP model is 10hPa, so use the exponential model for the refractivity up to the 50hPa, equation (3.3.5).

Atmospheric delay could be rewritten as:

$$STD = \int_l N \mathrm{d}\sigma + \delta\alpha = \sum N \cdot \Delta\sigma + \delta\alpha \tag{4.2.2}$$

Where, $\Delta\sigma$ is the integrate element, $\delta\alpha$ is bending correction.

There are two ways to add the bending correction, one is after integrated from station to the satellite, calculate the bending angle; the other is that the slant distance and the angle are calculated together by applying Snell's law. The later way is used here, but because of the bending the view angle from the station (surface) is different with the elevation angle, especially in the low elevation angle. The interpolation may be used in the final results.

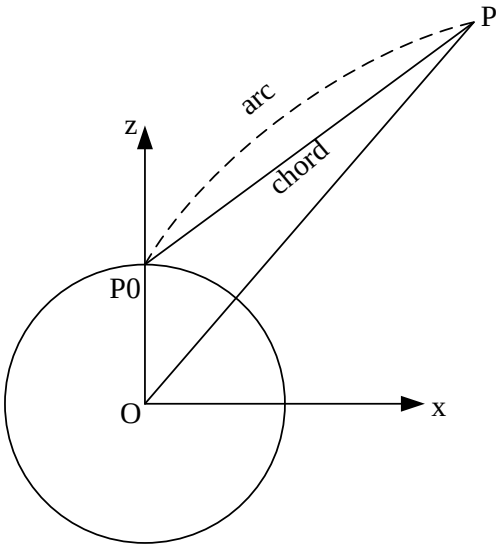

Figure 4.1: The Geometrical Path of GPS signal from surface to the satellite receiver

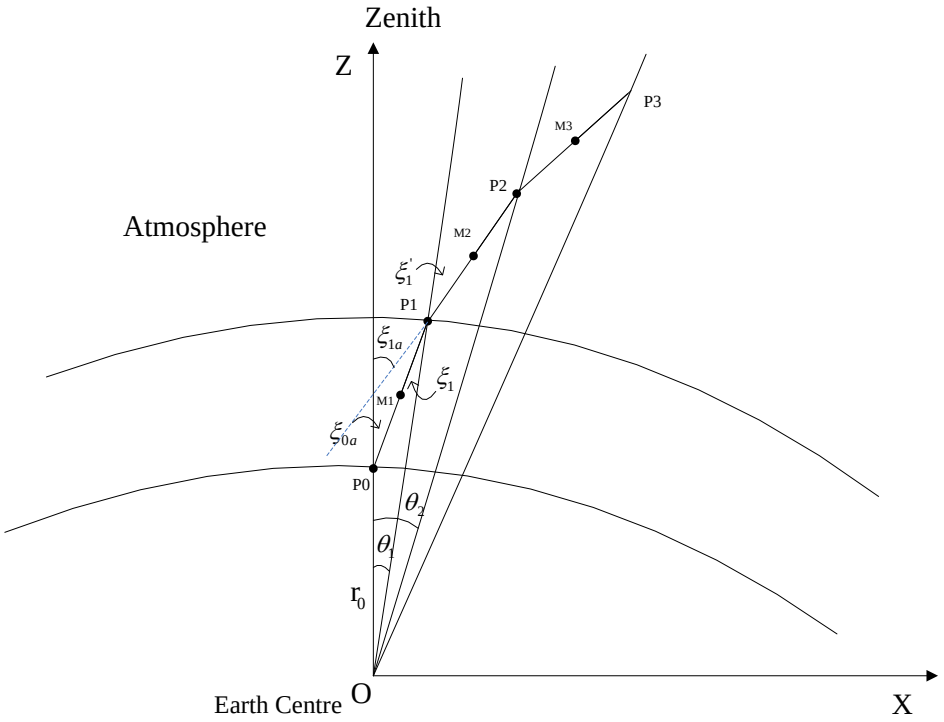

Figure 4.2: The Ray Tracing Path of GNSS signal from surface to the satellite receiver

Assuming $h_0 = 0$, is at the station p_0, α_0 is the arrival angle at p_0; $r_0 = 637800\text{m}$ is the Earth's radius, O is the Earth's Center, $\Delta\sigma = 100\text{m}$ is the Integrate element.

Exponential Distribution function for refractivity is $N(h) = N_0 e^{-\frac{h}{H}}$, when $T \cong const$, $g \cong const$ in the atmosphere, $H = \frac{g}{RT}$, $H = 7972.5m$, $N_0 = 300$ are set for the typical values.

When the positions of GNSS receiver and satellite are known, the elevation angel α_{0a} and azimuth angle φ of station can be calculated. The bending of the ray path is only taken account to the elevator angel. So all the Y-vector of coordinate is mapping from the X-vector by $\cos(\varphi)$, and the X-, Z- vectors of coordinate for integrate points at the ray path are obtained as the FATR method in the flow. The refractivity at each integrate point can be calculate by the MET data from NWP model, when the point coordinate is fixed. Last, the result of STD is get from the integration along the ray path.

First step of FATIR method, is the integration from point P_0 to get P_1.

1) At point P_0, taking a linear element $P_0P_1 = \Delta\sigma$, $\angle ZP_0P_1 = \alpha_{0a}$, $\theta_0 = 0$, the coordinate of P_0 is get, $X_{P_0} = 0$, $Z_{P_0} = r_0$, and. The integration result at point P_0 is $STD = 0$.

2) The coordinate of point P_1 is get, $X_{P_1} = \Delta\sigma.\sin(\alpha_{0_a}) + X_{P_0}$, $Z_{P_1} = \Delta\sigma.\cos(\alpha_{0_a}) + Z_{P_0}$

3) The point M_1 is set the middle of P_0P_1, and coordinate of point M_1 is get, $X_{M_1} = \frac{1}{2}(X_{P_0} + X_{P_1}) = \frac{1}{2}.\Delta\sigma.\sin(\alpha_{0_a}) + X_{P_0}$, $Z_{M_1} = \frac{1}{2}(Z_{P_0} + Z_{P_1}) = \frac{1}{2}.\Delta\sigma.\cos(\alpha_{0_a}) + Z_{P_0}$

4) The geocentric distance of point M_1 is got $P_{M_1} = (X_{M_1}^2 + Z_{M_1}^2)^{\frac{1}{2}}$, the height of M_1 is get $h_{M_1} = P_{M_1} - r_0$.

5) When the height h_{M_1}, elevation angle α_{0a} and azimuth angle φ are known, we can find the location of M_1 in the NWP model system. The

MET data in NWP grids can be interpolated to the location of M_1, then the interpolated MET data is used to get the refractivity of point M_1. The obtained refractivity $\mathrm{N}(h_{M_1})$ is also taken as the refractivity of linear element P_0P_1. Then the refractive index is set $\mathrm{n}(h_{M_1}) = 1 + 10^{-6}\mathrm{N}(h_{M_1})$.

6) The inject angel $\alpha_1 = \angle P_0P_1O = \alpha_{0a} - \theta_1$, when $\theta_1 = \tan^{-1}\left(\frac{X_{P_1}}{Z_{P_1}}\right)$. The integration result at first step is $\mathrm{STD} = \mathrm{STD} + \mathrm{N}(h_{M_1}).\Delta\sigma$.

Second step of FATIR method, is the integration from point P_1 to get P_2.

The Snell's Law is applied, $\mathrm{n}(h_{M_1})\sin\alpha_1 = \mathrm{n}(h_{M_2})\sin\alpha_1^{'}$, in which h_{M_2} and $\alpha_1^{'}$ are unknown. A iteration procedure is employed for h_{M_2} and $\alpha_1^{'}$:

1) The inject angle for P_1P_2 is set:

$$\left(P_1\overset{\frown}{P_2}OZ\right) = \alpha_1^{'} + \theta_1 \tag{4.2.3}$$

2) The coordinate of point P_2 is get, $X_{P_2} = \Delta\sigma.\sin(\alpha_{1_a}) + X_{P_1}$, $Z_{P_2} = \Delta\sigma.\cos(\alpha_{1_a}) + Z_{P_1}$, and $\theta_2 = \tan^{-1}\left(\frac{X_{P_2}}{Z_{P_2}}\right)$

3) The coordinate of middle point M_2 is get, $X_{M_2} = \frac{1}{2}(X_{P_1} + X_{P_2})$, $Z_{M_2} = \frac{1}{2}(Z_{P_1} + Z_{P_2})$, and geocentric distance of point M_2 is get $P_{M_2} = (X_{M_2}^2 + Z_{M_2}^2)^{\frac{1}{2}}$, the height of M_2 is get $h_{M_2} = P_{M_2} - r_0$.

4) Give a prior value of refractivity for M_2 by Exponential Distribution function, $\mathrm{N}(h_{M_2}) = N_0e^{-\frac{h_{M_2}}{H}}$, and refractive index is set $\mathrm{n}(h_{M_2}) = 1 + 10^{-6}\mathrm{N}(h_{M_2})$

5) The angle $\alpha_1^{'}$ is valued by $\alpha_1^{'*} = \sin^{-1}(\mathrm{n}(h_{M_1})\sin\alpha_1/\mathrm{N}(h_{M_2}))$

6) Give a threshold value $\varepsilon = 10^{-14}$, it's a experience value, usually it's smaller than 10^{-8}(Hobiger, 2009). When $\alpha_1^{'} - \alpha_1^{'*} > \varepsilon$, then let $\alpha_1^{'} = \alpha_1^{'*}$, repeat from the Eq.(4.2.3). Until $\alpha_1^{'} - \alpha_1^{'*} \leq \varepsilon$, the integration result is

$$\mathrm{STD} = \mathrm{STD} + \mathrm{N}\left(h_{M_2}\right).\Delta\sigma$$

The third step of FATIR method, is the integration from point P_i to P_{i+1}

At point P_i, the inject angle is set $\alpha_i = \alpha_{i-1a} - \theta_i$, then repeat from the Snell's Law in the Second step. . Let $i = 2, 3, \cdots, 202000$, integrated from receiver to the GPS satellite, we get the final result of STD. When the point $M_i$height h_{M_i} is higher than the top of NWP model we used, the MET data from climate model is used for calculate refractivity.

4.3 Precision of the Slant Total Delay by the Ray Tracing Algorithm

The Slant Total Delay (STD) and Slant Wet Delay (SWD) are estimated from the GPS data and integrated from MET data in 2010. The STD integrated from MET data will be compared with GPS post solutions. The main purpose of this experiment is to evaluate the precision of the integrated STD.

4.3.1 Experiment design

There are several Radiosonde stations in the East China region, and 8 stations are selected to obtain the MET data in this experiment (BFYH, BTLU, BTUZ, BXTC, SDHM, SDJM, SHBS and ZJHZ). The STD is integrated from the MET data from the Radiosonde station (i.e., RDS-STD) by a ray tracing algorithm. The MET data from the Radiosonde station are the observed data, and they will not bring additional errors into the integrated RDS-STD.

The 8 GPS stations near the Radiosonde stations are selected to estimate the STD from the GPS post solution (GPS-STD). 9 GPS stations from IGS in East Asia are also used in the data process. Double difference observations and Software GAMIT are used for the daily data process. IGS precise orbit products

are used in the post process.

For the GPS post solution, only the ZTD can be obtained. The GPS-STD can be reconstructed from the ZTD and other information in the GPS data process. The method for the GPS-STD is given in Section 4.3.2.

Meteorological Data

The Radiosonde is one of the main tools used to attain high accuracy atmospheric profiles, which gives results fit for two experiments in Greenwich time at 0 h and 12 h. Under ideal conditions, the Radiosonde accuracy is approximately 0.2 K for temperature, 5% (i.e., an increase in 25 °C) for relative humidity, and 2 hPa (i.e., a decrease of 500 hPa) for pressure (Rocken et al., 1997). The Radiosonde stations used in this chapter are distributed in East China during 2010 and 2011, with normal observations twice a day. Data will be added twice (at Greenwich times of 6 h and 18 h) for disaster weather, such as heavy storms and typhoons.

4.3.2 Method of GPS-STD retrieval

The Zenith Total Delays (ZTDs) are estimated from the GPS daily process, and the STD is reconstructed by modeling the ZTD. The Niell Mapping Functions (NMF) and the gradient model are used in the GAMIT software for daily processes, which are also used for the reconstruction of STD. The NMF model was introduced in section 3.4.3, and the gradient model is calculated by

$$D(e,\phi) = m(e)\left[G_N \cos(\phi) + G_E \sin(\phi)\right] \tag{4.3.1}$$

where e and ϕ are elevation and azimuth angles, respectively, and G_N and

G_E are the north-south and east-west gradients, respectively. $m(e)$ is the mapping function, which is calculated by

$$m(e) = 1/(\sin(e)\tan(e) + C), C = 0.003 \quad (4.3.2)$$

Therefore, the Total Slant Delay could be written as

$$STD = M_h(e)D_{hz} + M_w(e)D_{wz} + m(e)\left[G_N\cos(\phi) + G_E\sin(\phi)\right] + R_e \quad (4.3.3)$$

where D_{hz} and D_{wz} are the Zenith Dry Delay and the Zenith Wet Delay and $M_h(e)$ and $M_w(e)$ are the Niell dry and wet mapping functions, respectively. R_e is the residual of the observation.

Usually, the residual is caused by variations in atmosphere; if the residual is taken into account when reconstructing the STD, it will improve the precision, especially at low elevation angles. However, the residual can also be caused by other errors, such as a cycle slip, which will cause big errors in the STD reconstruction. In next experiment, the STD will be reconstructed both with and without residuals. The STD integrated from Radiosonde data is compared GPS-STD both with and without residuals.

4.3.3 GPS-STD with and without residuals

The distribution of the STD from GPS, both with and without residuals, is shown in Figure 4.3; blue triangles include residuals, and black points exclude residuals. The x-axis is the zenith distance (unit: degrees), and the y-axis is the STD (unit: m). The samples include all 8 stations for all days in 2010. The Zenith Distance is defined as 90 degrees subtract elevation angles.

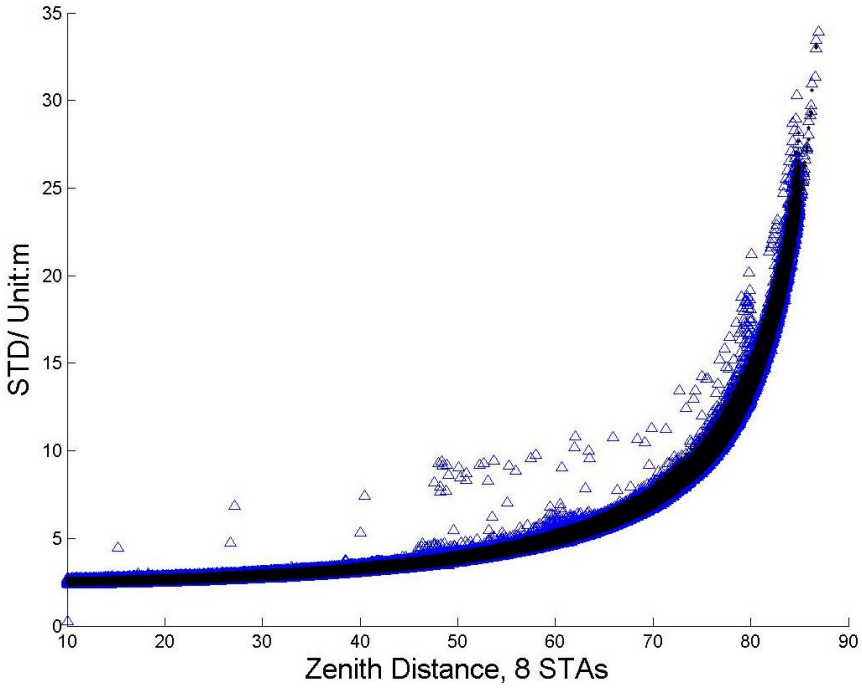

Figure 4.3: The distribution of STD from GPS with and without residuals

The STD from a different reconstruction model is shown in Figure 4.3; it seems that the model with residuals has more random error compared to the model without residuals.

4.3.4 RDS-STD compared with GPS-STD

Using the GPS estimated STD without residuals as the true value, differences between the STD from GPS and the Radiosonde data (GPS-RDS) are shown in Figure 4.4. The x-axis is the zenith distance (unit: degrees), and the y-axis represents differences in the STD (unit: cm). The samples include all 8 stations for all days in 2010.

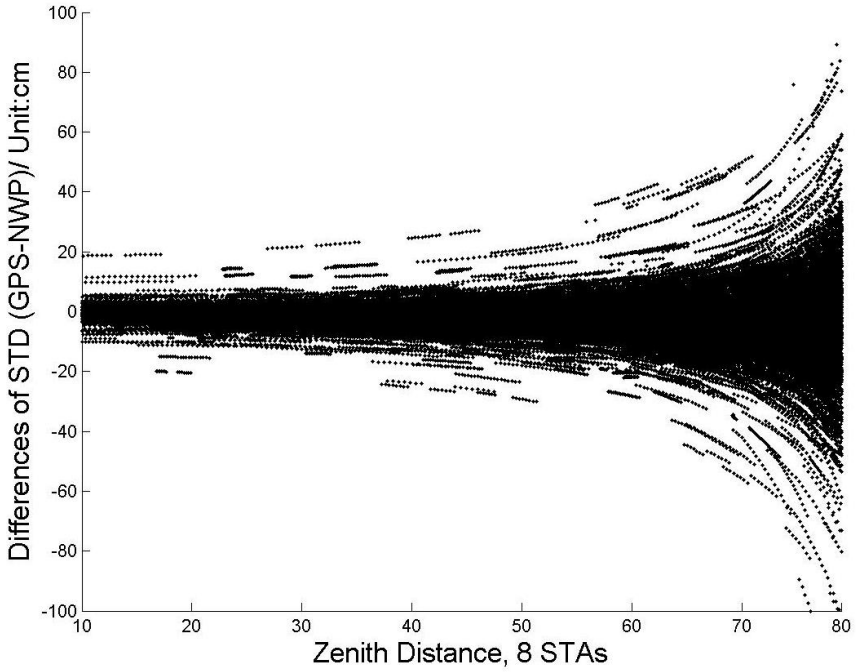

Figure 4.4: Differences between GPS-STD without residuals and RDS-STD (GPS-RDS)

The distribution of differences shows that a higher zenith distance has a higher bias; the main reason for this may be that the STD is higher with zenith distance. Therefore, statistics for absolute error, relative error, mean error and standard error are given to evaluate the precision of the RDS-STD.

Taking the GPS estimated STD without residuals as the true value, statistical differences between the STD from GPS and the Radiosonde data (GPS-RDS) are as follows:

Zenith Distance (degrees)	Max. Absolute Error (m) and its Relative Error		Mean Error (m)	Standard Error (m)	Number of Samples
85-80	2.2963	8.1543%	-0.0136	0.3902	3691
80-75	1.5695	12.1813%	-0.0213	0.2000	12652
75-70	0.7588	7.6166%	-0.0269	0.1235	10444
70-60	0.5548	7.6367%	-0.0177	0.0856	19982

60-40	0.3940	7.5964%	-0.0140	0.0525	28240
40-10	0.2509	7.6716%	-0.0103	0.0347	28587

Table 4.1: Differences between the GPS-STD without residuals and the RDS-STD

Statistical results show that the maximum relative error is approximately 8%, the mean error is approximately 1-2 cm, and the standard error is less than 20 cm when the zenith distance is smaller than 80 degrees.

Taking the GPS estimated STD with residuals as the true value, the differences between the STD from GPS and the Radiosonde data (GPS-RDS) are shown in Figure 4.5. The x-axis is the zenith distance (unit: degrees), and the y-axis shows differences in the STD (unit: cm). The samples include all 8 stations for all days in 2010.

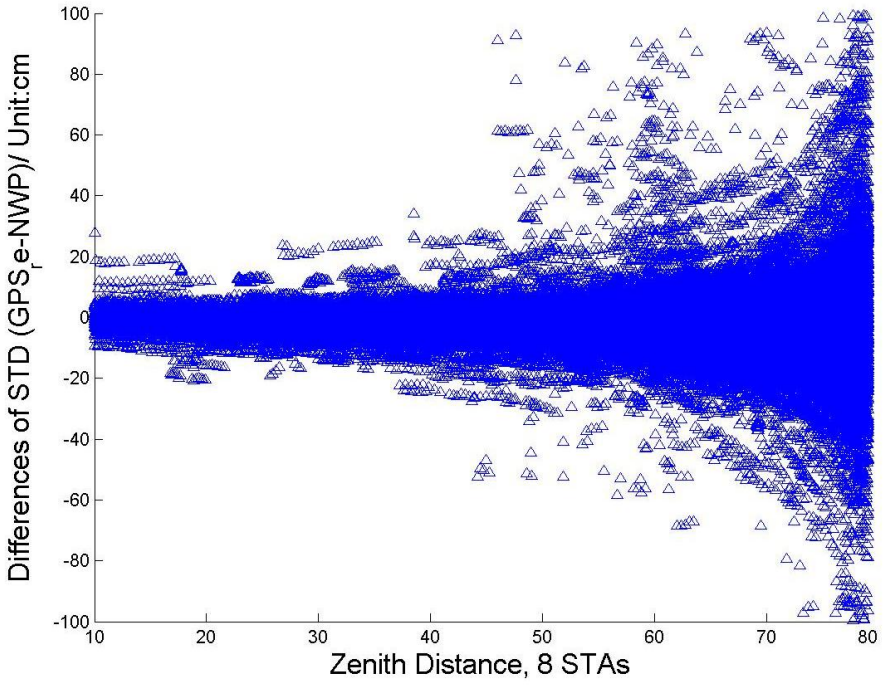

Figure 4.5: Differences between the GPS-STD with residuals and the RDS-STD (GPS-RDS)

Compared with Figure 4.4, a larger random bias in the high zenith distance (up to 50 degrees) is shown in Figure 4.5. The statistics for absolute error, relative

error, mean error and standard error are also given to evaluate the precision of the RDS-STD.

Taking the GPS estimated STD with residuals as the true value, statistics for differences between the STD from GPS and the RDS-STD (GPS-RDS) are shown as follows:

Zenith Distance (degrees)	Max. Absolute Error (m) and its Relative Error		Mean Error (m)	Standard Error (m)	Number of Samples
85-80	6.5229	30.7462%	0.0664	0.6396	2963
80-75	5.7074	30.8045%	0.0151	0.3909	12195
75-70	4.4735	33.2516%	-0.0203	0.1835	10382
70-60	5.1139	47.2254%	-0.0135	0.1461	19877
60-40	5.4383	57.9912%	-0.0057	0.1531	28156
40-10	4.1144	60.2295%	-0.0107	0.0468	28492

Table 4.2: Differences between the GPS-STD with residuals and the RDS-STD

The statistics show that when residuals are considered for the GPS-STD, it leads to large maximum absolute and relative errors. However, the mean error is approximately 1-2 cm, and the standard error is less than 40 cm when the zenith distance is smaller than 80 degrees.

4.4 The advantages of the FAIRT method

The bending of the GNSS signal is usually neglected, and the integration is along the geometric path between the receiver and satellite in many ray tracing algorithms. This will introduce a large error into the low elevation angle. When the bending is considered, the algorithm becomes more complex with more computations. The main purpose of this paper is to eliminate the tropospheric

effect in support of real-time, high-precision positioning. Accuracy and precision are both important when using the ray tracing method. The bending in the vertical direction is considered in the FAIRT method, and the exponential distribution function of refractivity is used as a prior value to accelerate the computation. In addition, the results of the STD are obtained for the different elevation angles (every 0.25 ° when the angle is lower than 5 °, every 0.5 ° when the angle lower than 15 °, and every 5 ° when the angle is higher than 15 °). When the solutions of the STD are obtained, the cubic spline interpolation can then be used to get the STD at any elevation angle. The solutions can then be used for the real-time mapping function, and more details are given in Section 4.5.

In the zenith direction, there is no bending. The accuracy and resolution of the MET data used are vital. On the one hand, different integration lengths are used for different heights, depending on the water vapor distribution. The vertical resolutions of the NWP model and Radiosonde observations are not good enough for the integration length. The meteorological models are used to obtain the MET data at the appointed height. On the other hand, the tropospheric delays over 10 hPa are considered in the FAIRT method. The top of the NWP model is usually 10 hPa, and the Radiosonde is observed at approximately 100 hPa. Sometimes, the Radiosonde is lacking observations when the balloon is in the sky. The climate model (Hopfield quartic profile in Chapter 3) is used to represent the upper atmosphere in this method. The integration for the tropospheric delays is along the GNSS signal until reaching the height of the GNSS satellite (such as 20200 km for the GPS signal).

The Radiosonde observation is used to describe the improvement of the FAIRT method in the zenith direction. In the old method, the integrated length was decided by the vertical resolution of MET data from the Radiosonde, and the tropospheric delays over 100 hPa were neglected. The ZTD integrated from a related method is called the Old-ZTD. The ZTD integrated by the FAIRT

method from Radiosonde observations is called the RDS-ZTD. The MET data for the year 2010 from the Radiosonde observations is used for both methods. The experiment is done for the entire year. Taking the ZTD estimated from the GPS post solutions as the reference, the errors of the Old-ZTD and RDS-ZTD are obtained for 8 stations in East China.

Stations	Standard Error (mm)		Number of Samples
	RDS-ZTD	OLD-ZTD	
BFYH	24.15	52.20	2097
BTLU	19.42	51.54	2058
BTUZ	18.22	44.80	2008
BXTC	32.12	77.52	2145
SDHM	28.77	36.10	2188
SDJM	20.16	34.86	2211
SHBS	20.61	49.04	1983
ZJHZ	22.80	45.99	2175

Table 4.3: The errors of ZTD from old method and FAIRT method

In Table 4.3, the standard error of ZTD from the FAIRT method is approximately 20 mm, and it is more than 40 mm for the ZTD from the old method. The vertical resolution is vital for the precision of the ZTD. The regional NWP model with high resolution is then used. More analysis about the ZTD precision is provided in Chapter 5.

4.5 The STD used for the Mapping Function

On the one hand, the STD can be used to eliminate the tropospheric effect along the GPS signals directly. On the other hand, the STD can be used to create the mapping function (MF) in real-time for the GPS data process.

Many MF models are also constructed for the GPS data processing. The global mapping function (GMF) is currently one of the most widely used model, and it is obtained from the global NWP data over a 40-year period with 15° ×15° grids. The GMF model is related to the day of year, location and height of the stations (Boehm, 2006).

The real-time MF can be obtained by dividing the ZTD by the STD, and the ZTD and STD are integrated from the MET data using the ray tracing algorithm in real-time. The modeled MF was generated from the climate MET data; thus, the real-time MF will have a higher precision. In this experiment, the STD and ZTD are integrated from Radiosonde data. The MF from Radiosonde (RDS-MF) data is defined as the integrated ZTD divided by the STD. The RDS-MF will be used as the reference, and the precision of the GMF model will be evaluated. The distribution of the RDS-MF and GMF are shown in Figure 4.6 (dry MF) and Figure 4.7 (wet MF), respectively.

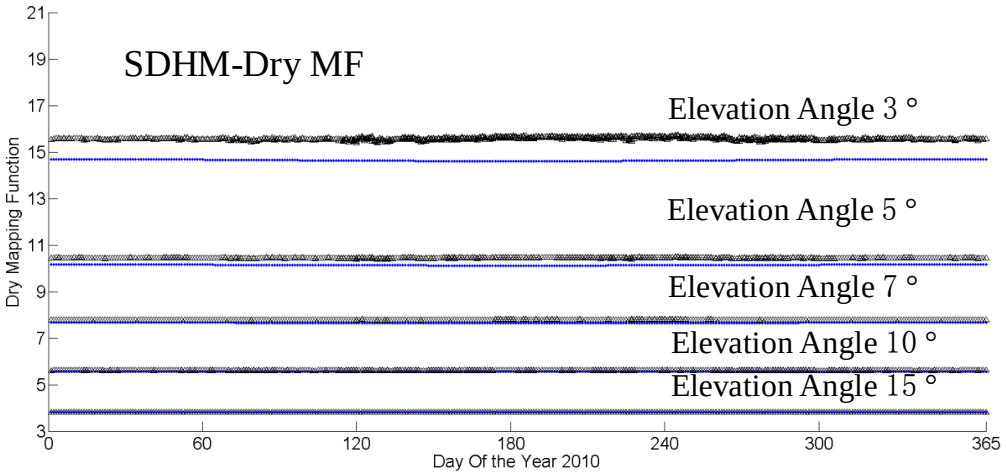

Figure 4.6: The distribution of the dry MF with different elevation angles (3,5,10,15 degree) from GMF (blue point) and RDS (black triangle) at Station SDHM for the year 2010

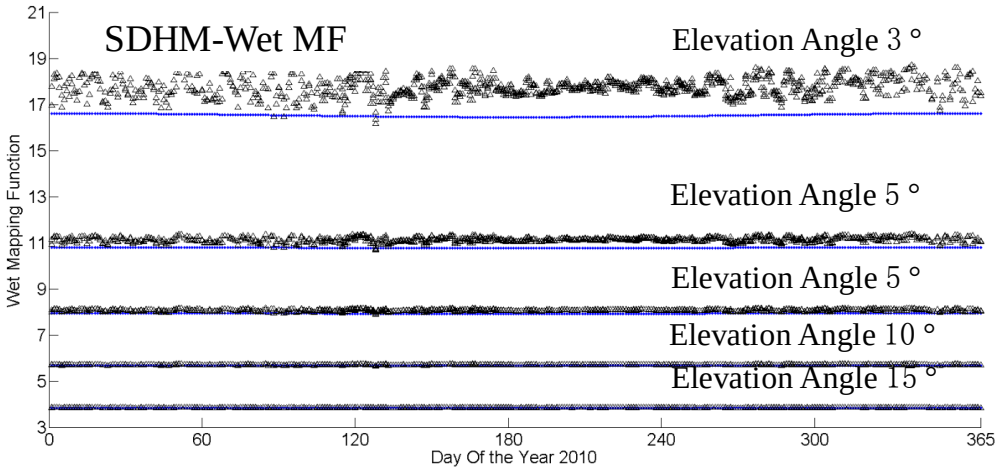

Figure 4.7: The distribution of wet MF with different elevation angles (3,5,10,15 degree) from GMF (blue point) and RDS (black triangle) at Station SDHM for the year 2010

Compared to the RDS-MF, both dry and wet GMF models show smaller seasonal variations. The wet RDS-MF changes more significantly in the winter and spring than at any other time. The main reason for is that the Radiosonde data is obtained at Greenwich Times 0 h and 12 h, and the daily changes in temperature are larger in the winter and spring, while the MF is affected more by the temperature (Yan, 1999; Yan, 2000).

Lower elevation angles show a larger bias between the RDS-MF and GMF. The RDS-MF is systematically larger than the GMF, especially when the elevation is less than 10 degrees. The statistics of the differences between the RDS-MF and GMF are shown in Table 4.4-1 (dry MF) and Table 4.4-2 (wet MF), respectively.

Stations	Angle 3 °	Angle 5 °	Angle 7 °	Angle 10 °	Angle 15 °
BFYH	0.961925	0.315398	0.135191	0.051370	0.016038
BTLU	0.934842	0.306888	0.131569	0.050002	0.015615
BTUZ	0.918478	0.302435	0.129845	0.049396	0.015436
BXTC	0.924214	0.302979	0.129789	0.049297	0.015390
SDHM	0.889931	0.295436	0.127252	0.048517	0.015185

SDJM	0.956085	0.314019	0.134727	0.051229	0.016002
SHBS	0.935799	0.307361	0.131793	0.050092	0.015645
ZJHZ	0.946666	0.309824	0.132646	0.050360	0.015715

(1)

Stations	Angle 3 °	Angle 5 °	Angle 7 °	Angle 10 °	Angle 15 °
BFYH	1.352976	0.389466	0.157214	0.057144	0.017294
BTLU	1.247162	0.362509	0.146843	0.053470	0.016182
BTUZ	1.263694	0.366345	0.148244	0.053957	0.016331
BXTC	1.197253	0.349688	0.141921	0.051748	0.015681
SDHM	1.238507	0.361868	0.146773	0.053471	0.016180
SDJM	1.436739	0.411000	0.165560	0.060128	0.018218
SHBS	1.296502	0.375657	0.152018	0.055351	0.016773
ZJHZ	1.247903	0.363287	0.147289	0.053695	0.016287

(2)

Table 4.4: The statistics of dry (1) and wet (2) MF with different elevation angles (3,5,7,10,15 degree) from GMF and RDS (RDS-GMF) at 8 Stations for the year 2010.

The GMF model shows a rather large bias at elevation angles of 3 ° and 5 °, and the bias of the MF at 7 ° is approximately 1%. The cut angle setting in the GAMIT software for our GPS post solution is 7 °. A smaller MF may lead to a larger GPS-ZTD in the GPS data processing. The GPS post solution is taken as the referenced data in this article, and it may have the bias in the low elevation observations.

Chapter 5 The analysis and improvement for tropospheric delays from NWP models

5.1 Introduction

One of the main sources of error in post-processed Global Positioning System (GPS) solutions is the tropospheric effect on precise GPS positioning. When orbits can be well predicted, the ionospheric effect can be eliminated using an ionosphere-free combination, and most errors are well modeled (Zamberge et al., 1993; Rocken et al., 2000). The ambiguities will be resolved quickly, and the convergence period of the GPS data processing will be decreased when the tropospheric effects are significantly reduced (Zamberge et al., 1997).

The effects of the troposphere can be divided into dry and wet delays. Although water vapor is a small part of the atmosphere, the refractivity of water vapor is approximately 17 times than that of dry air (Businger et al., 1996). The dry delays can be well modeled by most tropospheric correction models, but the wet delays cannot be well modeled. The method that is widely used in precise GPS data processing is to estimate the tropospheric effect as an unknown parameter. However, it takes a rather long time for the convergence to occur, and this makes the real-time positioning impossible. Therefore, the tropospheric correction is important for precise GPS real-time positioning, especially for a wide area range network.

The Radiosonde is the conventional instrument used to detect atmosphere. It is used for its vertical resolution and accuracy to establish the tropospheric model. Herring (1992) used ten Radiosonde stations to form mapping functions, and this is called the MTT model. A widely used mapping function is the NMF model (Niell, 1996), which uses 26 globally distributed Radiosonde data. Today,

an increasing amount of near real-time and predicted meteorological (MET) data are used for tropospheric correction. The data from the Numerical Weather Prediction (NWP) model is one of the best choices because of its high temporal and spatial resolutions (Ghoddousi-Fard R., 2009b).

The MET data from the NWP model could be well predicted over the following 72 hours, and it could be used to obtain the ZTD for tropospheric correction. On the one hand, the NWP data can be used to establish the new global and regional empirical ZTD model. Song (2011) has established a new regional tropospheric model based on the NWP model for the China area, and the ZTD from the model is improved by 65% compared to the global model. On the other hand, the NWP data can be used to integrate the ZTD directly by ray tracing (Pany, 2002; Jensen, 2002). The next-generation mapping functions can be based on high resolution NWP models alone, and these include the isobaric mapping function (NMF) (Niell, 2001), Vienna mapping function (VMF) (Boehm and Schuh, 2004) and the VMF improved version, VMF1 (Boehm et al., 2006a). The global mapping function (GMF) was then developed, which combined the accuracy of the VMF1 and the coverage of NMF (Boehm et al., 2006b). The NWP model could also be used for the STD of the GPS signal to eliminate the tropospheric effects, and the repeatability of the coordinates could be improved in GPS positioning (Eresmaa et al., 2006; Nordman et al., 2007).

Comparing Chen's (2012) analysis of the integrated ZTD over Asia for 49 GPS stations in 2004 with the ZTD estimated by GPS station, the RMSE values of the integrated ZTD based on the two different global NWP models are 27 mm and 68 mm, respectively. If the tropospheric delay could be eliminated directly in real-time, it would make high-precision GPS real-time positioning possible. The tropospheric delay is described by the ZTD and mapping function, so the accuracy of the ZTD is important, while the mapping function is well developed. In previous research, the integrated ZTD was not analyzed for a long time, or the

precision of the integrated ZTD was not sufficiently good. The reliability and applicability of the integrated ZTD is also not analyzed. The aim of this article is to analyze the long time, serious integrated ZTD from the NWP model and to check when the tropospheric delays could be directly eliminated to match the wide range of real-time high precision GPS positioning. Both the MET data from the high-resolution regional NWP model and the Radiosonde from the East China region are used to integrate the ZTD using the ray tracing algorithm. Compared with the ZTD integrated from the Radiosonde (RDS-ZTD), the precisions of the ZTD estimated from GPS stations (GPS-ZTD) and the ZTD integrated from the NWP model (NWP-ZTD) are both evaluated. The yearly and monthly differences between the GPS-ZTD and NWP-ZTD are also analyzed. Finally, taking the GPS-ZTD as the reference, the correlations between the NWP-ZTD errors and rainfall are analyzed.

5.2 The analysis and discussion of precision for NWP-ZTD

The experiments for the precision analysis are divided into the following parts: 1) evaluate the precisions of the GPS-ZTD from GPS solutions and the NWP-ZTD integrated from the regional NWP model using the RDS-ZTD integrated from the Radiosonde observation (RDS-ZTD); 2) estimate the differences between the GPS-ZTD and NWP-ZTD; and 3) discuss the major differences between the GPS-ZTD and NWP-ZTD, and what leads to these differences.

There are 8 Radiosonde stations used in the north-central part of the East China region, and the nearest GPS stations are selected for comparison. The NWP data will be interpolated to the location of the GPS stations in each grid. The 8 Radiosonde stations used and the nearest 8 GPS stations are shown in Figure 5.1. The GPS stations BTUZ, SHBS and ZJHZ are at the same locations as the Radiosonde, and the others are a little farther from the Radiosonde. The farthest GPS station is the SDHM, which is approximately 85 km away from the

Radiosonde.

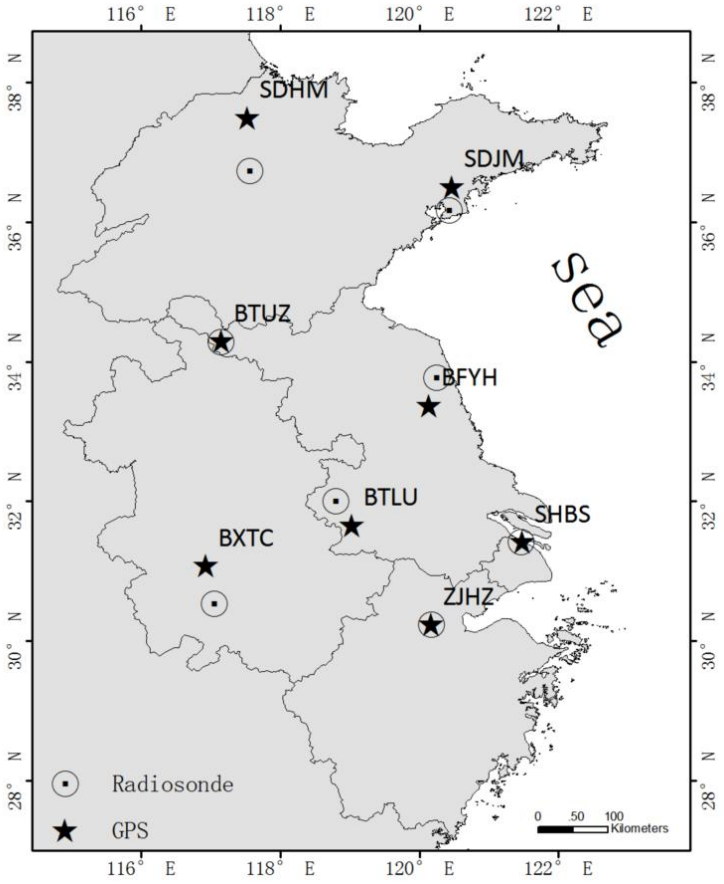

Figure 5.1: The distribution of GPS and Radiosonde stations

Double difference observations and the software GAMIT from the Massachusetts Institute of Technology (MIT) are used for the daily GPS data post processing, with 48 tropospheric parameters per day. The precise orbit data from the International GPS Service (IGS) and 9 IGS stations in East Asia are used for the experiments, which include BJFS, DAEJ, IRKT, KUNM, SHAO, SUWN, TSKB, USUD and WUHN.

The numerical weather prediction data used here is the main medium-range model from the Shanghai Meteorological Bureau (SMB). The model covers the East China area, and its spatial resolution is 9 km, with 35 vertical levels, and the top model is 50 hPa. The temperature bias between the Radiosonde and the

model at station SHBS (located in north Shanghai) in 2010 is 1.75 ℃, and the geo-potential height bias at 500 hPa is 1.11 gpdm. This information is supplied by the Shanghai Typhoon Institute, SMB.

5.2.1 Precision of the integrated yearly ZTD from GPS solutions

The Radiosonde is normally observed twice a day at Greenwich Times 0 h and 12 h, and two more observations, at 6 h and 18 h, are added during the rainy season (from June to September) for 2010, which is used to support weather service for the Shanghai World Exposition. The MET data from the Radiosonde is the observation, and the RDS- ZTD integrated from the Radiosonde by ray tracing is used as the reference data to evaluate the GPS-ZTD from the daily GPS post-processed solution. The GPS-ZTD is estimated each hour by the GPS post-processed solution, and the precision of the GPS-ZTD is given as follows.

- **The distributions of the ZTD**

The GPS-ZTD is compared with the RDS-ZTD for the year 2010, and the results for station BXTC (from Anhui Province) and ZJHZ (from Zhejiang Province) are shown in Figures 5.2 and 5.3. These two stations are in the south part of the region, which are supposed to be more affected by the water vapor from the Bay of Bengal. In Figures 5.2 and 5.3, the blue lines are the GPS-ZTD, and the red points represent the RDS-ZTD for the year 2010. The x-axis is the day of the year, and the y-axis is the ZTD (unit: cm).

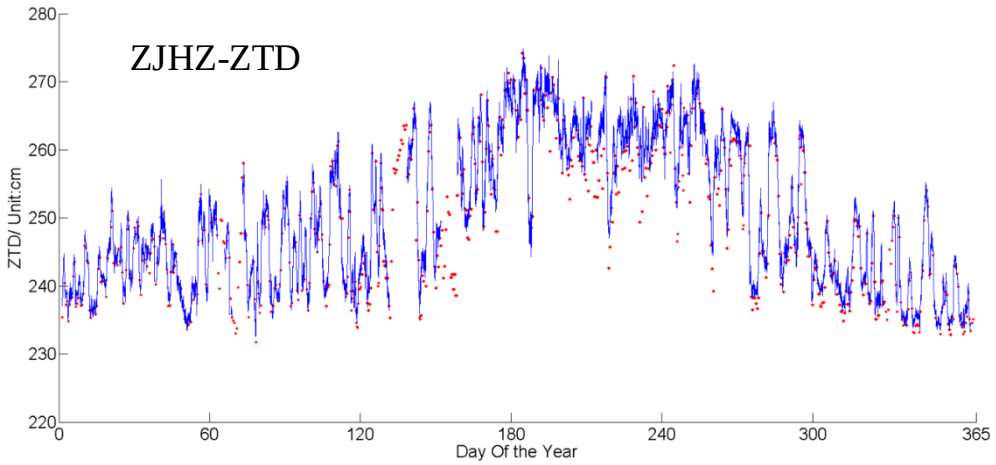

Figure 5.2: The GPS-ZTD (lines) compared with RDS-ZTD (points) at station ZJHZ in 2010

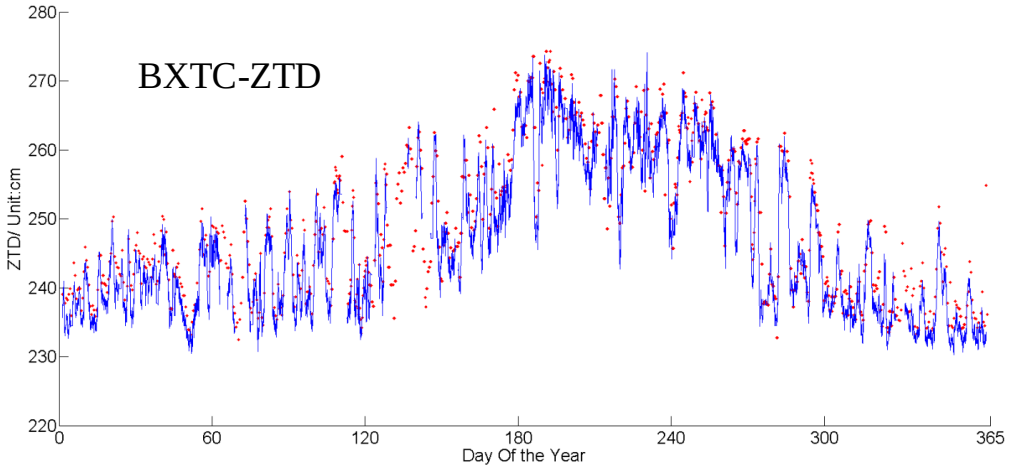

Figure 5.3: The GPS-ZTD (lines) compared with RDS-ZTD (points) at station BXTC in 2010

Based on Figures 5.2 and 5.3, the ZTD shows yearly changes from 230 cm to 275 cm. The GPS-ZTD is generally fit to the RDS-ZTD, and the statistical differences between the GPS-ZTD and RDS-ZTD will be given in Section 3.1.2.

- **Statistical tropospheric errors from GPS for the years 2010 and 2011**

Taking the RDS-GPS from the Radiosonde as a reference, statistical errors for the GPS-ZTD at 8 GPS stations for the year 2010 are shown in Table 5.1. The mean error and the root mean square error (RMSE) are listed for the statistics.

Observations for which the biases are 2 times larger than RMSE are removed from the statistics.

Stations	Mean Error(mm)	RMSE (mm)	Number of Samples	Number of Large Errors and Relativity	
BFYH	-3.31	24.09	2097	47	1.81%
BTLU	-2.35	19.26	2058	117	5.15%
BTUZ	-6.60	17.94	2088	123	5.31%
BXTC	-20.16	31.80	2145	100	4.75%
SDHM	9.47	27.62	1891	98	5.38%
SDJM	5.35	21.67	1697	96	5.28%
SHBS	6.14	20.90	1877	86	4.56%
ZJHZ	9.57	23.00	2175	115	5.53%

Table 5.1: The precision of GPS-ZTD in 2010 (GPS-RDS)

The same method is used for the year 2011 for the 8 stations. There is much less Radiosonde data in 2011 than in 2010 because four observations per day were collected only for the few days of disaster weather. The statistics of the whole year for the 8 stations are shown in Table 5.2.

Stations	Mean Error(mm)	RMSE (mm)	Number of Samples	Number of Large Errors and Relativity	
BFYH	13.76	30.73	916	23	2.51%
BTLU	11.38	26.90	484	22	4.55%
BTUZ	7.45	23.27	498	24	4.82%
BXTC	-1.94	30.77	859	14	1.63%
SDHM	14.84	32.74	806	7	0.87%
SDJM	18.47	34.75	716	3	0.42%
SHBS	4.88	25.18	892	23	2.58%

ZJHZ	14.90	25.26	391	7	1.79%

Table 5.2: The precision of GPS-ZTD in 2011 (GPS-RDS)

The statistical results show that RMSE of the GPS-ZTD is approximately 20-30 mm. The RMSE of stations BXTC and SDHM is a little larger than the others in both 2010 and 2011, which have slightly longer distances between the GPS and Radiosonde stations. For stations BTUZ, SHBS and ZJHZ, for which the GPS are exactly located in the Radiosonde station, show a smaller RMSE, of less than 20 mm in 2010 and approximately 25 mm in 2011.

- **Precision of GPS-ZTD during the rainy season for the year 2010**

The rainy season is usually from June to September in the East China region. During this time, water vapor is abundant in the atmosphere, and heavy storms occur much more often than during other seasons. The Radiosonde observations are twice as frequent during the rainy season for the year 2010 (4 times per day, UTC 00 h, 06 h, 12 h, 18 h). The same statistics of the GPS-ZTD during the rainy season for 2010 are made for the 8 stations, and the results are shown in Table 5.3.

Stations	Mean Error(mm)	RMSE (mm)	Number of Samples	Number of Large Errors and Relativity	
BFYH	-5.71	33.24	885	17	1.36%
BTLU	-1.53	24.86	878	47	5.47%
BTUZ	-6.74	23.15	862	51	5.58%
BXTC	-22.65	36.30	932	50	5.41%
SDHM	10.70	39.34	706	33	4.54%
SDJM	7.03	29.48	721	40	4.17%
SHBS	6.20	23.61	934	52	4.31%

ZJHZ	11.56	30.23	900	49	4.93%

Table 5.3: The precision of GPS-ZTD during the rainy season in 2010 (from day 152 to 273, June to September)

In Table 5.3, the RMSE for stations BXTC and SDHM are a little larger, and others are almost the same level. Although water vapor is only a small part of the atmosphere, less than 5% even in the tropics (Janes et al., 1991), wet delays are approximately 15-20% of the total delays during the rainy season. Relative to the statistical results of the whole year for 2010, larger RMSEs are shown during the rainy season for all 8 stations. It seems that the precision of the GPS-ZTD is affected by the water vapor.

5.2.2 Precision of the integrated ZTD from the NWP model

The Radiosonde is the most conventional instrument used to obtain the vertical distribution of the troposphere. The atmospheric profiles obtained from the Radiosonde are highly accurate, but its temporal and spatial resolution is low, and it is expensive. The observations from the Radiosonde are normally made twice a day, and the spatial resolution is approximately 300-500 km, even in the East China region, which is much better developed than most areas in China. It seems that the MET data from high-resolution NWP model is a better choice for the integrated ZTD.

The NWP model is the prediction for atmospheric parameters, and it may not be as accurate as the Radiosonde. It is necessary to analyze the precision of the ZTD integrated from the NWP model. The MET data from the NWP model is interpolated to the 8 Radiosonde stations and used to integrate the NWP-ZTD. Taking the RDS-ZTD from the Radiosonde as reference, the statistical precision of the NWP-ZTD at 8 stations for the year 2010 are shown in Table 5.4. The mean error and RMSE are the statistics listed. The observations are removed from the statistics as the biases are 2 times larger than the RMSE.

Stations	Mean Error(mm)	RMSE (mm)	Number of Samples	Number of Large Errors and Relativity	
BFYH	4.60	24.44	2306	66	2.86%
BTLU	-1.59	20.77	2306	146	6.33%
BTUZ	4.73	19.94	2306	148	6.42%
BXTC	21.96	35.41	2306	116	5.03%
SDHM	-0.51	26.23	2306	128	5.55%
SDJM	-2.54	21.86	2316	138	5.96%
SHBS	-9.65	26.47	2152	116	5.39%
ZJHZ	-12.50	27.84	2308	142	6.15%

Table 5.4: The precision of NWP-ZTD in 2010 (NWP-RDS)

Table 5.4 shows that RMSE of the NWP-ZTD is approximately 25-35 mm for the year 2010, which is the same level as the GPS-ZTD. The RMSE of stations BXTC, SHBS and ZJHZ is larger than the others. The main reason for this is that the 3 stations are in a more southern area, and the water vapor in this area is greater than in the northern area. For station BXTC, it is in the mountainous area of the south Anhui Province, which has more rainstorms during the rainy season.

5.2.3 The differences between GPS-ZTD and NWP-ZTD

The precisions of the GPS-ZTD and NWP-ZTD have been estimated by comparison with the RDS-ZTD, and they are both approximately 20-30 cm. The main purpose of the experiment is to see if the NWP-ZTD could be used instead of the GPS-ZTD in the positioning. The differences between the GPS-ZTD and NWP-ZTD are discussed.

- **Statistical errors of NWP-ZTD for the year 2010**

The MET data from the NWP model are interpolated to the same 8 GPS stations and used to integrate the NWP-ZTD. The differences between the GPS-ZTD and NWP-ZTD at 8 stations for the year 2010 are shown in Table 5.5. The GPS-ZTD is taken as the reference here, and the mean error and RMSE of NWP-ZTD are listed for the statistics. These observations are removed from the statistics because the biases are 2 times larger than the RMSE.

Stations	Mean Error(mm)	RMSE (mm)	Number of Samples	Number of Large Errors and Relativity	
BFYH	0.09	15.85	5080	293	5.77%
BTLU	-3.38	16.97	5023	290	5.77%
BTUZ	-2.64	15.49	5101	287	5.63%
BXTC	1.47	16.62	5288	305	5.77%
SDHM	10.45	19.12	5239	295	5.63%
SDJM	0.63	15.22	5608	312	5.56%
SHBS	-5.00	19.78	4923	252	5.12%
ZJHZ	-3.16	16.74	5366	330	6.15%

Table 5.5: Differences between GPS-ZTD and NWP-ZTD in 2010 (GPS-NWP)

In Table 5.5, the differences between the GPS-ZTD and NWP-ZTD at all 8 stations are less than 20 mm. The MET data from the NWP model has a much higher spatial resolution than that from the Radiosonde, and the NWP data used in Table 5.5 are interpolated to the location of the GPS station. Thus, all the stations have a similar RMSE.

In the East China region, the water vapor in the atmosphere and the rainfall both have seasonal variations. Taking the GPS-ZTD as a reference, the RMSE of the NWP-ZTD for all stations during each month are listed in Table 5.6.

Month	RMSE of each station in each month (mm)							
	BFYH	BTLU	BTUZ	BXTC	SDHM	SDJM	SHBS	ZJHZ
Jan.	7.81	9.94	7.52	10.32	10.13	8.64	11.93	11.36
Feb.	11.05	14.82	11.32	12.12	8.78	11.55	14.61	13.16
Mar.	13.95	16.92	13.55	12.83	14.40	11.80	14.81	13.99
Apr.	10.86	17.92	14.96	14.59	15.70	15.40	19.62	20.19
May	20.09	23.69	18.67	25.43	26.52	16.55	23.36	24.11
Jun.	23.64	27.82	25.98	20.83	28.61	18.84	24.68	25.02
Jul.	31.44	24.80	25.36	26.37	31.92	25.01	30.29	26.47
Aug.	19.52	19.75	22.69	25.84	30.90	24.57	21.62	18.41
Sep.	22.25	19.31	20.63	19.15	22.16	21.88	21.65	21.93
Oct.	14.93	13.94	12.78	16.39	17.91	13.83	15.75	13.33
Nov.	7.73	10.04	6.67	12.80	17.95	9.16	16.69	10.82
Dec.	7.90	7.74	7.04	8.22	11.06	7.38	15.22	8.20

Table 5.6: Differences between GPS-ZTD and NWP-ZTD for each month in 2010

In Table 5.6, the differences between the GPS-ZTD and NWP-ZTD for all stations show significant seasonal variations. From October to March, the water vapor is lower in the atmosphere, and the RMSE of most stations is less than 15 mm, especially in December and January (less than 10 mm). During the rainy season, from June to September, the RMSE for most stations is much larger (more than 25 mm).

- **Statistical errors of PWV from NWP model in year 2010**

The ZTD is divided into Zenith Hydrostatic Delay (ZHD) and Zenith Wet Delay (ZWD). The ZHD could be well modeled from the atmospheric pressure on the ground and was better than 1 mm (Businger et al., 1996; Liu et al., 2010).

The ZWD is obtained from equation 5.3.1:

$$ZWD = ZTD - ZHD \tag{5.2.1}$$

The ZWD could be transferred to the precipitable water vapor (PWV), which is defined as the height of an equivalent column of liquid water in the atmosphere (Bevis et al., 1992). The same statistics are completed for the PWV for the year 2010.

In Table 5.7, the statistical differences between the PWV from GPS (GPS-PWV) and the NWP model (NWP-PWV) at 8 stations for the year 2010 are shown. The GPS-PWV is taken as the reference, and the differences between the GPS-PWV and NWP-PWV are taken as the errors of NWP-PWV. The RMSE of all 8 stations for each month are listed in Table 5.8. The observations are removed from the statistics because the biases are 2 times larger than the RMSE.

Stations	Mean Error(mm)	RMSE (mm)	Number of Samples	Number of Large Errors and Relativity	
BFYH	-0.02	2.52	5080	297	5.84%
BTLU	0.53	2.70	5023	294	5.85%
BTUZ	0.41	2.47	5101	291	5.70%
BXTC	-0.23	2.63	5288	312	5.90%
SDHM	-1.64	3.02	5239	304	5.80%
SDJM	-0.11	2.41	5608	315	5.62%
SHBS	0.80	3.16	4923	251	5.10%
ZJHZ	0.57	3.11	5366	92	1.71%

Table 5.7: Differences between GPS-PWV and NWP-PWV in 2010

Month	RMSE of each station in each month (mm)							
	BFYH	BTLU	BTUZ	BXTC	SDHM	SDJM	SHBS	ZJHZ
Jan.	1.18	1.52	1.14	1.58	1.52	1.30	1.83	1.74

Feb.	1.68	2.29	1.74	1.84	1.33	1.75	2.26	2.05
Mar.	2.16	2.62	2.12	1.97	2.22	1.81	2.30	2.59
Apr.	1.70	2.82	2.34	2.31	2.46	2.40	3.07	3.17
May	3.21	3.75	2.99	4.06	4.25	2.63	3.71	3.89
Jun.	3.82	4.48	4.23	3.37	4.44	3.01	3.98	4.02
Jul.	5.11	4.04	4.12	4.30	5.19	4.06	4.93	4.29
Aug.	3.18	3.23	3.70	4.20	5.04	3.98	3.56	3.02
Sep.	3.54	3.01	3.32	3.08	3.53	3.54	3.50	3.49
Oct.	2.36	2.21	2.03	2.62	2.82	2.18	2.51	2.12
Nov.	1.20	1.57	1.04	2.00	2.77	1.41	2.61	1.70
Dec.	1.21	1.20	1.08	1.26	1.68	1.13	2.34	1.26

Table 5.8: Differences between GPS-PWV and NWP-PWV for each month in 2010

The RMSEs of the NWP-PWV for all 8 stations are less than 3 mm for 2010, and stations SHBS and ZJHZ have a slightly larger error, as they are in the south area, with more water vapor. In Table 5.8, the monthly RMSE of NWP-PWV also shows the seasonal changes, as in Table 5.6.

The changes of water vapor in the atmosphere lead to the seasonal changes of the RMSE for the NWP-PWV. In the summer, the NWP-PWV shows larger differences, but the total PWV in the summer is also larger than in other seasons. The relative error is obtained from the absolute RMSE of the NWP-PWV divided by total PWV. The relative errors of the NWP-ZTD are also discussed in Table 5.9.

Month	Relative RMSE of each station in each month (mm)							
	BFYH	BTLU	BTUZ	BXTC	SDHM	SDJM	SHBS	ZJHZ
Jan.	12.26%	11.77%	13.91%	11.41%	25.14%	17.03%	12.99%	10.60%
Feb.	11.53%	12.84%	13.01%	10.09%	14.03%	20.30%	12.74%	9.89%

Mar.	12.93%	13.04%	14.33%	8.98%	20.89%	18.40%	10.04%	5.63%
Apr.	13.30%	15.24%	15.42%	9.29%	18.36%	18.92%	12.79%	11.08%
May	11.14%	10.65%	11.05%	10.43%	17.28%	11.55%	11.14%	10.23%
Jun.	11.60%	10.57%	11.84%	7.64%	13.48%	9.78%	9.20%	7.66%
Jul.	9.30%	6.48%	7.71%	6.76%	10.98%	8.42%	8.26%	6.79%
Aug.	5.61%	5.71%	6.75%	7.78%	10.01%	7.37%	6.26%	5.19%
Sep.	7.72%	6.00%	7.57%	5.83%	9.35%	8.88%	6.95%	6.30%
Oct.	11.52%	8.66%	11.48%	10.13%	18.03%	13.28%	8.48%	6.50%
Nov.	11.55%	11.58%	11.77%	15.24%	37.74%	17.15%	13.92%	9.38%
Dec.	14.16%	11.47%	15.47%	11.47%	33.94%	19.49%	20.91%	8.78%

Table 5.9: Relative differences between GPS-PWV and NWP-PWV for each month in 2010

The PWV changes significantly throughout the whole year, and it is usually 60-80 mm in summer, and less than 10 mm in winter (Wang et al., 1999; Yang et al., 2008). In Table 5.9, the relative differences between the GPS-PWV and NWP-PWV during the rainy season are smaller than others. The main reason is that the differences between the GPS-PWV and NWP-PWV is a little larger during the rainy season (2-3 mm), but the absolute PWV is much larger during the rainy season.

5.2.4 The discussion of the large errors for NWP-ZTD

- **The precision of the NWP-ZTD during rainy and no rain periods**

The GPS-ZTD are taken as the reference, and the differences between the GPS-ZTD and NWP-ZTD are taken as the errors of NWP-ZTD. The yearly precision of the NWP-ZTD for 8 stations has been analyzed. It seems that the precision of the NWP-ZTD is affected greatly by the water vapor in the atmosphere. If it is rainy, it means there is plenty of water vapor in the atmosphere. Therefore, the observations of NWP-ZTD are divided into rainy and

no rain periods. The RMSE of the NWP-ZTD with rain and without rain is analyzed, and the statistics are shown in Table 5.10.

Stations	Yearly	Rain		No Rain	
	RMSE (mm)	RMSE (mm)	Number of Samples	RMSE (mm)	Number of Samples
BFYH	15.85	20.66	1063	14.62	4017
BTLU	16.97	20.11	1220	15.95	3803
BTUZ	15.49	20.86	806	14.52	4295
BXTC	16.62	17.96	1449	16.11	3839
SDHM	19.12	24.30	765	18.39	4474
SDJM	15.22	24.01	751	13.98	4857
SHBS	19.78	21.95	1266	19.04	3657
ZJHZ	16.74	19.41	1768	15.39	3598

Table 5.10: Differences between GPS-ZTD and NWP-ZTD in the hours with and without rain in 2010

As shown in Table 5.10, the observations of the NWP-ZTD without rain are approximately 80% of the total observations, and the other 20% are the NWP-ZTD with rain. The yearly RMSEs for all stations are also listed in the table, and are approximately 15-20 mm. The RMSE of the NWP-ZTD with rain is approximately 20-25 mm, approximately 5 mm larger than the yearly RMSE. The rainfall affects the precision of the NWP-ZTD; therefore, the correlation between the NWP-ZTD and rainfall is discussed.

- **The correlation between the NWP-ZTD errors and rainfall**

The PWV is correlated to the rainfall in the coming 3-6 hours and is significant to the rainfall now-casting (Ye et al., 2008). The changes of the PWV lead to the variations in the ZTD. The ZTD is approximately 2.3 m in the East China region,

and the ZWD is approximately 3%~30% of the ZTD in different seasons (Yang et al., 2008). How does the rainfall affect the ZTD throughout the whole year?

The 6-hour rainfall from the nearest MET station is used to analyze how the rainfall affects the precision of the NWP-ZTD at 8 stations. Additionally, the GPS-ZTD is taken as the reference, and the differences between the GPS-ZTD and NWP-ZTD are taken as the errors of the NWP-ZTD. The distributions of errors for the NWP-ZTD and 6-hour rainfall are shown in Figure 5.4 and Figure 5.5.

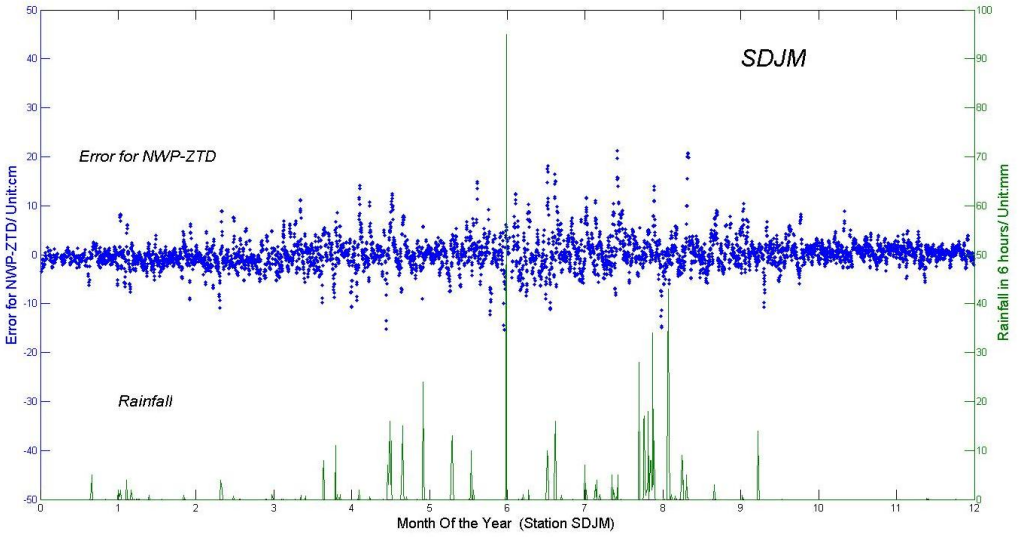

Figure 5.4: The RMSE of NWP-ZTD and 6-hour rainfall at station SDJM in 2010

The station SDJM is in the northern part of the East China region, and the rainfall has definite variations between the seasons. Figure 5.4 shows that there is only drizzle in the spring and almost no rainfall in the winter. The errors in the NWP-ZTD in the spring and winter are also much smaller than in the other seasons. On the contrary, the rainfall is much greater, and the errors of the NWP-PWV are much larger from middle May to the middle of September at station SDJM.

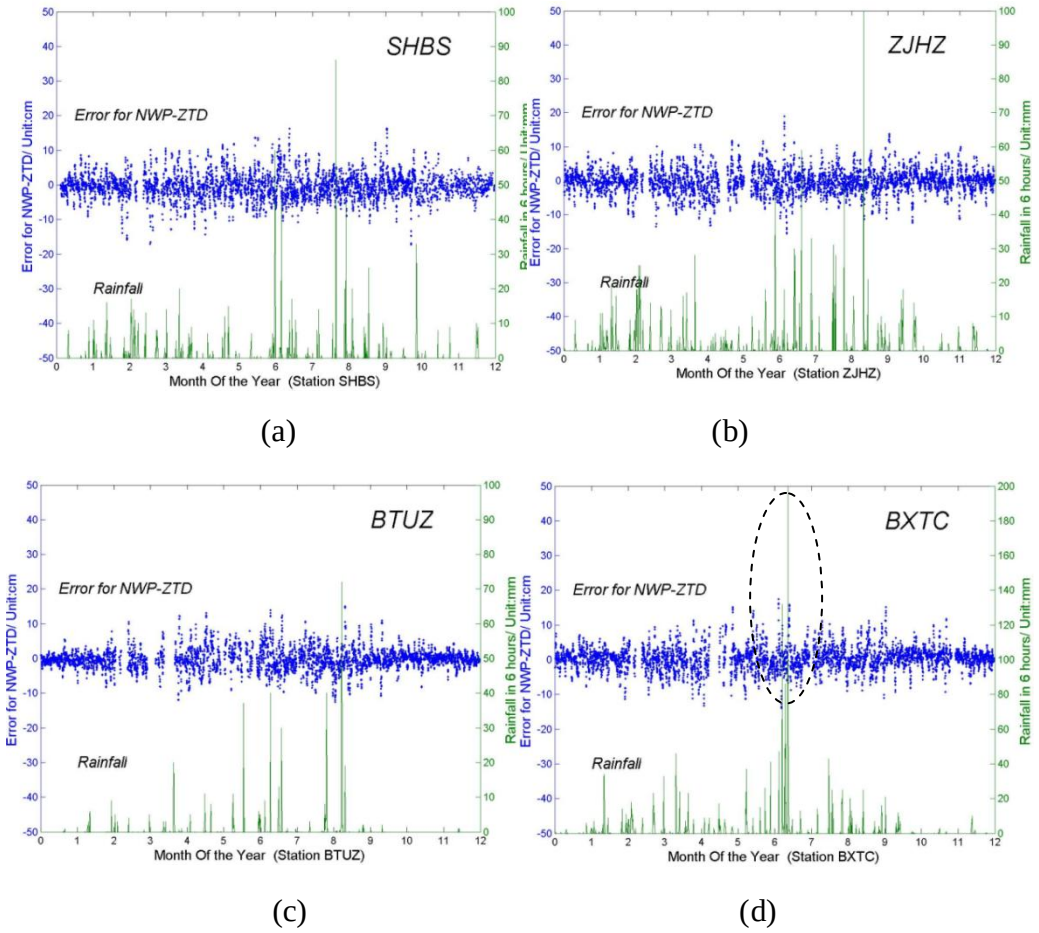

Figure 5.5: The RMSE of NWP-ZTD and 6-hour rainfall for 4 stations in 2010

Similar results are shown in Figure 5.5; the errors of the NWP-ZTD at all stations are related to the 6-hour rainfall. Stations SHBS and ZJHZ are in the more southern area and close to the sea (see Figure 5.1), where the rainfall lasted the whole year in 2010, and the RMSE of NWP-ZTD is almost the same throughout the whole year. For station BTUZ, there is no rain in the winter and early spring, and the RMSE of the NWP-ZTD is much smaller than any other time.

For the heavy storms, such as the rainfall at station BXTC in early July, the 6-hour rainfall is over 50 mm and lasts for a few days. The largest amount of rainfall is near 200 mm, see the cycle part in Figure 5.5(d). The RMSE of NWP-ZTD during the heavy storm is larger than other days, but it is not much larger. Therefore, it seems that the precision of the NWP-ZTD is more correlated

to the frequency of the rainfall and less correlated to the amount of the rainfall. The main reason may be because the water vapor is only at 3% in the atmosphere.

- **The analysis for large errors of NWP-ZTD**

In the former statistics, if the differences between the GPS-ZTD and NWP-ZTD are more than twice the RMSE, the observations will be removed. The GPS-ZTD is taken as the reference, and the differences between the GPS-ZTD and NWP-ZTD are taken as the errors of NWP-ZTD. The error of NWP-ZTD will be taken as the large error, when it is more than twice the RMSE.

When the NWP-ZTD is used in high-precision positioning, it is important to know when this will lead to large errors in the observations of the NWP-ZTD. The relationship between the large errors of the NWP-ZTD and 6-hour rainfall is discussed.

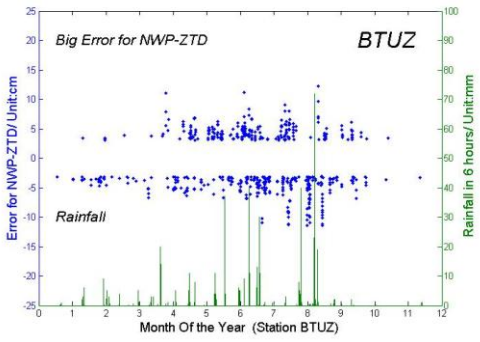

(a)

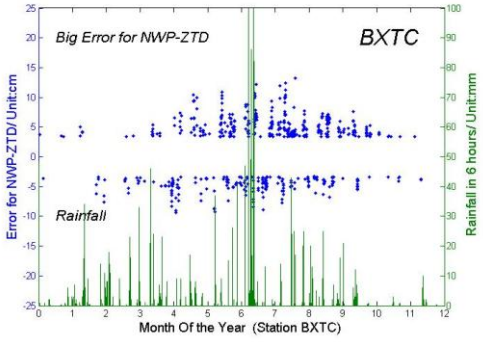

(b)

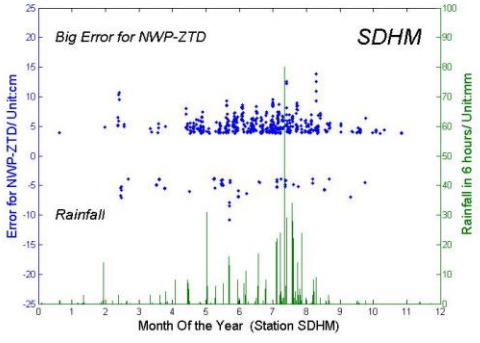

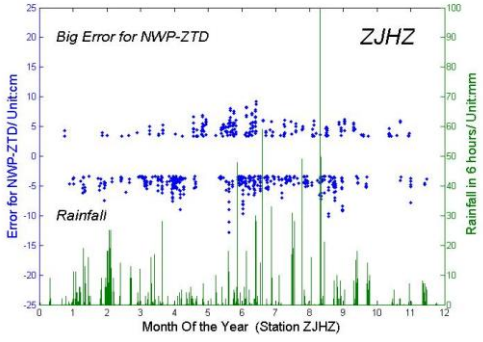

(c) (d)

Figure 5.6: The large error of NWP-ZTD and 6-hour rainfall for 4 stations in 2010

Compared to the whole errors of the NWP-ZTD in Figure 5.4 and 5.5, the large errors of the NWP-ZTD show more correlation with rainfall in Figure 5.6. For stations BTUZ and SDHM in the northern area (see Figure 5.1), there is no rain in the winter and little rain in the spring, and the large errors are also significantly less frequent or absent during this time. For all stations, the large errors occur more during the rainy seasons, while there is also much more rainfall than during other seasons.

It has been mentioned that the errors of the NWP-ZTD are related to the frequency of rain and not related to the amount of rain. To analyze the correlation of the frequency of large NWP-ZTD errors and rainfall, the large NWP-ZTD errors and rainfall are described as 0 and 1.

The water vapor will rise rapidly before rainfall and may last for a while after rainfall. In addition, the GPS-ZTD is estimated in the daily solution, and the tropospheric correction is averaged each hour for the whole day. This will lead to the larger difference between the NWP-ZTD and GPS-ZTD on the rainy days. If there is rain during this hour, the 12 hours before and after this hour will be set to 1, otherwise it is set to 0. If there is a large error, it is set to 1, otherwise it is set to 0.

The statistical method is used for the 4 stations (BTLU, BXTC, SHBS and ZJHZ) that have more observations for the NWP-ZTD with rain (see Table 5.10). The correlations for the frequency of large NWP-ZTD errors and rainfall for the 4 stations during the rainy seasons are given in Table 5.11.

Stations	Correlations	Samples of large errors
BTLU	0.57	145
BXTC	0.50	159
SHBS	0.70	133
ZJHZ	0.71	187

Table 5.11: The correlation for the frequency of NWP-ZTD large errors and rainfall during the rainy seasons

Table 5.11 shows that the large error of the NWP-ZTD is highly related to the rainfall. The correlations of the frequency of large NWP-ZTD errors and rainfall for the 4 stations during the rainy seasons are approximately 0.5 to 0.7. For stations SHBS and ZJHZ, the stations are in a more southern area and closer to the sea. The rainfall in this area is usually initiated by water vapor variation, so the large error of the NWP-ZTD for the 2 stations is more correlated to the rainfall. Station BXTC is located in the mountainous area. The rainfall in this area is not only initiated by water vapor variation but also initiated by the terrain. The large error of the NWP-ZTD for BXTC is shown to be less correlated to the rainfall.

5.2.5 The improvement of the tropospheric model for positioning

In real-time positioning, an atmospheric model, such as the Saastamoinen model, is used directly to eliminate the atmospheric effect. The errors from the atmospheric model are used in the final positioning results. The RMSE of the ZTD integrated from the Radiosonde and NWP model is compared with that from the Saastamoinen model.

Taking the ZTD from the GPS post-processed solution as the reference, the errors of NWP-ZTD, RDS-ZTD and ZTD from the Saastamoinen model

(MDE-ZTD) for 8 stations in 2010 are compared in Table 5.12.

Stations	RMSE (mm)		
	NWP-GPS	RDS- GPS	MDE-GPS
BFYH	15.85	24.09	98.43
BTLU	16.97	19.26	103.72
BTUZ	15.49	17.94	97.16
BXTC	16.62	31.80	100.88
SDHM	19.12	27.62	88.30
SDJM	15.22	19.52	100.62
SHBS	19.78	20.70	102.81
ZJHZ	16.74	23.00	106.08

Table 5.12: Errors of NWP-ZTD, RDS-ZTD and MED-ZTD in 2010

The improvement of the atmospheric correction for real-time positioning is shown in Table 5.12. For the Saastamoinen model, the error of the MDE-ZTD is approximately 100 mm and will be larger at the stations with abundant water vapor and rainfall, such as SHBS and ZIHZ. The error of the NWP-ZTD is less than 20 mm; it is improved by approximately 400%.

5.2.6 Conclusion of precision analysis

To directly remove the tropospheric effects during the GPS data processing, the ray tracing algorithm and the MET data from the NWP model are used to integrate the ZTD. Yearly data from the Radiosonde and GPS observations for 8 stations in East China region are used to discuss the precision of the integrated NWP-ZTD.

The RDS-ZTD from 8 Radiosonde stations are taken as the reference, and both the estimated GPS-ZTD and integrated NWP-ZTD are fit to the RDS-ZTD. The

yearly RMSE of GPS-ZTD is approximately 20-30 mm in 2010 and 2011. The GPS-ZTD shows a 10 mm larger bias during the rainy season, when there is more water vapor in the troposphere and more rainfall than in other seasons. The yearly RMSE of NWP-ZTD is approximately 25-35 mm, which is almost the same level as the GPS-ZTD.

The main purpose of the experiment is to use the NWP-ZTD instead of the GPS-ZTD estimation. Therefore, the GPS-ZTD is taken as the reference, the differences between the NWP-ZTD and GPS-ZTD are taken as the NWP-ZTD errors. The yearly error of the NWP-ZTD is less than 20 mm, and the monthly error shows the seasonal changes. The error for the NWP-ZTD in heavy storms is larger than at any other time, but it is NOT as large as the amount of rainfall. The observations of the NWP-ZTD with and without rain are analyzed separately, and the error of the NWP-ZTD with rain is approximately 20-25 mm, which is approximately 5 mm larger than the yearly error.

For the analysis of reliability and applicability for the NWP-ZTD, the correlation between the NWP-ZTD large errors and rainfall are discussed. When there is no rain in the winter or spring at some stations, the large errors of NWP-ZTD are significantly less or none. The correlations for the frequency of the NWP-ZTD large errors and rainfall for the 4 stations during the rainy seasons are approximately 0.5 to 0.7. The precision of the NWP-ZTD is highly correlated to the frequency of rainfall.

Taking the estimated GPS-ZTD as the reference, the error of NWP-ZTD is compared with the error of RDS-ZTD from the Radiosonde and MED-ZTD from the Saastamoinen model. The NWP-ZTD is shown to be closer to the GPS-ZTD and can be well predicted for the following few hours. Depending on the precision requirement for the GPS positioning, the integrated NWP-ZTD may directly eliminate the tropospheric effects in the data processing that will

improve the ambiguity resolve and the convergence period. However, for the high-precision positioning (millimeter level), the precision of the integrated NWP-ZTD is not good enough, and it needs to be corrected for higher accuracy. The GPS-ZTD derived from a relatively sparse GPS network may be used to correct the integrated NWP-ZTD, and the error model may be established to improve the NWP-ZTD. A related experiment will be completed in the next work.

5.3 The improvement method of NWP-ZTD

Is it possible that the NWP-ZTD can instead be an estimation of the tropospheric parameters in the GPS data processing? It depends on the positioning precision and the precision of the NWP-ZTD. Limited by the accuracy of the MET data predicted from the NWP model, the precision of the integrated NWP-ZTD is not sufficient. Could the integrated ZTD from the NWP model be improved? In the paper, the sparse GPS network will be used to estimate the ZTD, which is called the spatial correction. In addition, the GPS-ZTD from the surrounding GPS stations is used to correct the integrated ZTD from the NWP model. The GPS networks with different horizontal resolutions (150 km and 250 km) are used for the correction. The error information of the NWP-ZTD from the last observation epoch will be used to improve the NWP-ZTD in this epoch, which is the temporal correction. The NWP-ZTD with different temporal resolutions and different precisions are used to check the improvements made by two corrections. The experiment is completed in the East China region and in different seasons. The mean RMSE of the corrected ZTD from the NWP model is smaller than 10 mm in the spring, and approximately 15 mm in the summer. It is suggested that temporal correction be used, as it is a more effective improvement and requires less computing resources.

5.3.1 Experimental design

The tropospheric correction could be integrated from the NWP model (NWP-ZTD), but the precision of the NWP-ZTD is not sufficient for high-precision positioning. The experiment here is aimed at improving the precision of the NWP-ZTD by the different correction algorithms.

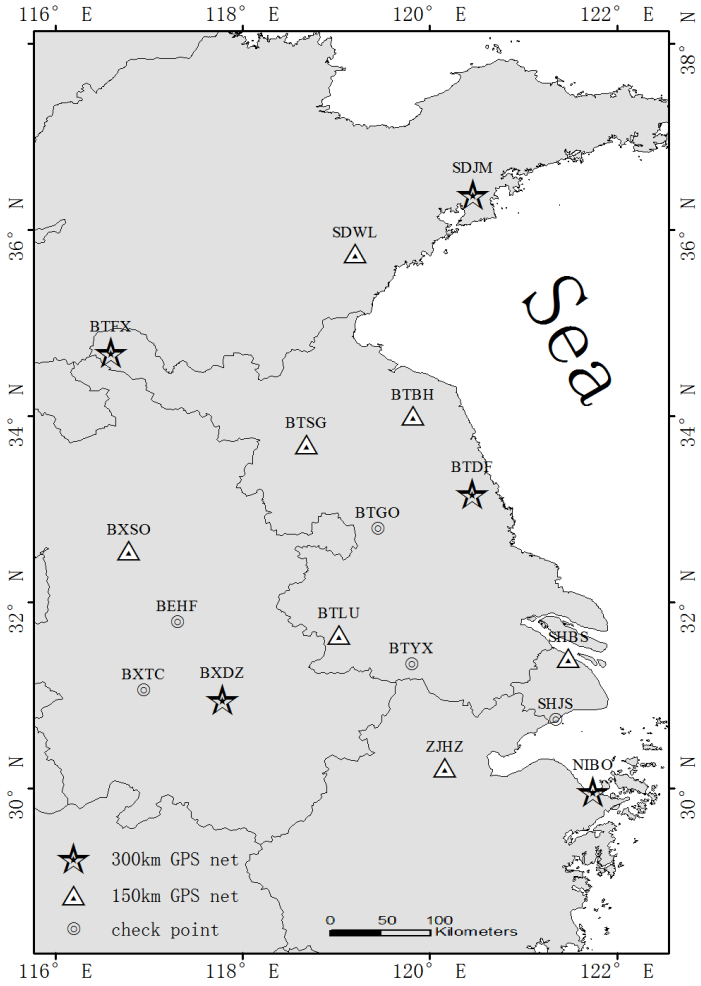

Figure 5.7: The distribution of GPS stations for correction

All 17 GPS stations for corrections are distributed in northeastern China, as shown in Figure 5.7. The 5 stations marked by pentagons make up a regional GPS network with a 250 km resolution; 12 stations marked by pentagons and triangles make up a regional GPS network with a 150 km resolution; and the other 5 GPS stations marked by circle are used to check the improvement in

precision for NWP-ZTD.

- **The MET data from NWP model**

The MET data for different seasons and with different temporal resolutions are selected for the experiment. The details of MET data from the NWP model are as follows:

1) Normal data from days 161 to 224 during the year 2011 with a 3-hour resolution (in summer);
2) Normal data during July in 2011 (from days 162 to 212) with a 1-hour resolution (in summer);
3) Normal data from days 022 to 099 in 2013 with a 3-hour resolution (in spring); and
4) Bad data from days 022 to 099 in 2013 with a 3-hour resolution (in spring).

The NWP model is usually used to predict the MET parameters in the following 72 hours, and in the first few hours, the accuracy is not very good. Therefore, the predicted MET data from hours 12 to 18 is used. This data is updated every 6 hours and is called normal data.

To see if the integrated NWP-ZTD with a worse precision could be corrected well, the MET data predicted after 36 hours is used in 2013 and is called bad MET data.

- **The precision of the uncorrected NWP-ZTD**

The experiment is done in the spring of 2013 and summer of 2011 to check the corrections in different seasons. Taking the GPS-ZTD as the reference, the RMSE of the NWP-ZTD for the 12 correct stations and 5 check stations in

different seasons and different resolution is evaluated.

	Station	2011-1h	2011-3h	2013-3h	2013-3h-w
Reference Stations					
1	SDJM	26.51	24.38	9.54	111.98
2	BTFX	29.76	29.11	21.99	80.68
3	BTDF	30.90	27.48	20.46	131.46
4	BXDZ	28.03	29.90	17.24	83.27
5	NIBO	29.00	28.10	12.62	24.62
6	SDWL	22.52	21.19	10.35	16.19
7	BTSG	25.88	26.06	8.58	52.28
8	BTBH	30.61	29.30	9.83	27.17
9	BXSO	29.69	28.65	14.09	120.24
10	BTLU	30.55	34.52	20.36	27.82
11	SHBS	29.23	29.32	23.33	144.38
12	ZJHZ	21.57	25.36	14.88	70.70
Mean		**27.85**	**27.78**	**15.27**	**74.23**
Check Stations					
1	BTGO	34.22	31.01	10.16	101.54
2	BEHF	36.63	35.56	15.83	24.18
3	BXTC	24.80	25.48	12.32	45.41
4	BTYX	23.35	24.34	15.94	60.81
5	SHJS	22.43	21.56	12.13	79.45
Mean		**28.29**	**27.59**	**13.28**	**62.28**

Table 5.13: The errors of NWP-ZTD from different MET data for all stations (Unit: mm)

2011-1h: The NWP data with a 1-hour resolution from July 2011 is used to integrate the NWP-ZTD for all stations.

2011-3h: The NWP data with a 3-hour resolution from the summer of 2011 is used to integrate the NWP-ZTD for all stations.

2013-3h: The NWP data with a 3-hour resolution from the spring of 2013 is used to integrate the NWP-ZTD for all stations.

2013-3h-w: The NWP data with a 3-hour resolution and worse precision from the spring of 2013 is used to integrate the NWP-ZTD for all stations.

In Table 5.13, the mean of the RMSE for the 12 reference stations and 5 check stations is less than 30 mm in the summer and less than 20 mm in the spring. The NWP-ZTD with a 1-hour resolution does not show a better precision than that with a 3-hour resolution. However, for the NWP-ZTD integrated from the bad data in 2013, the RMSE for all GPS stations is significantly larger. The mean of the RMSE is larger than 70 mm for reference stations and 60 mm for check stations.

5.3.2 Spatial correction for NWP-ZTD

The GPS networks will be used to correct the NWP-ZTD, so the precision of the ZTD derived from the GPS real-time solution will be discussed first.

The water vapor is one of the most active compositions in the atmosphere. It plays an important role in the weather systems. The GPS signals are most refracted by water vapor, which will affect the precision of the GPS positioning. For the tropospheric correction used in GPS positioning, the dry part can be well modeled by the most empirical tropospheric model, while the wet part cannot be well modeled. Therefore, the ZTD is usually estimated together with other parameters in GPS data processing, and the GPS-derived ZTD can be transferred to the precipitable water vapor (PWV). Currently, GPS meteorology (GPS/MET) is a conventional technique for water vapor detection in the meteorological field for its high precision and because it is less affected by weather conditions.

On the one hand, the PWV detected from the regional GPS network can indicate

the spatial and temporal variances of the water vapor in the atmosphere (Ye et al., 2008). The PWV is highly related to the rainfall in the upcoming 3 hours and is widely used for weather now-casting. In the weather analysis, the latest observations should be used while the atmosphere changes quickly. Thereby, the ZTD from the GPS real-time solution is used to obtain the real-time PWV. The precision of the ZTD from the real-time solution is import to the weather analysis, and the error information of the ZTD is necessary while the ZTD is used in the NWP model. On the other hand, the ZTD from the real-time solution will be used to improve the integrated NWP-ZTD in the next experiment in this thesis. The improvement of the NWP-ZTD will be affected by the precision of the real-time ZTD.

As reported by the National Oceanic and Atmospheric Administration (NOAA), the differences between the PWV from GPS real-time solutions and post-processed solutions are approximately 1.2 mm, while there is an 8 mm difference for the ZTD. The main experiment in this chapter evaluates the precision of the GPS-derived ZTD from the real-time solution. The ZTD can be divided into zenith hydrostatic delay (ZHD) and zenith wet delay (ZWD). The ZHD can be well modeled, at better than 1 mm (Businger et al., 1996). Compared with the ZWD from the post-processed solution, the precision of the ZWD from the GPS real-time solution will be analyzed. Then, the ZWD will be transferred to the PWV, and the real-time PWV is compared with the results from the Radiosonde integration.

1) Retrieval of ZWD and PWV

The tropospheric delay of the GPS signal is described as the ZTD and mapping function (MF). The ZTD is divided into ZHD and ZWD, and the ZHD could be well modeled from the atmospheric pressure on the ground as follows (Askne et al., 1987):

$$\mathrm{ZHD} = \frac{0.0022768 P_0}{1 - 0.00266\cos 2\varphi - 0.00028H} \tag{5.3.1}$$

where P_0 is the pressure on the ground (hPa), φ is the latitude of the GPS station, and H is the altitude of the receiver (km).

While the ZTD is obtained from the GPS solution, the ZWD can be obtained from the ZTD minus the ZHD:

$$\mathrm{ZWD} = \mathrm{ZTD} - \mathrm{ZHD} \tag{5.3.2}$$

The PWV is defined as the height of the water vapor column per unit area, and the relationship between PWV and ZWD is defined as follows:

$$\mathrm{PWV} = \mathrm{ZWD} \times \Pi \tag{5.3.3}$$

Π is the ratio of PWV and ZWD, and it is defined as follows:

$$\Pi = 10^6 \left[R_w \left(\frac{k_2}{T_m} \right) + k_1 \right]^{-1} \tag{5.3.4}$$

where R_w is the ideal gas constant, k_1 and k_2 are constant, and T_m is the weighted mean temperature of the atmosphere modeled from the surface temperature T_s by the Radiosonde observations (Bevis et al., 1992):

$$T_m = 70.2 + 0.72 \times T_s \tag{5.3.5}$$

The value of the ratio factor Π is approximately 0.15, and it varies approximately 15% according to the changes in atmospheric parameters (Bevis et al., 1992).

2) Experiment results

The GPS data from over 200 GPS stations in the East China region are processed every half-hour in real-time at the Shanghai Meteorological Bureau (SMB). There are several Radiosonde stations located in the same area, and some GPS stations are very near the Radiosonde station or located in the same meteorological station. The ZTD from the GPS real-time solution for the experiment is obtained from the real-time data processed in SMB.

The software GAMIT from the Massachusetts Institute of Technology (MIT) is used for both real-time and post-processed GPS data. There are two main differences between the real-time and post-processed GPS data: One difference is that the ultra-rapid orbit from the International GPS Service (IGS) is used in the real-time data processing, while the precise orbit from the IGS is used in the post processing; and the other difference is that the GPS data used in post processing is more complete than that used in real-time processing because of the real-time transmission problem.

The 2 Radiosonde stations in the East China region are selected for the experiment, and the nearest 2 GPS stations are also selected. The locations of the stations are listed in Table 5.14.

	Station	Location of GPS	Location of Radiosonde
1	SHBS	[121.48, 31.41]	[121.46, 31.41]
2	ZJHZ	[120.17, 30.23]	[120.17, 30.23]

Table 5.14: The locations of 2 Radiosonde stations and the nearest GPS stations used in the experiment

The precision of the real-time ZTD is evaluated by comparison with the results from the GPS post-processing solution. Only the ZWD derived from the GPS real-time solution will be discussed in the experiment, while the ZHD is usually well modeled. The ZWD is also transferred to the PWV, and the precision of the real-time PWV is also evaluated.

The experiment was completed in 2008 and 2010; the rainfall and typhoons occurred more in 2008 and less in 2010, on average.

a. The distributions of yearly ZWD in 2010

The real-time and post-processing ZTD are estimated from the real-time and post-processed GPS data, respectively. The ZWD is obtained from the real-time and post-processed ZTD by subtracting the ZHD. The distributions of the real-time and post-processed ZWD at stations SHBS and ZJHZ from the post-processed and real-time solutions are shown in Figures 5.8 and 5.9. The x-axis is the day of the year, and the y-axis is the SWD (unit: meter).

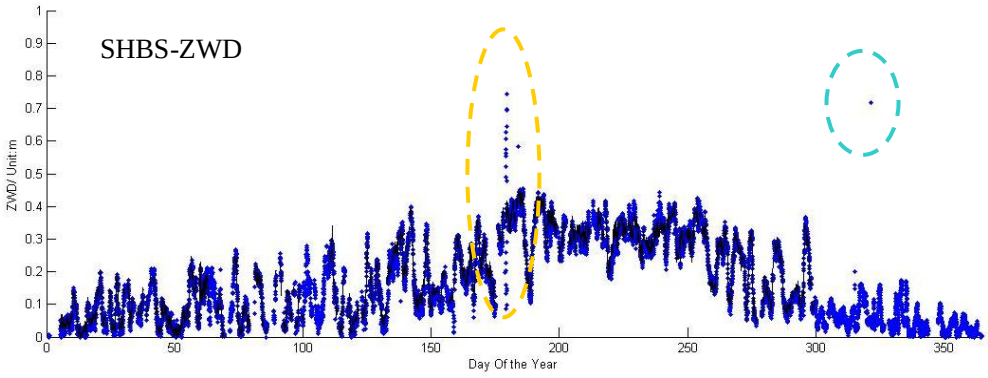

Figure 5.8: The real-time GPS solutions (blue points) compared with the post-processed GPS solutions (black lines) at station SHBS in 2010

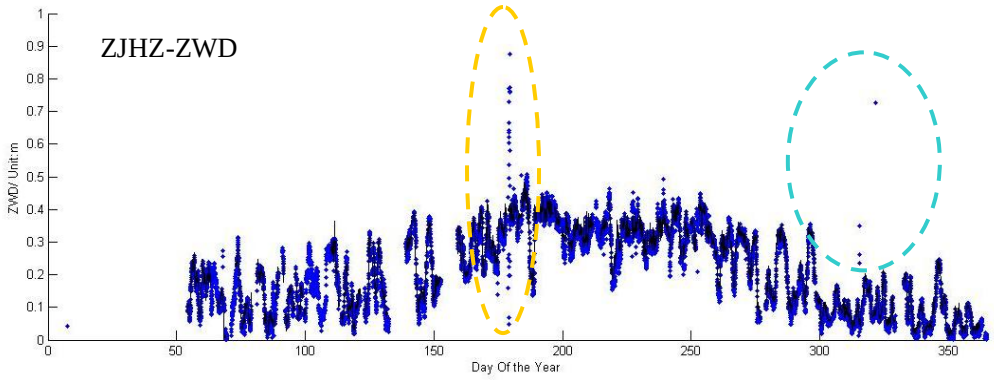

Figure 5.9: The real-time GPS solutions (blue points) compared with post-processed GPS solutions (black lines) at station ZJHZ in 2010

As shown in Figures 5.8 and 5.9, the real-time ZWD is generally fit to the post-processed ZWD. At the end of June, the real-time ZWD has a continual abnormal value at stations SHBS and ZJHZ. This is because of the ultra-rapid orbit used in the GPS real-time data processing. The ultra-rapid orbit from the IGS is predicted for the following 3 days and will have a small error when the GPS satellite malfunctions. The very small error of the orbit can lead to a large error in the ZTD estimation. In addition, the ultra-rapid orbit is updated every 6 hours, so if the orbit has an error, the ZTD will have a continual error for the next 6 hours. This is the main reason for the continual abnormal value of the SWD in Figures 5.8 and 5.9. If the GPS stations are not far away from each other, the GPS signals from the same satellites will be received for the GPS stations. Therefore, if one of the received satellites malfunctions, the ZWD will have an abnormal value at the same time for multiple nearby GPS stations.

There are some scattered points in Figures 5.8 and 5.9, and these are the occasional abnormal values of the real-time ZWD. The interruption of the real-time GPS data transmission is the main reason. While the data resumed transmission after interruption for over 3 hours, there were not enough observations for cycle slip detection and estimation of other unknown

parameters. Therefore, there is a ZWD with an abnormal value in the real-time data processing.

b. The precision of the PWV in 2008 and 2010

Based on Eq. (5.3.3), the ZWD will be transferred to the PWV for 2008 and 2010 at station SHBS. The Radiosonde data is used to integrate the ZWD, and the ZWD is also transferred to the PWV. The differences between the PWV from the GPS real-time solution (GPS-PWV) and the Radiosonde integration are taken as the errors of the real-time GPS-PWV. The GPS-PWV with a large error, which is more than twice the RMSE, will be removed. This means that the orbit error and data interruption will affect the precision of the GPS-PWV much less.

The monthly and yearly standard error of the real-time GPS-PWV in 2008 and 2010 are shown in Tables 5.15 and 5.16.

Month	1	2	3	4	5	6	7	8	9	10	11	12	total
error	1.3	2.5	1.1	2.3	2.7	5.1	6.0	4.7	4.3	2.7	1.8	1.1	3.1

Table 5.15: The monthly and yearly error of the real-time GPS-PWV in 2008 at station SHBS (unit: mm)

Month	1	2	3	4	5	6	7	8	9	10	11	12	total
error	1.3	1.5	1.7	2.0	2.9	3.7	5.9	5.5	4.3	1.9	1.4	1.2	2.9

Table 5.16: The monthly and yearly error of the real-time GPS-PWV in 2010 at station SHBS (unit: mm)

It is shown in Tables 5.15 and 5.16 that the yearly RMSE of the real-time GPS-PWV is approximately 3 mm. The yearly RMSE of the GPS-PWV is 3.1 mm in 2008 and 2.9 mm in 2010. There is more rainfall and more typhoons in 2008. Thereby, the water vapor in the atmosphere in 2008 is greater, and the

yearly RMSE of the GPS-PWV is slightly larger in 2008. In the rainy season (from June to September), the monthly RMSE is greater than in other seasons.

Based on the analysis of the ZWD from the real-time and post-processed GPS solutions, the real-time ZWD is generally fit to the post-processed results. The main factors that lead to the abnormal value of ZTD are orbit error and data interruption. The ZTD from the real-time solution will have a similar precision to the ZWD, while the ZHD is well modeled.

In another experiment, the ZTD is estimated from the GPS network in real-time, and the real-time ZTD will be used to improve the ZTD from the NWP integration. It is better to obtain the orbit with a more stable precision from an IGS data center. Meanwhile, when the data are interrupted at one GPS station, it is better to use the data from other nearby stations.

The precision of the PWV from a real-time GPS solution is evaluated by comparison with the results from the Radiosonde integration. This is the indication for the precision of the real-time ZTD from the GPS solution. Additionally, the precision of the PWV is given as a reference when it is used for weather now-casting analysis. When the PWV and ZWD are used in the NWP model to improve the weather forecast, error analysis of the PWV and ZWD are necessary.

- **The correlations of GPS-ZTD from different GPS networks**

To check the correlations of the ZTD within different distances, GPS networks with different resolutions (50 km, 150 km and 250 km) are used to estimate the GPS-ZTD. The distribution of GPS networks with different resolutions are shown in Figure 5.10.

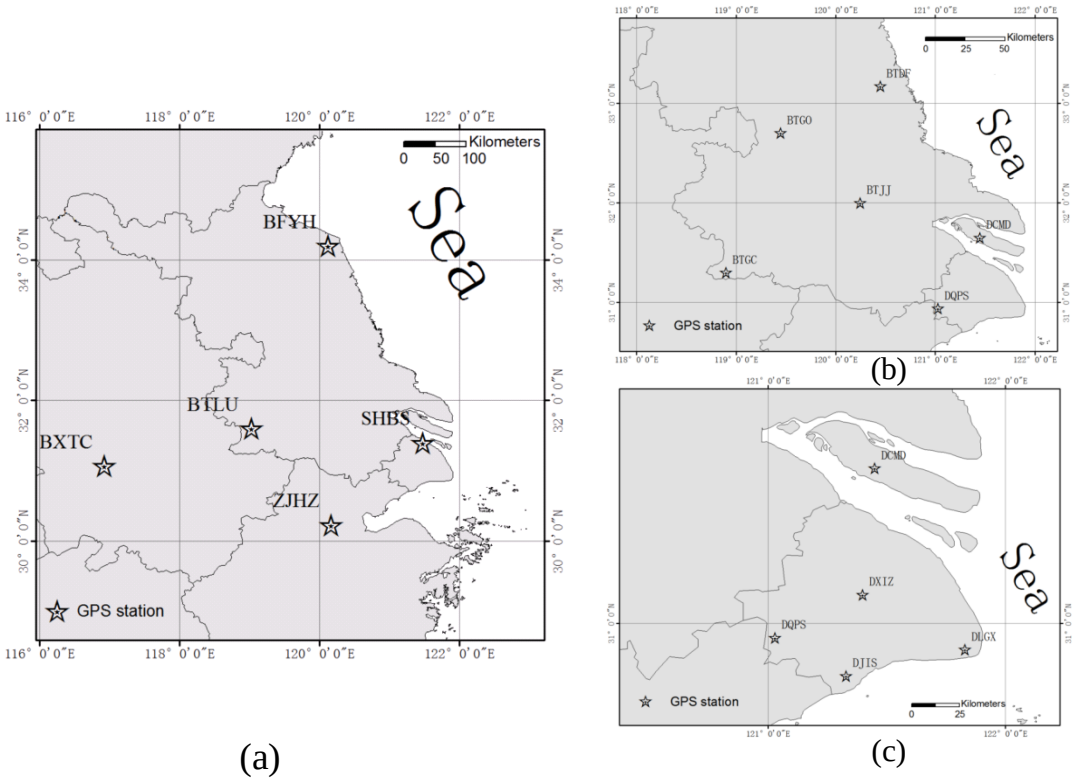

Figure 5.10: The GPS network with approximately 250 km (a), 150 km (b) and 50 km (c) resolution in the East China region

In Figure 5.10a, station BTLU is in the center of the network; the correlations of GPS-ZTD between BTLU and the other 4 stations in 2010 are shown in Table 5.17a. Similarly, the correlations of the GPS-ZTD between BTJJ and the other 5 stations in Figure 5.10b in 2010 are shown in Table 5.17b. The correlations of GPS-ZTD between DXIZ and the other 4 stations in Figure 5.10c in 2010 are shown in Table 5.17c.

Station	Correlation	Distance of GPS stations
BTLU-BYFH	0.56	287 km
BTLU-BXTC	0.68	239 km
BTLU-SHBS	0.61	270 km
BTLU-ZJHZ	0.59	200 km

(a) 250 km resolution

Station	Correlation	Distance of GPS stations
BTJJ-BTDF	0.63	124 km
BTJJ-BTGC	0.70	122 km
BTJJ-BTGO	0.68	156 km
BTJJ-DCMD	0.59	174 km
BTJJ-DQPS	0.67	155 km

(b) 150 km resolution

Station	Correlation	Distance of GPS stations
DXIZ-DCMD	0.71	67 km
DXIZ-DLGX	0.81	54 km
DXIZ-DJIS	0.80	54 km
DXIZ-DQPS	0.84	56 km

(c) 50 km resolution

Table 5.17: The correlations of GPS-ZTD for the stations with different resolutions in 2010

It is shown in Table 5.17 that the correlation of the GPS-ZTD is over 0.8 when the distance of the stations is approximately 50 km; the correlation of the GPS-ZTD is near 0.7 when the distance of the stations is approximately 150 km; and the correlation of the GPS-ZTD is approximately 0.6 when the distance of the stations is approximately 250 km. The latitude of the stations has a greater influence on the correlations than distance per se. For example, stations BTLU and ZJHZ are the nearest to each other in the network with 250 km resolution, but their correlation is not the highest. The same characteristic is shown for station BTJJ-BTDF and station DXIZ-DJIS. The main reason is that the weather system is always moving in the north-south direction.

A correlation of the GPS-ZTD of over 0.6 is generally considered highly related. Therefore, the GPS network with a 250 km resolution is recommended for use in the experiment. The correlation of the GPS-ZTD between BTLU and the other 4

stations for each month in 2010 are shown in Table 5.18.

	Correlation of GPS-ZTD			
	BTLU-BFYH	BTLU-BXTC	BTLU-SHBS	BTLU-ZJHZ
Jan.	0.63	0.82	0.80	0.60
Feb.	0.65	0.67	0.71	0.72
Mar.	0.72	0.79	0.68	0.65
Apr.	0.64	0.72	0.65	0.62
May	0.61	0.57	0.62	0.66
Jun.	0.35	0.60	0.60	0.35
Jul.	0.14	0.44	0.44	0.25
Aug.	0.45	0.16	0.21	0.27
Sep.	0.38	0.58	0.29	0.43
Oct.	0.66	0.73	0.65	0.50
Nov.	0.42	0.64	0.45	0.48
Dec.	0.60	0.82	0.65	0.66
mean	0.52	0.63	0.56	0.51

Table 5.18: The correlation of GPS-ZTD for the stations with approximately 250 km for each month in 2010

It is shown in Table 5.18 that the correlation of the GPS-ZTD is much smaller during the rainy season (from June to September) than in other seasons. Water vapor is abundant in the atmosphere, and many rain storms occur during the rainy season. The weather systems move quickly during that time, which leads to the large differences in the GPS-ZTD in different areas in a short time, even for the GPS stations that are close to each other.

- **The precision of the spatially corrected NWP-ZTD in summer**

Based on the former analysis, the GPS network with a 250 km resolution may be

sufficient for the NWP-ZTD correction. For the experiment, the GPS networks with 250 km and 150 km resolutions are both used here, which is a spatial correction for the NWP-ZTD.

The GPS networks are used to improve the precision of the NWP-ZTD for the 5 check stations in different seasons. For each check station, the nearest 3 referenced stations from the network will be used. The error information of the NWP-ZTD for the referenced stations is interpolated to the locations of the check stations as the correction information. The NWP-ZTD for the 5 check stations is improved by the added corrections.

The NWP-ZTD is integrated from the MET data with 1-hour and 3-hour temporal resolutions in the summer in 2011. The observations of the NWP-ZTD with a 1-hour temporal resolution are for all of July (from day 182 to day 212); the NWP-ZTD has a lower temporal resolution of 3-hour or less samples, so the observations of NWP-ZTD are over a longer timeframe (from day 161 to day 224). Taking the GPS-ZTD from the GPS post-processed solution as the reference, the uncorrected and corrected results are shown in Tables 5.19 and 5.20.

Station	Un-corrected	Number of Samples	150 km net corrected	Improve-ment	300 km net corrected	Improve-ment
BTGO	34.22	1369	20.77	39.30%	23.66	30.86%
BEHF	36.63	1369	20.70	43.49%	25.23	31.12%
BXTC	24.80	1369	17.32	30.16%	18.95	23.59%
BTYX	23.35	1369	14.39	38.37%	14.75	36.83%
SHJS	22.43	1369	13.42	40.17%	15.03	32.99%
mean	**28.29**	**1369**	**17.32**	**38.30%**	**19.52**	**31.08%**

Table 5.19: The RMSE of the uncorrected and spatially corrected NWP-ZTD with a 1-hour

resolution for 5 check stations, from day 182 to day 212 in 2011 (Unit: mm)

Station	Un-corrected	Number of Samples	150 km net corrected	Improve-ment	300 km net corrected	Improve-ment
BTGO	31.01	951	17.07	44.95%	21.91	29.35%
BEHF	35.56	951	21.21	40.35%	24.48	31.16%
BXTC	25.48	951	16.68	34.54%	18.93	25.71%
BTYX	24.34	951	16.16	33.61%	16.68	31.47%
SHJS	21.56	908	12.78	40.72%	14.55	32.51%
mean	**27.59**	**942**	**16.78**	**38.84%**	**19.31**	**30.04%**

Table 5.20: The RMSE of uncorrected and spatially corrected NWP-ZTD with a 3-hour resolution for 5 check stations, from day 161 to day 224 in 2011 (Unit: mm)

Uncorrected: The NWP-ZTD for check stations without correction by the GPS network

150 km net corrected: The NWP-ZTD for check stations corrected by the GPS network with 150 km resolution

250 km net corrected: The NWP-ZTD for check stations corrected by the GPS network with 250 km resolution

In Tables 5.19 and 5.20, the RMSE of the NWP-ZTD in the summer of 2011is approximately 30 mm before correction. The errors are reduced to 20 mm when corrected by the GPS network with 250 km resolution and less than 17 mm when corrected by the GPS network with 150 km resolution. Compared to the uncorrected NWP-ZTD, the precision of the NWP-ZTD is improved by approximately 30% by the GPS network with 250 km resolution and approximately 40% by the GPS network with 150 km resolution.

Compared with Tables 5.19 and 5.20, the NWP-ZTD with a 1-hour resolution does not show significant improvement over that with a 3-hour resolution. The main reason may be that the atmosphere does not change very much over 3 hours most of the time. Therefore, the MET data from the NWP model with a

3-hour resolution is sufficient to integrate with the NWP-ZTD.

The NWP-ZTD corrected by the 150 km-network is improved more than that corrected by the 250 km-network, but the mean RMSE is only 2 mm better. Economically, the GPS network with a 250 km resolution could be used in the real case.

- **The precision of the spatially corrected NWP-ZTD in the spring**

The same experiment was performed for the NWP-ZTD in the spring of 2013. The water vapor in the atmosphere in spring is less than that in summer, and the precision of the NWP-ZTD is better in the dry season, as discussed in the former experiment.

The NWP-ZTD is integrated from the normal MET data and bad MET data (see Sec.3.2) and corrected by the 150 km-network and 250 km-network, and the results are shown in Tables 5.21 and 5.22.

Station	Un-corrected	Number of Samples	150 km net corrected	Improve-ment	300 km net corrected	Improve-ment
BTGO	10.16	1232	5.67	44.19%	6.82	32.87%
BEHF	15.83	1217	7.93	49.91%	7.05	55.46%
BXTC	12.32	819	8.28	32.79%	9.32	24.35%
BTYX	15.94	1232	15.72	1.38%	13.00	18.44%
SHJS	12.13	1154	9.10	24.98%	8.50	29.93%
mean	**13.28**	**1130**	**9.34**	**30.65%**	**8.94**	**32.21%**

Table 5.21: The RMSE of uncorrected and spatially corrected NWP-ZTD from normal MET data with a 3-hour resolution for 5 check stations, from day 022 to day 099 in 2013 (Unit: mm)

In Table 5.21, the precision of the NWP-ZTD is better than that in Tables 5.19 and 5.20, and the mean RMSE is less than 14 mm before correction in the spring of 2013. The errors are reduced to approximately 10 mm when corrected by the GPS network with 250 km and 150 km resolutions. The precision of the NWP-ZTD is improved by an average of approximately 30% by the referenced GPS network.

The NWP-ZTD itself has a good precision in the dry season, so the improvement of the NWP-ZTD by the referenced GPS network is small. The NWP-ZTD improved by the 150 km-network shows a small difference with that improved by the 300 km-network. Similar to the results in the summer, the GPS network with a 300 km resolution is sufficient to improve the NWP-ZTD in the spring.

To determine whether the NWP-ZTD with a worse precision could be improved further, the bad MET data from the NWP model is used to integrate the NWP-ZTD in Table 5.19. Taking the GPS-ZTD from the GPS post-processed solution as the reference, the uncorrected and corrected results are shown in the Table 5.22.

Station	Un-corrected	Number of Samples	150 km net corrected	Improve-ment	300 km net corrected	Improve-ment
BTGO	101.54	1232	48.93	51.81%	64.92	36.06%
BEHF	24.18	1217	12.18	49.63%	22.77	5.83%
BXTC	45.41	819	37.42	17.60%	44.72	1.52%
BTYX	60.81	1232	55.35	8.98%	60.27	0.89%
SHJS	79.45	1154	68.29	14.05%	79.28	0.21%
mean	**62.28**	**1130**	**44.43**	**28.66%**	**54.39**	**8.90%**

Table 5.22: The RMSE of the uncorrected and spatially corrected NWP-ZTD from the bad

MET data with a 3-hour resolution for the 5 check stations, from day 022 to day 099 in 2013

(Unit: mm)

The precision of the uncorrected NWP-ZTD is much worse than that in Table 5.21, and the mean RMSE is more than 60 mm before correction. The errors could not be reduced to 20 mm when corrected by the GPS networks with the 250 km and 150 km resolutions. Thus, if the precision of the NWP-ZTD is very bad, it cannot be improved much more by the spatial correction; the precision of the MET data is vital.

5.3.3 Temporal correction for NWP-ZTD

In the former research, the large error of the NWP-ZTD is highly related to the rainfall. The rainfall leads to the changes of the water vapor in the atmosphere. The water vapor usually changes randomly when the weather system is moving. However, the changes in water vapor are continuous over time, meaning the errors of the NWP-ZTD exhibit continuous changes. Therefore, the errors of the NWP-ZTD from the last observation epoch can be used to improve the NWP-ZTD in this epoch.

In the summer, there are many rainstorms, and the weather systems move quickly. It is better to use the NWP-ZTD with high temporal resolution in the summer. The observations of the NWP-ZTD with 1-hour and 3-hour resolutions are used for the experiment in the summer. In the spring, the NWP-ZTD with a 3-hour resolution is used. Additionally, the observations of the NWP-ZTD that are integrated from good and bad MET data are both used to check the improvement.

To compare the spatial correction improvements, the same GPS check stations and the data of the NWP-ZTD at the same times are used for the temporal

correction experiment.

- **The precision of the temporally corrected NWP-ZTD in summer**

As with the spatial correction, the NWP-ZTD is integrated from NWP model with 1-hour and 3-hour temporal resolutions in the summer of 2011. The observations of the NWP-ZTD with 1-hour resolutions are for all of July (from day 182 to day 212), and the observations of the NWP-ZTD are over a longer time (from day 161 to day 224). Taking the GPS-ZTD as the reference, the uncorrected and corrected results are shown in Tables 5.23 and 5.24.

Station	uncorrected	Number of Sample	1-hour Corrected (mm)	Improvement
BTGO	34.22	1369	15.86	53.65%
BEHF	36.63	1369	15.13	58.69%
BXTC	24.80	1369	16.10	35.08%
BTYX	23.35	1369	15.56	33.36%
SHJS	22.43	1369	13.21	41.11%
mean	**28.29**	**1369**	**15.17**	**44.38%**

Table 5.23: The RMSE of the uncorrected and temporally corrected NWP-ZTD with a 1-hour resolution for the 5 check stations, from day 182 to day 212 in 2011 (Unit: mm)

Station	Uncorrected (mm)	Number of Samples	3-hour Corrected (mm)	Improvement
BTGO	31.01	951	27.20	12.29%
BEHF	35.56	951	25.34	28.74%
BXTC	25.48	951	25.16	1.26%
BTYX	24.34	951	24.12	0.90%
SHJS	21.56	908	21.02	2.50%

mean	**27.59**	**942**	**24.57**	**9.14%**

Table 5.24: The RMSE of uncorrected and temporally corrected NWP-ZTD with a 3-hour resolution for the 5 check stations, from day 161 to day 224 in 2011 (Unit: mm)

Uncorrected: The NWP-ZTD for check stations without correction

1-hour corrected: The NWP-ZTD corrected by the error of the NWP-ZTD from 1 hour before

3-hour corrected: The NWP-ZTD corrected by the error of the NWP-ZTD from 3 hours before

The uncorrected NWP-ZTD with 1-hour and 3-hour resolutions have a similar precision, approximately 28 mm, in Tables 5.23 and 5.24. The error of the NWP-ZTD with a 1-hour resolution can be reduced to approximately 15 mm, and the error of the NWP-ZTD with a 3-hour resolution can be reduced to approximately 25 mm. For the NWP-ZTD with a 1-hour resolution, the latest corrected information for NWP-ZTD is from 1 hour before. The corrected information with a high temporal resolution is better for the NWP-ZTD in the summer, while the weather system moves rapidly and water vapor changes quickly during this season.

- **The precision of the temporally corrected NWP-ZTD in the spring**

There is much less water vapor in the atmosphere in the spring than in the summer. The PWV is usually less than 10 mm in the early spring and more than 60 mm in the summer in the East China region. This means that the ZTD in the early spring is approximately 330 mm less than that in the summer. The ZTD integrated from the NWP model with a 3-hour resolution is used for the temporal correction experiment in the spring.

As with the spatial correction, the NWP-ZTD will be integrated from normal and bad MET data in the spring of 2013. The observations of the NWP-ZTD

with a 3-hour resolution are from day 022 to day 099, and they will be corrected by the error information of the NWP-ZTD from 3 hours before. Taking the GPS-ZTD as the reference, the uncorrected and corrected results are shown in Tables 5.25 and 5.26.

Station	Uncorrected (mm)	Number of Samples	3-hour Corrected (mm)	Improvement
BTGO	10.16	1232	9.25	8.95%
BEHF	15.83	1217	10.63	32.85%
BXTC	12.32	819	10.61	13.88%
BTYX	15.94	1232	11.98	24.84%
SHJS	12.13	1154	11.81	2.64%
mean	**13.28**	**1130**	**10.86**	**16.63%**

Table 5.25: The RMSE of uncorrected and temporally corrected NWP-ZTD from normal MET data with a 3-hour resolution for the 5 check stations, from day 022 to day 099 in 2013 (Unit: mm)

Station	Uncorrected (mm)	Number of Samples	3-hour Corrected (mm)	Improvement
BTGO	101.54	1232	17.16	83.10%
BEHF	24.18	1217	13.91	42.47%
BXTC	45.41	819	15.04	66.88%
BTYX	60.81	1232	16.26	73.26%
SHJS	79.45	1154	14.24	82.08%
mean	**62.28**	**1130**	**15.32**	**69.56%**

Table 5.26: The RMSE of uncorrected and temporal corrected NWP-ZTD from bad MET date with a 3-hour resolution for the 5 check stations, from day 022 to day 099 in 2013 (Unit: mm)

The precision of the uncorrected NWP-ZTD from the normal MET data is approximately 10-15 mm; the precision of the uncorrected NWP-ZTD from the bad MET data is worse, on average, than 60 mm in Tables 5.25 and 5.26. The RMSE of the NWP-ZTD with good precision can be reduced to approximately 10 mm by the corrected information; the RMSE of the NWP-ZTD with bad precision can be reduced to approximately 15 mm by the corrected information. The NWP-ZTD from the bad MET data is improved much more by the temporal correction than by the spatial correction. The precision of the MET data used for the integration is less affected by the precision of integrated NWP-ZTD, while the NWP-ZTD is improved by the temporal correction.

- **The precision of the temporally corrected NWP-ZTD in 2010**

Compare the precision and algorithm of spatially corrected and temporally corrected NWP-ZTD, the temporal correction is a better and more convenient way to improve the NWP-ZTD. The method of temporal correction is used for the NWP-ZTD with a 3-hour resolution in 2010 for 8 GPS stations. The GPS-ZTD derived from the GPS post-processed solution are the reference, and the precision of the uncorrected and temporally corrected NWP-ZTD with a 3-hour resolution is listed in Table 5.27.

Station	Uncorrected (mm)	Number of Samples	3-hour Corrected (mm)	Improvement
BFYH	15.85	5080	13.94	12.05%
BTLU	16.97	5023	14.32	15.61%
BTUZ	15.49	5101	12.68	18.14%
BXTC	16.62	5288	13.88	16.49%
SDHM	19.12	5239	11.98	37.34%
SDJM	15.22	5608	12.25	19.51%

SHBS	19.78	4923	16.87	14.71%
ZJHZ	16.74	5366	14.42	13.85%
mean	**16.97**	**5203**	**13.79**	**18.46%**

Table 5.27: The RMSE of uncorrected and temporal corrected NWP-ZTD from bad MET data with a 3-hour resolution for the 5 check stations in 2010 (Unit: mm)

For all 8 GPS stations in the East China region, the average precision of the uncorrected NWP-ZTD in 2010 is approximately 17 mm, shown in Table 5.27. The RMSE of the NWP-ZTD is reduced to approximately 14 mm, when improved by the temporal correction.

5.3.4 Data Assimilation for NWP-ZTD improvement

- **The cost function for data assimilation**

In the assimilation approach, the best estimate x of the tropospheric effect (ZTD), given the observations, is found by the cost function $J(x)$, where

$$J(x) = \frac{1}{2}(x - x_b)^T B^{-1}(x - x_b) + \frac{1}{2}(x - H\{M; G\})^T (O)^{-1}(x - H\{M; G\}) + J_c(x) \quad (5.3.6)$$

where x_b is the ZTD measurement from NWP model (NWP-ZTD), the algorithm for NWP-ZTD is introduced in Chapter 4; B is the error covariance matrix of a priori x_b, it will decided by the error statistics of NWP-ZTD in this Chapter; $H\{M; G\}$ is the observation operator, and its error covariance is given by the matrix O. $J_c(x)$ is for the constraint, which is not taken account here.

$H\{M; G\}$ contains two different observations. One is the ZTD from GPS post-processed solutions (GPS-ZTD), which can be estimated directly from the data processing. Another is the ZTD from the ground meteorological observatory (MET-ZTD), which is estimated by an empirical model, the details of which are as follows.

- **The empirical model for MET-ZTD**

The ground wet pressure e_g, ground temperature T_g and ground pressure P_g are observed by each artificial meteorological observatory in China, and they are also observed by an advanced automatic meteorological station. The resolution of the wet pressure observation is approximately 30-50 km in East China and less than 20 km in Shanghai.

The water vapor is mostly distributed at the bottom of the atmosphere, and the Precipitable Water Vapor (PWV) is mainly near the ground. The vertical distribution of the water vapor is stable in the same area, and it can be modeled from the climate data. The PWV is highly related to the ground wet pressure e_g, and the correlation is more than 0.93 in East China and 0.97 in West China (Yang et al., 2002). The relationship between them can be described as follows:

$$W = a_0 + a_1 e_g + a_2 e_g^2 \tag{5.3.7}$$

where W is the PWV (unit: cm); and a_0, a_1 and a_2 are the empirical factors. The water vapor distribution in the Tibetan Plateau is different from that in other places in China because of the high altitude. In other places, the empirical factors can be described with functions of geographic latitude φ (unit: degree) and altitude H (unit: km). These are defined as follows:

$$a_0 = \begin{cases} 0.03\exp(-1.39H^2 + 2.74H + 0.15), \text{when } \varphi \geq 33^\circ \\ 0.004\exp(0.6H) - d_1 + d_2, \text{when } \varphi < 33^\circ \end{cases} \tag{5.3.8}$$

$$a_1 = \begin{cases} 0.17 + d_3, \text{when } \varphi \geq 33^\circ \\ (0.20 - d_3)d_4, \text{when } \varphi < 33^\circ \end{cases} \tag{5.3.9}$$

$$a_2 = \begin{cases} 0, \text{ when } \varphi \geq 28^{\circ} \\ -0.002, \text{ when } \varphi < 28^{\circ} \end{cases} \tag{5.10}$$

where

$$d_1 = \frac{0.05}{(\varphi - 25.0)^2 + 0.25}$$

$$d_2 = \begin{cases} 0, \text{ when } \varphi > 20^{\circ} \\ -0.9, \text{ when } \varphi \leq 20^{\circ} \end{cases}$$

$$d_3 = \frac{0.066}{(\varphi - 33.0)^2 + 4.41}$$

$$d_4 = \begin{cases} 1.0, \text{ when } a_2 = 0 \\ 1.3, \text{ when } a_2 \neq 0 \end{cases}$$

When the PWV is obtained from the ground wet pressure, the wet delay (ZWD) can be calculated (see Eq. 5.3.2). The hydrostatic delay (ZHD) is can also be obtained from ground parameters (see Eq. 5.3.1). Then, the total delay of the ZTD is obtained as follows:

$$\text{ZTD} = \text{ZHD} + \text{ZWD} \tag{5.11}$$

- **Data assimilation workflow and results**

The MET-ZTD can be modeled from the ground wet pressure, but the empirical model will lead to a relatively large error, approximately 40 mm of ZTD in Shanghai (Yang et al., 2002). In Eq. (5.3.7), the empirical factor a_2 is near 0 in East China; a_0 changes quickly depending on the location, and it is given by Eq. (5.3.8). For better precision of the MET-ZTD, empirical factor a_1 is set as the unknown parameter in the cost function $J(x)$. The prior value of a_1 is obtained from the model in Eq. (5.3.9), and it will be determined by the minimum cost function $J(x)$. When the empirical factor a_1 is obtained, the best estimated x for the improved NWP-ZTD can be obtained from Eq. (5.3.6) directly.

The work flow of the data assimilation is given as follows:

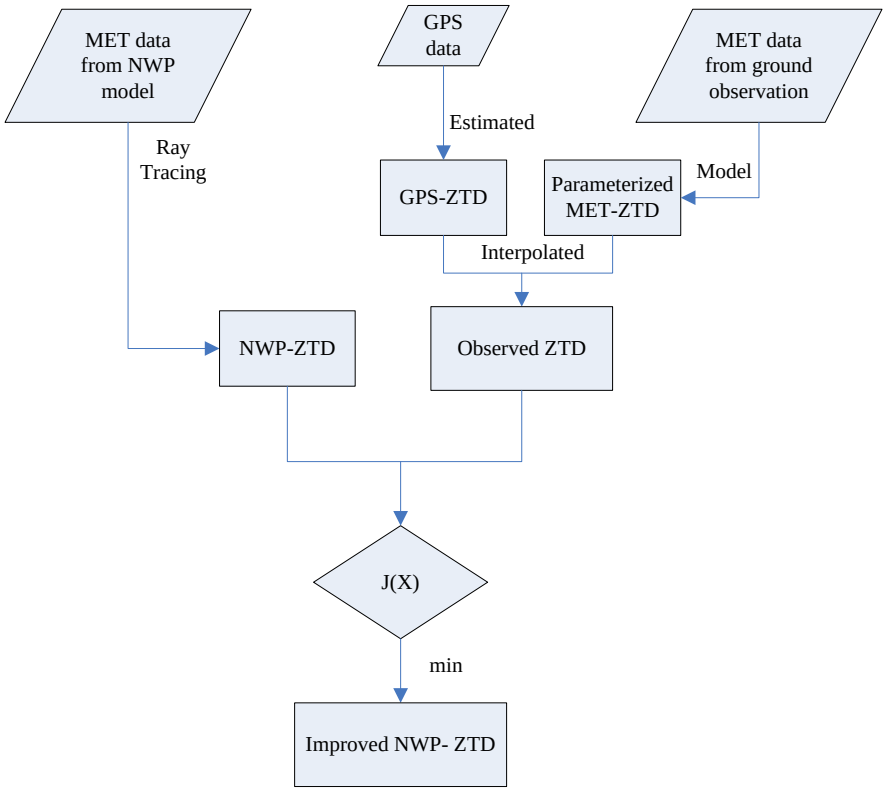

Figure 5.11: The data assimilation workflow

The data from 8 GPS stations in East China (See Figure 5.1) are used for the experiment. The ground meteorological observatories with wet pressure observation in East China are also used for assimilation. The experiment was completed for July 2010, and the improved NWP-ZTD is compared with the GPS-ZTD. The RMSE of the improved NWP-ZTD is given in Table 5.28.

Station	Uncorrected (mm)	Number of Samples	Assimilation Corrected (mm)	Improvement
BFYH	38.92	496	14.21	63.48%
BTLU	29.59	496	12.15	58.93%
BTUZ	29.19	496	12.75	56.32%

BXTC	31.52	496	12.30	60.98%
SDHM	32.28	496	10.52	67.41%
SDJM	29.06	496	12.46	57.12%
SHBS	37.48	496	12.66	66.22%
ZJHZ	30.37	496	12.88	57.57%
mean	**32.30**	**496**	**12.49**	**60.94%**

Table 5.28: The RMSE of uncorrected and assimilation-corrected NWP-ZTD for 8 stations in July 2010 (Unit: mm)

The experiment was completed during the rainy season because of the abundant water vapor, and the errors of the NWP-ZTD are large for all 8 stations, approximately 30-40 mm. When the data assimilation is used for correction, the RMSE of the improved NWP-ZTD is reduced to approximately 12 mm.

5.3.5 Conclusion of improvement for NWP-ZTD

For real-time high-precision positioning, the integrated NWP-ZTD could be used to eliminate the tropospheric effect directly. The integrated NWP-ZTD is used instead of the GPS-ZTD estimation in positioning. Therefore, the difference between the NWP-ZTD and GPS-ZTD will affect the positioning precision. Taking the GPS-ZTD as the reference, the difference between the NWP-ZTD and GPS-ZTD is taken as the precision of the NWP-ZTD.

The predicted MET data from the high-resolution regional NWP model is used to integrate the NWP-ZTD. The accuracy of the predicted MET data is vital for the precision of the integration. Usually, the RMSE of the integrated NWP-ZTD is smaller than 30 mm in the summer (rainy season) and smaller than 20 mm in the spring (dry season). However, the precision of the NWP-ZTD is not sufficient, especially in the summer. Additionally, the RMSE of the NWP-ZTD is large, while the MET data from the NWP model is not predicted well. The

effective correction for the NWP-ZTD is necessary.

The spatial correction by GPS network is used to improve the precision of the NWP-ZTD. The precision of the NWP-ZTD corrected by the GPS network with a 250 km resolution are approximately 20 mm in the summer and 10 mm in the spring. While the GPS network with a higher resolution (150 km) is used for NWP-ZTD, the precision of the corrected NWP-ZTD is improved a little more. However, for the NWP-ZTD integrated from bad MET data, it cannot be improved well by spatial correction, and the RMSE of the NWP-ZTD is over 40 mm in the spring after correction.

The temporal correction uses the error information from the last observation epoch to improve the NWP-ZTD in this epoch. The MET data with 1-hour and 3-hour resolutions are used for the integrated NWP-ZTD. The precision of the temporally corrected NWP-ZTD with a 3-hour resolution are approximately 25 mm in the summer and 10 mm in the spring, while the precision of the NWP-ZTD with 1-hour is 20 mm after temporal correction. The NWP-ZTD with a higher temporal resolution means the error information is updated faster, and it is suggested to use this approach during the rainy season. The NWP-ZTD integrated from the NWP model with a high temporal resolution is better to use during the rainy season. For the NWP-ZTD integrated from bad MET data, it can be improved well by temporal correction, and the RMSE of the NWP-ZTD is approximately 15 mm in the spring after correction. The temporal correction can make the precision of the NWP-ZTD less related with the accuracy of the predicted MET data.

The temporal correction is suggested because of its simple algorithm. However, in the real case, if the GPS receiver is nearby, we can use the differential observation to eliminate the tropospheric effect, and therefore the NWP-ZTD is unnecessary. Economically, the assimilation with ground MET data can be used

to improve the NWP-ZTD. Compared with the spatial correction, it is more efficient and less GPS data will be used.

The higher the temporal MET data used for the NWP-ZTD, the better the precision of the spatially corrected NWP-ZTD. Limited by the time-consuming and computing resources, the temporal resolution of MET data from most regional NWP models is 3 hours. When the water vapor is abundant and changes quickly during the rainy season, the errors of the NWP-ZTD are large. The ground MET data with a high temporal resolution (less than 1 hour) will be effective, and the data assimilation will be useful.

For most weather prediction centers, including the Shanghai NWP innovation center in SMB, a higher (temporal and spatial) resolution regional NWP model will be developed in the next few years. The NWP-ZTD integrated from the new regional NWP model will have a better precision and will be more effective for the improvement of the NWP-ZTD.

Chapter 6 Positioning Experiments based on Regional NWP models

6.1 Introduction

In recent years, using numerical weather prediction (NWP) models for static and kinematic positioning has been proposed by many researchers for the purpose of minimizing the size of the residual tropospheric error (Pany et al., 2002; Behrend et al., 2001, Jensen et al., 2002; Boccolari et al., 2006; Nordman et al., 2007). Nie (2010) get ZTD from CORS network estimation and from the traditional models (mainly Saastamoinen model and Hopfield model), used for the PPP. Three different ways are compared in the coordinates of WUHN station in the rainy days, the traditional model used in PPP directly without ZTD estimation, the traditional model with ZTD estimation, and the CORS network result used directly without ZTD estimation, the RMSE of the up-component is about 50 cm, 13 cm, and 14 cm, respectively.

In this chapter, the integrated NWP-ZTD will be first used directly as the true values for tropospheric correction of GPS signal. In addition, the baseline consistency with the regional GPS network using such a method will be compared with the use of a conventional positioning method. Then, we propose a new instantaneous search method for the tropospheric delay estimation based on the GNSS carrier phase measurements. This new method can be directly applied to high-precision, real-time positioning algorithms. The experiments and the analysis of the results will be shown, as well some discussions and conclusions.

6.2 Coordinate consistency for daily solution experiment

The Zenith Total Delay (ZTD) was estimated from the GPS data and the integration from the NWP data in July 2011. Both the GPS-ZTD and NWP-ZTD are for every hour each day. The regional NWP used is the STI-WARMS Medium-Range Numerical Weather Prediction model, which was introduced in Chapter 3. All the baselines are estimated from the daily solution, GPS-ZTD and baselines estimated from conventional methods and are taken to be the referenced results.

The GPS stations used in the experiment are the same as in Chapter 5. Five of the stations are selected for baselines, and only one IGS station, SHAO, is used here. The stations are distributed in Shandong, Jiangsu, Anhui, and Shanghai and are shown in Figure 6.1. The following 15 baselines will be used for the software: 1 BYYH-BXTC, 2 BFYH-SDHM, 3 BFYH-SDJM, 4 BFYH-SHAO, 5 BFYH-SHBS, 6 BXTC-SDHM, 7 BXTC-SDJM, 8 BXTC-SHAO, 9 BXTC-SHBS, 10 SDHM-SDJM, 11 SDHM-SHAO, 12 SDHM-SHBS, 13 SDJM-SHAO, 14 SDJM-SHBS, and 15 SHAO-SHBS.

Two main goals will be shown in this experiment:

- To check the consistency of the baselines when the NWP-ZTD is used directly to eliminate the tropospheric effect; and
- To check the consistency of the baselines when ZTD with different precisions is used as prior values in the GPS measurements.
-

6.2.1 Consistency of baselines with NWP-ZTD

The ZTD from July 2011 are integrated from the NWP models every hour for each day, and then they are interpolated for each observation. The NWP-ZTD will be taken as the true value to eliminate the tropospheric delay directly. Therefore, the ZTD will not be estimated together with coordinates during the data processing.

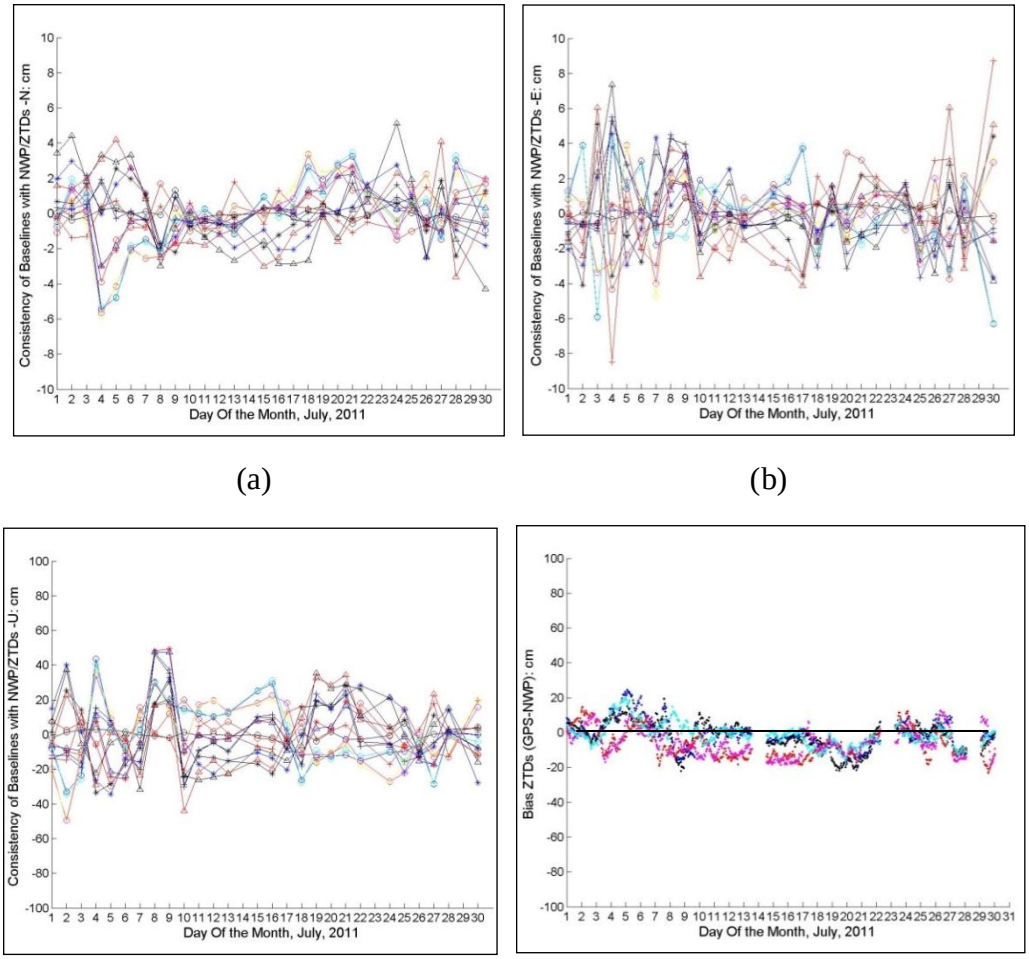

Figure 6.1: The consistency of baselines with NWP-ZTD and the errors of NWP-ZTD

The consistency of baselines is shown in Figure 6.1, and the baseline consistencies in different directions (N, E, U) are shown in (a), (b) and (c), respectively. The statistics for all the baselines are as follows:

	N-directions (cm)	E-directions (cm)	U-directions (cm)
Standard Error	1.63	2.09	17.14

Table 6.1: The baselines consistencies in different directions

The differences in the GPS-ZTD and NWP-ZTD are shown in (d). Compared with Figure 6.1 (c) and (d), the main large errors in the baselines are found to be related to the errors in the NWP-ZTD. The large error of the ZTD from 4-9 July

leads to the large error of the baselines at the same time.

It seems that the accuracy of the ZTD is very important to the precision of baselines. Thus, taking the GPS-ZTD as the true input values, the ZTD will not be estimated together with the coordinates, and the results are shown in Figure 6.2.

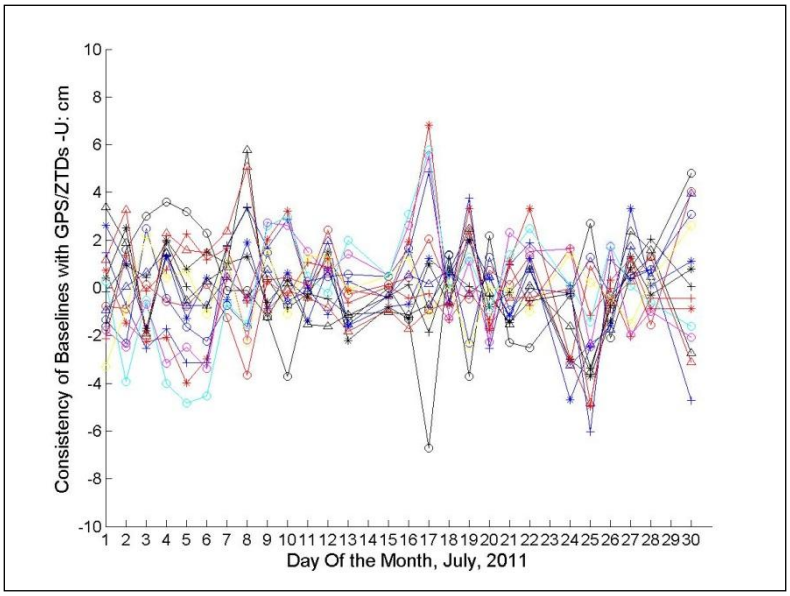

(a)

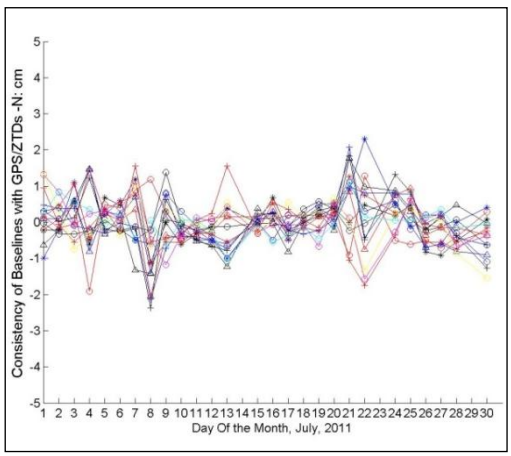

(b)

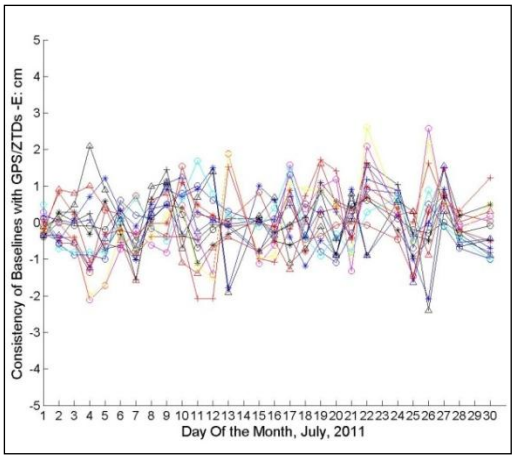

(c)

Figure 6.2: The consistency of baselines with GPS-ZTD

The consistency of the baselines is shown in Figure 6.2, and the baseline consistencies in different directions (N, E, U) are shown in (a), (b) and (c),

respectively. The statistics of all baselines are as follows:

	N-directions (cm)	E-directions (cm)	U-directions (cm)
Standard Error	0.63	0.81	1.90

Table 6.2: The baseline consistencies in different directions

Compared with Figure 6.1 and Figure 6.2, it is shown that if the NWP-ZTD is good enough, the consistencies of the baselines without ZTD estimation could be improved a great deal, both in the horizontal and vertical directions.

6.2.2 Effects of baseline consistency with prior values

The ZTD from the Saastamoinen model, NWP-ZTD and GPS-ZTD are used together as the prior values, and all ZTDs are taken as the unknown values to check if the prior ZTD values could lead to a better consistency in the baselines. Therefore, the ZTD here will be estimated together with the coordinates during the data processing.

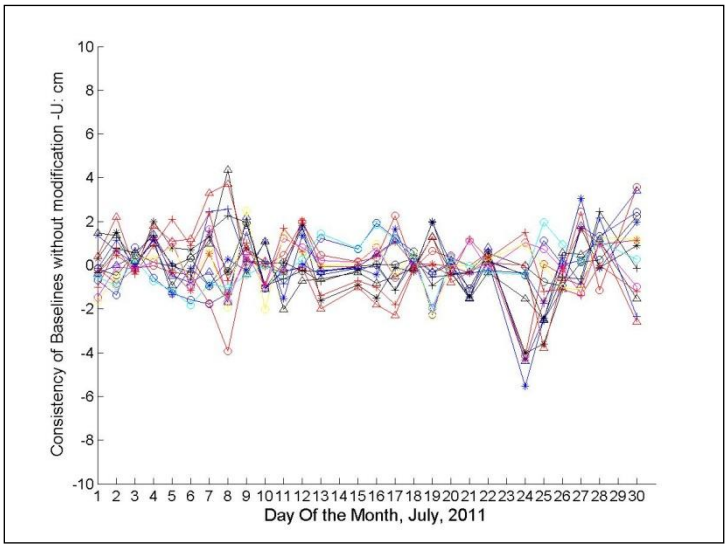

(a)

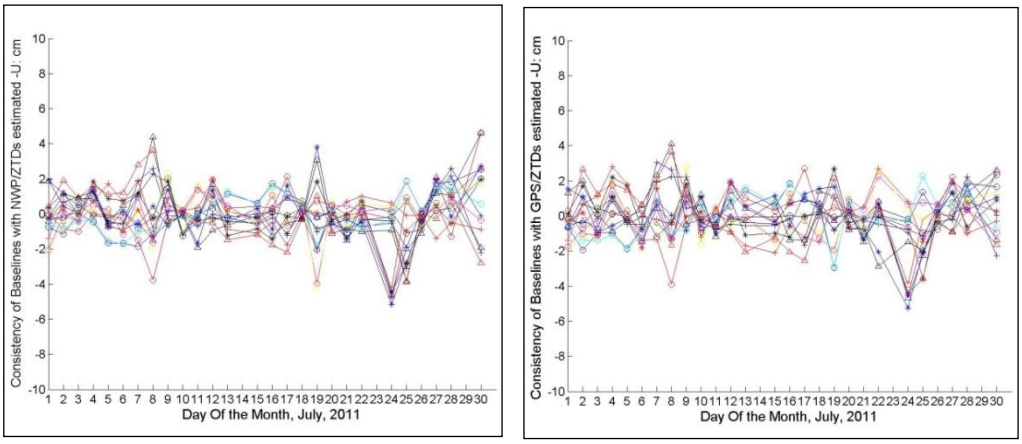

(b) (c)

Figure 6.3: The consistencies of baselines with different ZTDs in the U direction

The baseline consistencies with model ZTD (conventional way), NWP-ZTD and the GPS-ZTD are shown in (a), (b) and (c), respectively. The statistics for all the baselines are as follows:

Prior Values	Standard Error N-directions (cm)	Standard Error E-directions (cm)	Standard Error U-directions (cm)
Model ZTD	0.38	0.63	1.28
NWP-ZTD	0.41	0.65	1.33
GPS-ZTD	0.41	0.69	1.32

Table 6.3: Differences in the baseline consistencies with different prior ZTDs

Compared with Figure 6.3 (a), (b) and (c), no improvement of baseline consistency in the U direction is shown by using the prior ZTD values.

Comparing Tables 6.1 and 6.2, it is shown that while the GPS-ZTD are used directly, and not estimated in the measurement, the consistencies of the baselines could still achieve the similar precision as the conventional method, within 1-2 cm in the vertical direction. If the NWP-ZTD is taken as the prior value in the GPS positioning, it will not show a significant improvement in the coordinates.

6.3 The Instantaneous Search Method for positioning

In the former experiment, if the tropospheric effect was eliminated directly by using the NWP-ZTD, it cannot achieve high-precision positioning. If the NWP-ZTD is only taken as the prior value, the tropospheric effect is also taken as the unknown parameter in the positioning, and the convergence time will not be cut down. Therefore, we develop a new instantaneous search method based on the NWP-ZTD. The tropospheric delay will be estimated for each epoch, and this will make the near real-time, high-precision positioning possible.

6.3.1 The instantaneous tropospheric delay search method

It is well known that the tropospheric delay at different zenith angles are significantly different and a mapping function is commonly used to project the ZTD to different zenith angles. Figure 6.4 shows a typical relationship between a mapping function and the zenith angle (Niell 2000). From this figure, we find that the value of $m(\alpha_i)$ is approximately 1.0 when the zenith angle of the satellites is relatively small (e.g., $\alpha_i < \alpha_0$, $\alpha_0 = 70°$, , for example). In contrast, $m(\alpha_i)$ increases significantly when the zenith angle is very large (e.g., $\alpha_i > \alpha_0$).

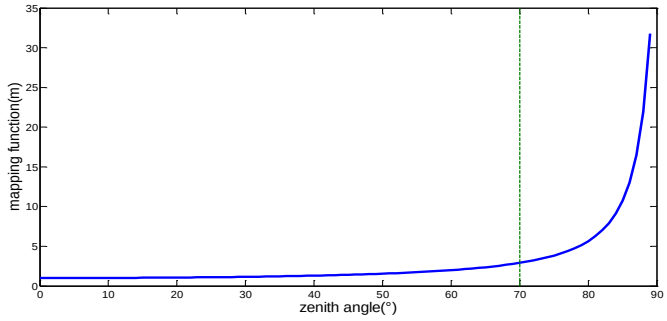

Figure 6.4: The Relationship between the mapping function and zenith angle

Based on this property, we propose a new search method to estimate the

tropospheric delay by employing the GNSS carrier phase measurements.

The general form of the linear observation equations for GNSS positioning can be expressed as follows:

$$AX = L = L_0 + M(\alpha)V_t + e \tag{6.3.1}$$

where A is the design matrix determined by initial satellite and receiver positions, X is the receiver position vector, L is is the pseudo-range and carrier phase observation, and L_0 denotes the measurement vector without error. $M(\alpha)V_t$ is the tropospheric delay error, V_t is the tropospheric delay in the zenith direction, and e is the remaining error vector of the observation.

In Eq. (6.3.1), $M(\alpha)$ is a vector:

$$M(\alpha) = [m(\alpha_1), m(\alpha_2), \dots, m(\alpha_n)]^t \tag{6.3.2}$$

where $m(\alpha_i)$ is the mapping function of the tropospheric delay for each satellite observed, with the zenith angle α_i.

The position vector X can be estimated by the least squares method as follows:

$$\hat{X} = (A^T A)^{-1} A^T L \tag{6.3.3}$$

with the residual vector

$$\hat{V} = (I - H)L \tag{6.3.4}$$

where $H = A(A^T A)^{-1} A^T$.

Without a loss of generality, we arrange the linear observation equation (Eq. (6.3.1)) of different satellites based on the size of the zenith angle, from smallest to the largest.

$$a_i^T X = L_i - m(\alpha_i)V_t, \quad (i=1, \ldots\ldots.,n) \tag{6.3.5}$$

where a_i^T is the row of the design matrix for satellite i.

First, we establish the single difference equation (Eq. (6.3.6)) between the two observed satellites, using the satellite with the smallest zenith angle (α_1) to be the reference satellite.

$$\left(a_i^T - a_1^T\right)X = Li - L1 - (M(\alpha_i) - M(\alpha_1))V_t \tag{6.3.6}$$

Second, we form the single difference equation of the satellite with the second smallest zenith angle (α_2):

$$(a_2^T - a_1^T)X = L2 - L1 - (M(\alpha_2) - M(\alpha_1))V_t \tag{6.3.7}$$

With the current GNSS satellite constellations (i.e., GPS, BeiDou, and GLONASS), the satellites can be roughly homogeneously distributed in sky. Thus, it is not difficult to find two satellites with small zenith angles. From Eq. (6.3.7) we can see that the second term on the right side is approximate to 0, when α_2 is very close to α_1, as the mapping functions with small zenith angles have similar values (see Figure 6.4). This means that Eq. (6.3.7) is basically not affected by the tropospheric delay. Additionally, as both satellites have relatively high elevation angles, Eq. (6.3.7) will mainly affect the estimation of the vertical component.

Third, we select the single difference equation of all satellites with zenith angle (α_j) larger than α_0 to form a single difference:

$$\left(a_j^T - a_1^T\right)X = Lj - L1 - \left(M\left(\alpha_j\right) - M(\alpha_1)\right)V_t, \text{ j=k, …, n} \qquad (6.3.8)$$

Comparing Eqs. (6.3.7) with (6.3.8), we find that the former will not vary considerably, no matter what V_t is chosen. However, the variation of V_t will have a significant effect on Eq. (6.3.8) due to the large difference between the mapping functions $M\left(\alpha_j\right)$ and $M(\alpha_1)$. Even this variation is imperceptible.

Fourth, by solving the position vector X from Eqs. (14) and (15) with a given $\widehat{V_t}$, we can calculate the residual of Eq. (6.3.7):

$$V_2 = (L2 - L1) - (M(\alpha_2) - M(\alpha_1))\widehat{V_t} - (a_2^T - a_1^T)\widehat{X} \qquad (6.3.9)$$

Assuming V_{t0} is the correct tropospheric delay in the zenith direction, when $\widehat{V_t} < V_{t0}$, the right side of Eq. (6.3.8) will increase significantly. As a result, the height component of $\widehat{X}$ will be pulled down heavily, which will cause the residual (Eq. (6.3.9)) of observation Eq. (6.3.7) to be negative. Conversely, if $\widehat{V_t} > V_{t0}$, the right side of Eq. (6.3.8) will decrease remarkably. The height component of $\widehat{X}$ will be pulled up, and the residual of Eq. (6.3.9) will be positive.

Based on this property, we can first define a search range for V_t first. Then, the V_t value in the search range, which corresponds to the residual V_2 for Eq. (6.3.9) of zero, is the tropospheric delay for the epoch. This search method can be summarized as follows:

We choose the satellite with the smallest zenith angle (α_1) as the reference

satellite, and then construct Eqs. (6.3.7) and (6.3.9).

We search for $\widehat{V_t}$ in a certain range of b (i.e., within 20 cm) with a given search step D, $V_t \in (-b, b)$. If V_2 in Eq. (6.3.9) is approximately equal to zero when $\widehat{V_t} = -b + S * D, S \epsilon Z$, this V_t is identified as the tropospheric delay in the zenith direction for the epoch.

Again, this search method only needs one epoch of data to estimate the tropospheric delay. As the high-low satellite combinations (Eq. (6.3.7) and (6.3.8)) are used for parameter estimation, the satellite geometry is generally very strong for the parameter estimation. The accuracy of the ZTD estimation using this method should be equivalent to the accuracy of the measurement, as this method forces the residual V_2 to be zero and the size of the tropospheric estimation error should be equal to the true size of the residual.

- **Experiment design**

To evaluate the ZTD estimation accuracy of the search method proposed in this paper, an experiment was designed. Using observations from several GNSS stations, we can estimate the tropospheric delays at the stations using a conventional GNSS tropospheric delay estimation method (Liu and Li 2013). Then, we use one station as a reference station and try to obtain the station coordinates and ZTDs of the other stations using the methods proposed in this paper. For simplicity, the ambiguities are fixed in the data processing. Finally, we compare the ZTD estimations from the search method and the conventional method to evaluate the accuracy of the search method.

For example, the double differences observation equation is formed between two stations (k_1 and k_2) and two observed satellites (i and 1) as follows:

$$AX + \left[\left(M(\alpha_i)V_t^{k_2} - M(\alpha_1)V_t^{k_2}\right) - \left(M(\alpha_i)V_t^{k_1} - M(\alpha_1)V_t^{k_1}\right)\right] + BN_{i,1}^{k_1,k_2} = L_{i,1}^{k_1,k_2} + e_{i,1}^{k_1,k_2} \quad (6.3.10)$$

where $N_{i,1}^{k_1,k_2}$ is the double difference ambiguity, B is the corresponding design matrices, $L_{i,1}^{k_1,k_2}$ is the double difference carrier phase observation, and $e_{i,1}^{k_1,k_2}$ are the remaining errors of $L_{i,1}^{k_1,k_2}$. Let the station k_1 be the reference station. By removing the reference station tropospheric delay terms (which can be obtained from a conventional ZTD estimation method) and ambiguity, Eq. (7.3.1) becomes the following:

$$AX = Lw - \left(M(\alpha_i)V_t^{k_2} - M(\alpha_1)V_t^{k_2}\right) + e_{i,1}^{k_1,k_2} \quad (6.3.11)$$

where $Lw = L_{i,1}^{k_1,k_2} - BN_{i,1}^{k_1,k_2} + \left(M(\alpha_i)V_t^{k_1} - M(\alpha_1)V_t^{k_1}\right)$.

It can be seen that Eq. (6.3.10) has the same form as Eq. (6.3.11) and therefore the method proposed in this paper can be directly used to estimate the ZTD $V_t^{k_1}$.

- **Test results**

Data used in this study were 24-hour GPS observations (Oct. 2, 2012) from three GNSS reference stations (HKSS, HKWS and HKFN) from the Hong Kong Satellite Positioning Reference Station Network (SatRef). The observation interval was set to 30 seconds. In the data processing, HKSS was regarded as the reference station, and the baselines between the reference station and HKSW and HKFN were 3.9 km and 8.8 km, respectively. In the data processing, we first fixed the double difference ambiguity and estimated the zenith total tropospheric delay (ZTD) of all three stations using the conventional GPS post-processing

method. The Zenith Dry Delay (ZDD) was computed based on the NWP data, the error of the ZDD was very small, and thus we neglected it in the test. The remaining zenith wet delays (ZWD), which were residual from the NWP model, were considered to be the unknown parameters in this test.

Figures 6.5 and 6.6 show the zenith wet delays (ZWD) for the observation period for the two "user" stations (HKWS and HKFN), estimated with the conventional post-processing method for comparison purposes. From these figures we can see that the ZWDs of these two stations varied between 0.15 m to 0.22 m.

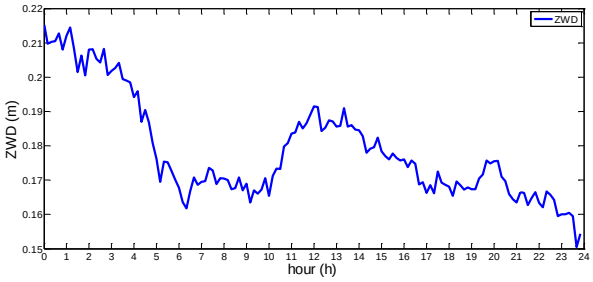

Figure 6.5: Zenith wet tropospheric delay of station HKWS

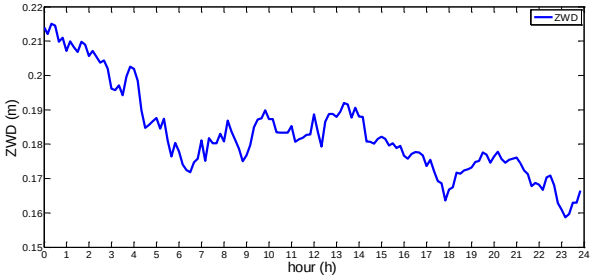

Figure 6.6: Zenith wet tropospheric delay of station HKFN

To determine the initial value and the search range of the ZWD, we defined the NWP-ZWD as the initial value, and computed the difference between the NWP-ZWD and GPS estimated using ZWD. The RMSE is given in Table 6.4 (uncorrected RMSE). This RMSE (38 mm) is chosen for the search range. We applied the search method proposed in this paper to correct the ZWD from the

NWP for both stations. To show the variations of the residual V_2 (Eq. (6.3.9)) from the search method, we plotted the changes in V_2 against different V_t values at two different epochs (00:10:00 and 00:40:00) and at two different stations, as shown in Figures 6.7 and 6.8. The search step of 1 mm is used. We can clearly see that the residual V_2 is increased with the increase in V_t values, from negative to positive. In Figure 6.7, the corresponding ZWD is 0.212 m with a V_2 equal to zero. The difference between this estimation and the one from the conventional method is only 4 mm. Similar results for another epoch can be seen in Figure 6.8.

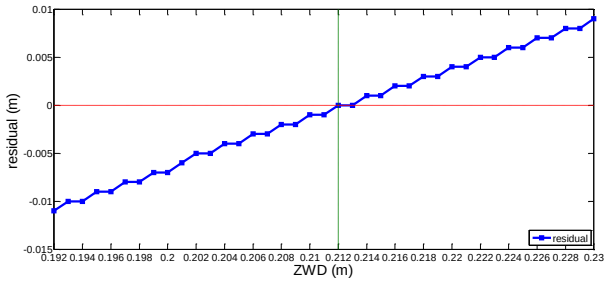

Figure 6.7: The residuals of V_2 under different ZWDs at station HKWS at 00:10:00

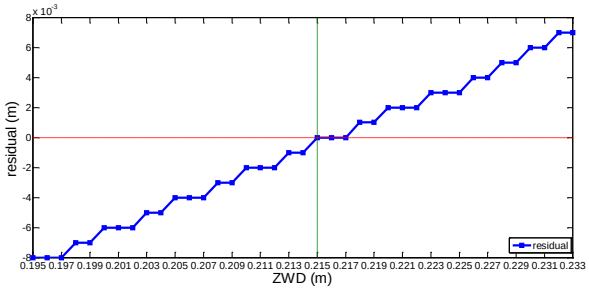

Figure 6.8: The residual of V_2 under the different ZWDs at station HKFN at 00:40:00

In the data processing, we estimated the ZWD every 10 minutes and compared these values with the corresponding values from the conventional post-processing method. Figures 6.9 and 6.10 show the ZWD estimation differences between the proposed method and the conventional post-processing method. The RMSE value for the proposed method is shown in Table 6.4. In the experiment, by using the search method proposed in this paper, the tropospheric

delay estimation accuracy can reach 10 mm, which is comparable to the conventional method. On the other hand, only one epoch of data is required to precisely estimate the tropospheric delay for the proposed search method.

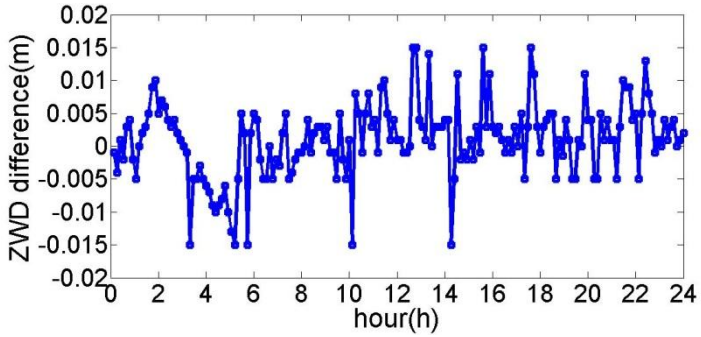

Figure 6.9: ZWD errors of the search and estimate method at station HKWS

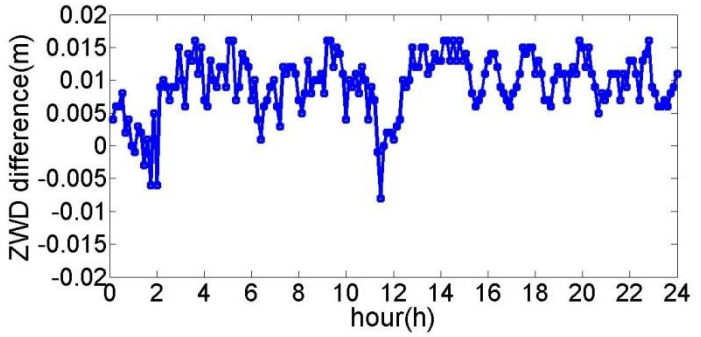

Figure 6.10: ZWD errors of the search and estimate method at station HKFN

Station Name	uncorrected	Search method
HKWS	33	11
HKFN	34	12

Table 6.4: RMSE of the ZWD error of the search and the NWP integrated method (uncorrected) at stations HKWS and HKFN (unit:mm)

Based on the analysis of the residual properties of the GNSS observation equation and the characteristics of the mapping function, we proposed a new method for the instantaneous tropospheric delay search method. The method can be used for fast tropospheric delay estimation with single epoch GNSS observation. The tropospheric delay estimation accuracy is the same as that of

the GNSS measurements used for the processing. To examine the performance of this method, experiments are carried out based on the GNSS observations collected from the Hong Kong SatRef network. The results show that 10 mm accuracy for ZTD estimation can be achieved for the method, which is nearly compatible to the accuracy achieved using the conventional GNSS tropospheric delay estimation but with a much shorter period.

In the data processing, we resolved the integer ambiguities and removed them from the double difference observation equation to evaluate the ZTD estimation accuracy from the new method. In the GNSS RTK positioning, the proposed ZTD estimation method can be integrated using the ambiguity search process to estimate both the ambiguities and ZTD at the same time.

6.3.2 Ionospheric Delay Search Technique for Long-range RTK

The long-range baseline suffers from significant ionospheric delays, especially at low latitudes (Zhu et al. 2004; Shu et al., 2009). The ionospheric delay search technique for long-range RTK that is used in this experiment will also be introduced.

The linearized carrier phase observation model for long baselines at the DD level can be rewritten as follows:

$$\Delta\Phi_i = AX + CT - \lambda_i \Delta N_i - \beta_i \Delta\delta_{I_1} + \sigma_{\Delta\Phi_i} \tag{6.3.12}$$

where $\Delta\Phi_i$ is the DD geometric distance between the satellite and receiver, X is the unknown vector of the baseline components, and A is the design matrix corresponding to X. T is the vector of the zenith tropospheric delay, and C is the design matrix corresponding to T. λ_i is the wavelength of the signal, and ΔN_i is the vector of the float ambiguity estimations. β_i is the ionospheric scale

factor defined with respect to the first-order ionospheric delay on the L_1 carrier ($\Delta\delta_{I_1}$). $\sigma_{\Delta\Phi_i}$ is the DD phase observation noise of the triple-frequency observation.

Applying the least squares estimation, the objective function to be minimized in the integer least squares problem, Ω_i (Teunissen et al., 1998) is given as follows:

$$\Omega_i = \left(\Delta\widehat{N}_i - \Delta N_i\right)^T Q_{\Delta N_i}\left(\Delta\widehat{N}_i - \Delta N_i\right) \qquad \Delta N_i \epsilon\, \mathbb{Z}^n, i = 1,2,3 \tag{6.3.13}$$

where $\Delta\widehat{N}_i$ are the integer ambiguity candidates selected from the ambiguity search space. $Q_{\Delta N_i}$ is the variance-covariance matrix of the float ambiguity estimates and n is the number of the carrier phase observations.

From Eq. (6.3.12), we can see that once the ambiguity parameters are obtained, the ionospheric delay can be derived from the geometry-free combination as follows:

$$\hat{I}_{ij} = \left(\frac{f_j^2}{f_i^2 - f_j^2}\right)[\lambda_i\Phi_i - \lambda_j\Phi_j - (\lambda_i\widehat{N}_i - \lambda_j\widehat{N}_j)] \tag{6.3.14}$$

If we have computed a search space for the DD ambiguity parameters, a pair of ambiguity parameter candidates can be selected in the search space. Then, we can estimate the DD ionospheric delay with Eq. (6.3.14). Each ambiguity candidate provides its corresponding ionosphere observable. According to Eq. (6.3.14), the estimation of the DD ionospheric delay is not affected by the DD tropospheric delay and the position parameters. Once we have a new ionosphere observable, we can estimate a new float ambiguity estimate and its

corresponding variance-covariance matrix, which are free from the effects of the ionospheric delay. Our goal is to find the ambiguity candidate with the minimum Ω_i in Eq. (6.3.13).

One issue with this DD ionospheric delay search method is that the ionosphere observable will be affected by the observation noise. The observation noise is enlarged by approximately 2 times, except the L_2-L_3 and B_3-B_2 combinations. Since most of the GPS satellites do not support triple-frequency signals, the best combination for the DD ionospheric delay search technique is L_1-L_2 for GPS and B_1-B_2 for BDS (Xu et. al, 2015).

6.3.3 The workflow of the TSAR method

Both the modernized GPS and BDS systems provide triple-frequency signals, which are expected to provide great benefits to the ambiguity resolution for the long-range baseline (Feng et al., 2007; Ji et al., 2010). A new triple search ambiguity resolution method (TSAR) for long-baseline RTK operation was developed by Xu et al. 2015. In this TSAR method, the tropospheric search technique introduced in Section 6.3.1 will be applied. The error of tropospheric delay is estimated with other errors, and the NWP-ZTD results are used as the initial value of the tropospheric delay.

The main steps of the methods are as follows:

1) The predicted meteorological data is collected in NWP mode, and the data is used to compute the NWP-ZTD, NWP-ZDD and NWP-ZWD over the following few hours.

2) Fix the ambiguity of the triple-frequency optimal combinations to Extra-Wide Lane (EWL) and Wide Lane (WL). Take the NWP-ZTD as the known tropospheric delay, estimate the ionospheric delay as a parameter, together with the coordinates and ambiguities, thus adopting the least squares adjustment using the original observation. Fix the ambiguity of EWL

and WL with the methods reported in Xu et al. 2015.

3) Calculate the ambiguity search space using the LAMBDA method (Teunissen 1995) for L_1, L_2, L_5 (GPS) or B_1, B_2, B_3 (BDS) with the observation equations below (Eq. (6.3.15)). In this equation, the EWL and WL carrier phase observation, together with the fixed integer ambiguity, are regarded as precise pseudo-range observations. v_{ϕ_i} is the residual vector of the triple-frequency carrier phase measurement. K_{ewl} and K_{wl} are the coefficient matrices of the EWL and WL combination. The ambiguity candidates are sorted according to the sum values of the residuals, V^TPV.

$$\begin{bmatrix} v'_{ewl} \\ v'_{wl} \\ v_{\phi_i} \\ v_{\hat{N}_{ewl}} \\ v_{\hat{N}_{ewl}} \end{bmatrix} = \begin{bmatrix} B & 0 \\ B & 0 \\ B & \lambda_i \\ 0 & K_{ewl} \\ 0 & K_{wl} \end{bmatrix} \begin{bmatrix} X \\ N \end{bmatrix} - \begin{bmatrix} l'_{ewl} \\ l'_{wl} \\ l_i \\ \hat{N}_{ewl} \\ \hat{N}_{wl} \end{bmatrix} \tag{6.3.15}$$

4) Select a pair of ambiguity candidates from the search space, and then eliminate the ionospheric delay of L_1, L_2, L_5 employing the geometry-free combination (Eq. 6.3.14).

5) As the ambiguity and the ionospheric delays are known, the observation equations can be rewritten as follows:

$$BX + CT = l_i + \beta_i \cdot \Delta\delta_{I_1} \tag{6.3.16}$$

where X is the vector of the baseline component and T is the residual zenith tropospheric delay. Search $\hat{T}$ in a certain range b (i.e., within 20 cm) with a given search step D, $\hat{T} \in (-b, b)$. If the sum values of the residuals V^TPV of Eq. (6.3.16) are the minimum, when $\hat{T} = -b + S * D, S \epsilon Z$, this $\hat{T}$ is identified as the tropospheric delay in the zenith direction for the epoch.

6) Once we have a new ionosphere and troposphere observable, we can estimate a new float ambiguity estimate. This new float ambiguity and the corresponding variance-covariance matrix are nearly free from the effects of both the ionospheric and tropospheric delays. Obviously, each pair of ambiguity candidates gain their own corresponding variance-covariance

matrices. Save the value of the corresponding Ω_i, , and find the ambiguity candidate with the minimum and second minimum of Ω_i.

7) When the R-ratio is larger than 2.5, fix the ambiguity with the minimum Ω_i. Otherwise, repeat steps 1-7 until the R-ratio is larger than 2.5.

The detailed flow chart is shown in Figure 6.11.

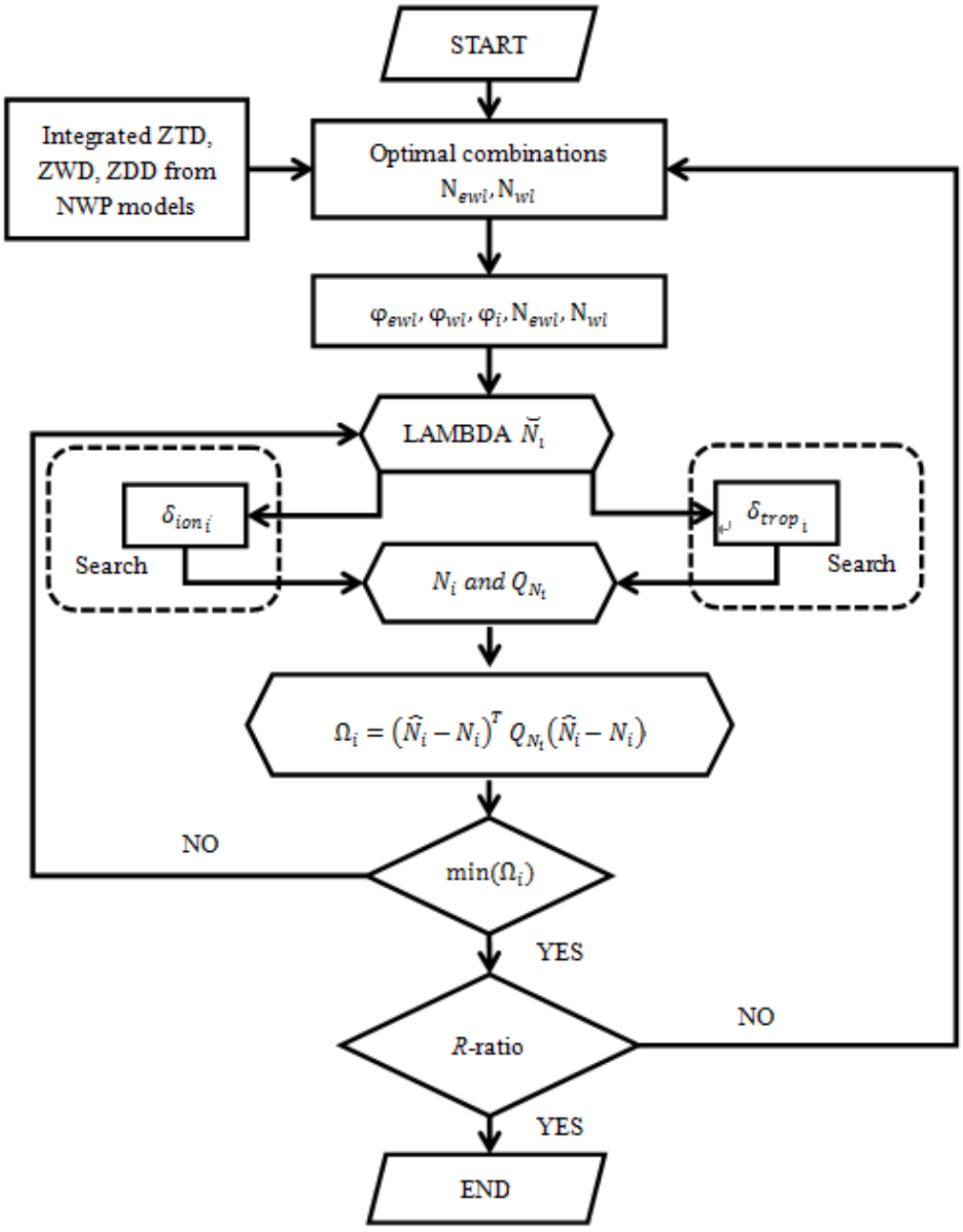

Figure 6.11: The flow chat of the triple search ambiguity resolution method

6.3.4 Experimental design and results

The FAIRT algorithm for tropospheric delays discussed in Chapter 3 could be used to integrate the ZTD from the NWP model. When the algorithm is used for slant path along the GNSS signal, the STD will also be integrated. To check how the integrated tropospheric delays and corrected delays play for the AR in the long-baseline positioning, the NWP-ZTD, NWP-STD and tropospheric search method for the NWP-ZTD correction will be used to eliminate the tropospheric effects in the AR experiment. The stations BXTC, BTLU and BFYH in Jiangsu and Anhui in East China are used for the test. The distribution of stations is shown in Figure 5.7 in Chapter 5, and the length of the baseline for BTLU-BXTC and BTLU-BFYH is approximately 300 km.

The dual-frequency GPS observations of three stations are collected during the dry season (Jan. 24-26) and the rainy season (Jul. 26-28) in 2010. The sample interval is 30 seconds, and the data are processed independently for each single epoch. For a better AR performance, the cut angle of observations is set to 15 °. Five schemes are set for the experiment to check the convergence time for the AR.

1) **No-NWP:** The tropospheric delays are set as the **unknown** parameters and are estimated together with coordinates and ambiguities in the positioning.

2) **NWP-ZTD:** The NWP-ZTD is integrated from the NWP model, **without any correction**. The integrated NWP-ZTD is taken as the **known** parameter, and used to eliminate the tropospheric delay directly in the positioning.

3) **Src- ZTD:** The NWP-ZTD is integrated from the NWP model. The NWP-ZTD and **tropospheric search method** are used to eliminate the

tropospheric delays in the ambiguity search.

4) **Fix- ZTD:** The NWP-ZTD is integrated from the NWP model, and **corrected by a 300 km GPS network and ground MET observations**. The corrected NWP-ZTD and **tropospheric search method** are both used to eliminate the tropospheric effects in the positioning.

5) **STD:** The NWP-STDs are integrated from the NWP model directly, and the mapping functions are NOT used for the ZTD mapping of the slant delays. Others are completed the same way as the scheme 'NWP-ZTD'.

The integrated NWP-ZTD from the NWP model is used for the experiment. The precision of the NWP-ZTD for the 3 stations is vital to the experimental results; therefore, this will be analyzed first. As defined in Chapter 5, the errors are the differences between the NWP-ZTD and ZTD estimated from the post GPS solution. The RMS errors of the NWP-ZTD for the 3 stations are listed in Table 6.5. The DD will be completed for the stations during the data processing, so the RMS errors of the NWP-ZTD at the DD level for two baselines are also shown in Table 6.6.

Station	RMSE of NWP-ZTD (mm)			
	Jan. 24-28		Jul. 26-29	
	Uncorrected	Corrected	Uncorrected	Corrected
BFYH	16.48	9.65	32.66	19.00
BXTC	20.00	12.03	32.91	14.74
BTLU	22.34	13.60	19.36	11.94

Table 6.5: The RMSE of NWP-ZTD for 3 stations

Baseline	RMSE of Double Difference NWP-ZTD (mm)	
	Jan. 24-28	Jul. 26-29

	Uncorrected	Corrected	Uncorrected	Corrected
BFYH-BTLU	19.03	11.76	32.10	18.80
BXTC-BTLU	13.75	9.61	28.61	15.69

Table 6.6: The RMSE of NWP-ZTD at DD level for two baselines

The precision analysis shows that the NWP-ZTD is relatively good during the dry season, and bad during the rainy season. As reported in Chapter 5, the GPS networks with 300 km resolution are used to correct the NWP-ZTD of the 3 stations. The precision of the NWP-ZTD is improved by approximately 30% after correction.

The NWP-ZTD and NWP-ZTD corrected by GPS are both used to eliminate the tropospheric effects directly in the long-baseline RTK. Additionally, the NWP-ZTD corrected by the tropospheric search method and NWP-STDs are used for AR in the positioning. The convergence time for the ambiguities search using 5 different schemes are shown in Figure 6.12 and Table 6.7.

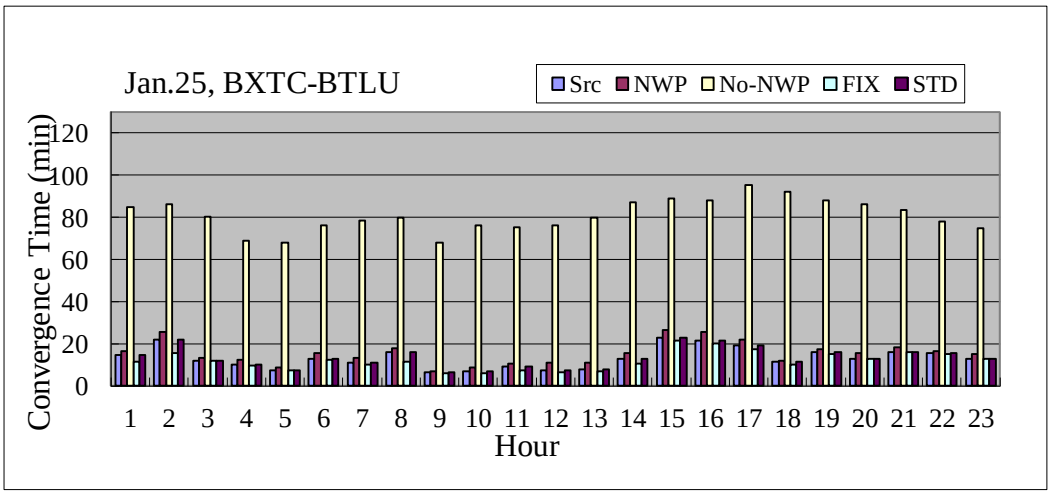

(Jan. 25, 2010 for baseline BXTC-BTLU)

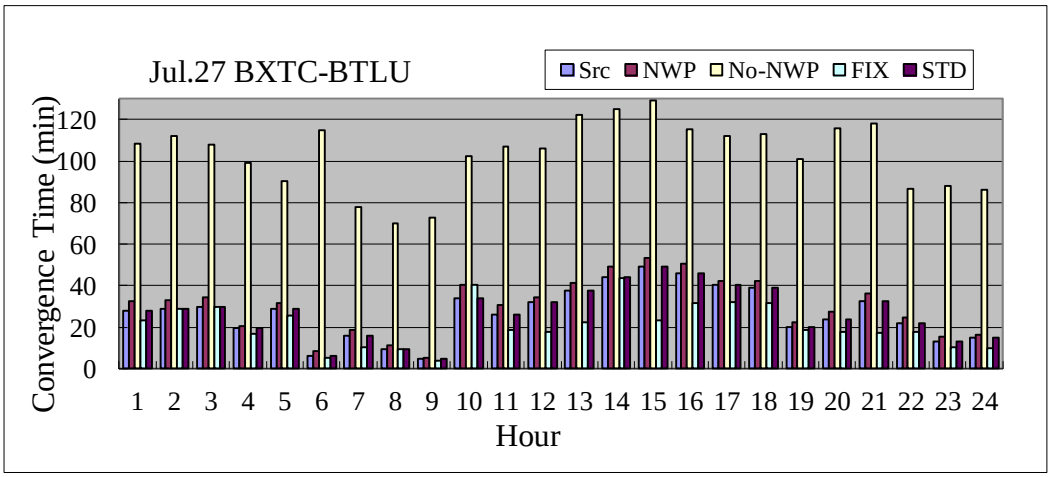

(Jul. 27, 2010 for baseline BXTC-BTLU)

Figure 6.12: The convergence time of AR in 2010 for baseline BTLU-BXTC

Baseline	Day	Mean time for Ambiguity Resolution				
		No-NWP	NWP-ZTD	Src-ZTD	Fix-ZTD	STD
BTLU-	Jan. 24-26	90.757	15.528	13.236	12.111	13.215
BXTC	Jul. 26-28	94.271	22.083	19.042	15.896	19.035
BFYH	Jan. 24-26	87.910	15.236	12.660	12.235	12.646
-BXTC	Jul. 26-28	103.174	18.854	15.674	14.236	15.667

Table 6.7: The convergence time of AR in 2010 for baseline BTLU-BXTC and BFYH-BXTC

The long-baseline RTK experiments are completed for the two baselines, BTLU-BXTC and BFYH-BXTC and are completed during different seasons. The GPS observations are processed for each epoch, and the ambiguity searches are completed for each hour. The convergence times of AR for 24 hours on Jan. 25 and Jul. 27 are shown in Figure 6.12. The statistics of the mean convergence time for the two baselines during different seasons are listed in Table 6.7. We could see that if the AR was completed without NWP-ZTD, the convergence time of AR would be more than 90 minutes. With NWP-ZTD, the convergence time of AR is cut down to 15-20 minutes, even during the rainy season. This will make the real-time, long-range GNSS positioning possible.

In the scheme ‘Src-ZTD’, when the tropospheric search method was used in the AR research, the convergence time is cut down to approximately 2 minutes. The tropospheric search method is used in the schemes ‘Src-ZTD’ and ‘Fix-ZTD’, when NWP-ZTD is improved before the search method, the convergence time is cut down to 1-5 minutes, depending on the improvement of the NWP-ZTD.

Compared with the results in the schemes ‘NWP-ZTD’ and ‘STD’, the convergence time of AR search is nearly the same. The cutting angle is set to 15 ° to eliminate the effects of multi-path. The mapping function is relatively accurate at the high elevation angle. Therefore, it will not see the obvious improvement when the STD is used in the positioning directly. When the observed satellites are not enough and the cutting angle is set lower, the scheme ‘STD’ will show more improvement.

To check the positioning results of the scheme ‘Src-ZTD’, the 3-day mean RMS errors of the two baselines in the N, E, U directions are provided in Table 6.8. In both the dry and rainy seasons, the RMS errors of the two baselines are at the mm-level. The long-baseline positioning results based on the TSAR method and tropospheric search are reliable.

Baseline	Day	Mean RMSE of Baselines (mm)		
		N	E	U
BTLU-BXTC	Jan. 24-28	5.5	4.5	6.4
	Jul. 26-29	6.9	3.6	8.1
BFYH-BXTC	Jan. 24-28	4.5	2.8	6.3
	Jul. 26-29	6.6	4.6	6.2

Table 6.8: The RMSE of baselines in the N, E, U in 2010 for BTLU-BXTC and BFYH-BXTC

6.4 Conclusion

The coordinate experiment was completed in July, the rainy season in East China, which leads to larger errors in the atmospheric parameters of the NWP models than at other times. Therefore, the integrated NWP-ZTD has the worst results here, which is nearly the worst situation of the entire experiment. If the NWP-ZTD are good enough (the same precision as the GPS-ZTD), they could be used directly to eliminate the tropospheric effect, and the consistencies of the baselines could achieve a similar precision as the conventional method. However, the baseline consistency will NOT be improved by the good prior ZTD.

The NWP-ZTD plays an important role in the convergence time for the ambiguity search. With the NWP-ZTD, the convergence time of the AR is cut down from over 90 minutes to 15-20 minutes. When the tropospheric search method and improved NWP-ZTD are used, the convergence time is less than 15 minutes. This makes the real-time, long-range GNSS positioning possible.

Chapter 7 Conclusions and Future Research Plans

7.1 Conclusions

The main purpose of this study is to develop a better tropospheric correction model based NWP models for real-time high precision GNSS positioning. Firstly, the tropospheric delays derived from the latest NWP models are evaluated by GNSS and Radiosonde data, over a period of one year. This is the first time to evaluate NWP model for long period time and in China. A new ray tracing algorithm (FAIRT) is developed in this study to improve ray tracing accuracy and computation efficiency. Based on the analysis of NWP-ZTD errors, further improvements on regional ZTD estimation accuracy are achieved through the integration NWP-ZTD with real-time GNSS and surface meteorological observations in the region. The newly develop tropospheric models are apply in GPS data processing to evaluate the performance improvement on using the new tropospheric models and a new search algorithm is proposed to further improve positioning accuracy and to reducing AR convergence time. Base on this study, the main conclusions are as follows:

- **A new ray tracing algorithm for tropospheric delays (FAIRT method)**

For real-time high precision positioning based on NWP models, accuracy and computation speed are both important to the ray tracing method. A new ray tracing algorithm, named the FAIRT method, is developed for tropospheric delay computation using 3D NWP models. In this method, the bending of GNSS signals is taken into account to improve ray tracing accuracy, and the exponential distribution function of refractivity is used to accelerate the computation. The precision of the delays for the slant path (STD) by the FAIRT method is discussed in the thesis. As a by-product, the accuracy of the existing

mapping functions is evaluated using the new ray tracing method.

- **A precision and reliability analysis for NWP derived ZTD**

The FAIRT method and MET data from regional NWP models are used to integrate tropospheric delays in zenith direction (ZTD). Yearly data from Radiosonde and GPS observations for 8 stations in East China are both used to evaluate the precision of the integrated NWP-ZTD. Compared with observation from Radiosonde, the yearly RMSE of the GPS-ZTD is approximately 20-30 mm in 2010 and 2011. The yearly RMSE of the NWP-ZTD is approximately 25-35 mm, which is almost the same level as that of the GPS-ZTD.

The RMSE differences between the NWP-ZTD and the GPS-ZTD for one year are less than 20 mm, and the monthly error is shown in seasonal changes. The differences in different seasons are significantly different and the larger differences are in the wet seasons. The precision of the NWP-ZTD is highly correlated to the frequency of rainfall. Correlations for the frequency of large NWP-ZTD errors and rainfall for 4 stations in wet seasons are in the range of 0.5 to 0.7.

- **Improvement methods for the ZTD from NWP models**

The accuracy of the NWP derived ZTD can be further improved through the integration with GNSS and surface meteorological measurements. The spatial correction by the GPS network is used to improve the precision of the NWP-ZTD. The precision of the NWP-ZTD, corrected by the GPS network at 250 km, is approximately 20 mm in summer and 10 mm in spring. However, for the NWP-ZTD integrated from MET data with poor precision, the NWP-ZTD cannot be improved through spatial correction; the RMSE of the NWP-ZTD is

over 40 mm in spring after correction.

The temporal correction uses error information from the last observation epoch to improve the NWP-ZTD in the current epoch. The precision of temporal corrections for the NWP-ZTD at a 3-hour resolution is approximately 25 mm in summer and 10 mm in spring, while the precision of the NWP-ZTD within a 1-hour resolution is 20 mm after temporal correction. For the NWP-ZTD integrated from MET data with poor precision, the NWP-ZTD can be improved by temporal corrections well, and the RMSE of the NWP-ZTD is approximately 15 mm in spring after the correction.

A new data assimilation method is developed to correct the NWP-ZTD. In this method, wet pressure observations at the surface with a high temporal resolution are collected for improvement. Using ground data in this assimilation, the model with an empirical factor is used to obtain the ZTD. During the assimilation course, the empirical factor is used as the unknown parameter, and the corrected NWP-ZTD and improved empirical factor are combined together. The RMSE of the NWP-ZTD is less than 15 mm in summer after the correction.

- **The positioning experiments for baseline consistency and ambiguity convergence**

The NWP derived ZTD has been applied in GNSS data processing to eliminate the tropospheric delays in GNSS observations. The horizontal positioning errors are with NWP-ZTD is in centimeter level and the vertical errors in decimeter level. The large errors of NWP-ZTD in wet seasons mainly affect vertical component. If the tropospheric delays are directly estimated from GPS observation, the positioning accuracy is similar with either standard tropospheric model ((i.e. Hopefiled model) or the improved NWP-ZTD model as initial

value.

For GNSS carrier phase processing, a new method is proposed to search tropospheric delays, together with the ambiguity search process. Using NWP-ZTD to define the search range, the ambiguity convergence time can be further improved.

7.2 Future Research Plan

Limited by time-consuming and computing resources, the temporal resolution of the MET data from most regional NWP models is 3 hours. However, for most weather prediction centers (including the Shanghai NWP innovation center in the SMB), higher temporal and spatial regional NWP models will be developed in the next few years (Qi, 2017). The NWP-ZTD integrated from new regional NWP models will have better precision, and the NWP-ZTD will be used more effectively for the GNSS data process.

The positioning experiments performed in the thesis are mainly for the GPS data process. When other GNSS systems are developed, these experiments are can also be performed for those systems, such as Beidou. In addition, only double differenced observations are used in this positioning experiment. In the future, tropospheric corrections based on NWP models can also be used with PPP techniques.

References

Ahn, YW, Lachapelle G, and Skone S, Gutman et al. (2006), Analysis of GPS RTK performance using external NOAA tropospheric corrections integrated with a multiple reference station approach, GPS Solut 10:171-186.

Alber C, Ware RH, Rocken C, and Solheim FS (1997), GPS surveying with 1 mm precision using corrections for atmospheric slant path delay, Geophys. Res. Lett., 24, 1859-1862.

Allen CW (1973), Astrophysical Quantities, 3rd ed., The Athlone Press, Chap. 6, 114-120.

Alves P, Ahn YW, and Liu J et al. (2004), Improvements of USCG RTK Positioning Performance Using external NOAA Tropospheric Corrections Integrated with a Multiple Reference Station Approch, National Technical Meeting, Institute of Navigation, San Diego.

Andrei CO and Chen RZ (2007), Tropospheric delay estimation based on Numerical Weather Model. Cadastre Journal RevCAD, 87-94.

Anthes RA, Rocken C and Kuo YH (2000), Applications of COSMIC to meteorology and climate, Special issue of Terrestrial, Atmospheric and Oceanic Science. 11(1), 115-156.

Ashkenazi V (2006), Geodesy and satellite navigation. Inside GNSS, 1(3), 44-49.

Askne J, Nordius H (1987), Estimation of tropospheric delay for microwaves from surface weather data. Radio Sci , 22, 379-386.

Behrend D, Cucurull L, and Cardellach E et al. (2001), The use of NWP Products in Near Real-Time GPS Data Processing. ION GPS 2001, 11-14 September 2001, Salt Lake City, UT.

Beutler G, Bock H, and Fridez P et al. (2007), Bernese 5 GPS Software user manual. Astronomical Institute, University of Bern.

Bevis M, Bnsinger S, and Herring TA et al. (1992), GPS Meteorolosy: remote sensing of the almospheric water vapor using the Global Positioning System. J. Geophys. Res., 97, 15787-15801.

Bevis M, Businger S, and Chiswell S et al. (1994), GPS Meteorology: mapping zenith wet delay onto precipitable water. J. Appl. Meteoml., 33, 379-386.

Bian S, Jin J, Fang Z (2005), The Beidou satellite positioning system and its positioning accuracy. Navigation, 52(3): 123–129.

Boccolari M, Fazlagic S, and Santangelo R (2006), GPS coordinate estimates by a priori tropospheric delays from NWP using ultra-rapid orbits. Annals of Geophysics, 49, N. 4/5: 881-889.

Bock O, Nuret M (2009), Verification of NWF Model Analyses and Radiosonde Humidity Data with GPS Precipitable Water Vapor Estimates during AMMA. Weather and Forecasting, 24(4), 1085-1101.

Boehm J and Schuh H (2004), Vienna mapping functions in VLBI analyses. Geophys.Res. Lett., 31:L01603, doi:10.1029/2003GL018984.

Boehm J, Werl B and Schuh H (2006a), Troposphere mapping functions for GPS and very long baseline interferometry from European Centre for Medium-Range Weather Forecasts operational analysis data. J. Geophys. Res., 111, B02406, doi:10.1029/2005JB003629.

Boehm J, Niell A, Tregoning P and Schuh H (2006b), Global Mapping Function (GMF): A new empirical mapping function based on numerical weather model data. Geophys. Res. Lett., 33, L07304, doi:10.1029/2005GL025546.

Born M and Wolf E (1980), Refraction and reflection at a metal surface, 6th, Pergamon Press, p122.

Boucher C, Altamimi Z, L Duhem (1994), Results and Analysis of the ITRF93. IERS Technical Note, No. 18, October 1994, Observatoire de Paris.

Braun J etc. (2001), Validation of line-of-sight water vapor measurements with GPS. Radio Sci., 36, 459-472.

Braun J etc. (2003), Comparisons of line-of-sight water vapor observations using the Global Positioning System and a pointing microwave radiometer. Journal of Atmospheric and Oceanic Technology, 2003, 20, 606 ~ 612

Braun J (2004), Remote Sensing of Atmospheric Water Vapor with the Global Positioning System, PhD thesis.

Bruyninx C (2007), Comparing GPS-only with GPS+GLONASS Positioning in a Regional Permanent GNSS Network. GPS Solution 11: 97-106.

Businger S, Ch iswell S R, and Bevis M, et al. (1996), The promise of GPS in atmospheric monitoring. Bulletin of the American Meteorological Society, 77: 5- 18.

Chao CC (1970), A Preliminary Estimation of Tropospheric Influence on the Range and Range Rate Data during the Closest Approach of the MM71 Mars Mission. JPL Tech. Memo 391-129.

Chao CC (1971), Tropospheric Range Effect Due to Simulated Inhomogeneities by Ray Tracing, JPL Tech. Report 32-1526, VI, 57-66.

Chao CC (1972a), A Model for Tropospheric Calibration from Daily Surface and Radiosonde Balloon Measurements, Tech. Memo. Calif. Inst. Technol. JPL, 391-350, 17

Chao CC (1972b), A New Method to Predict Wet Zenith Range Correction from Surface Measurements. JPL Tech. Report 32-1526, XIV, Pasadena, California, 33-37

Chen G, and Herring TA (1997), Effects of atmospheric azimuthal asymmetry on the analysis of space geodetic data. J. Geophys. Res., 102, 20,489-20,502.

Chen M, Zhang P and Zhang JL (2016), The development and application of CORS in China. China Surveying and Mapping. (1), 30-34.

Chen QM, Song SL and Zhu WY (2012), An analysis for the accuracy of tropospheric zenith delay calculated from ECMWF/NCEP data over Asia. Chinese Journal of Geophysics, 55(3), 275-283.

Chen W, Hu C, et al. (2009), Error correction models and their effects on GPS Precise Point Positioning. Survey Review, 41, 313 pp. 238-252.

Collins J P，Laney R B (1997), Final Contract Report Prepared for Nav Canada Department of Geodesy and Geomatics Engineering Technical Repot，University of New Brunswick，Fredericton，N B Canada.

Collins JP (1999), Assessment and Development of a Tropospheric Delay Model for Aircraft Users of the Global Positioning System. Technical Report University of New Brunswick，Fredericton，Canada.

Collins P (2008), Isolating and estimating undifferenced GPS integer ambiguities. In: Proceedings of ION national technical meeting, San Diego, US, pp 720–732

Dach R, Schmid R and Schmitz M et al. (2011), Improved antenna phase center models for GLONASS, GPS Solutions, 15 (1), 49-65.

Davis J, Herring T, and Shapir I et al. (1985), Geodesy by radio- interferometry: effects of atmospheric modeling errors on estimates of baseline lengths, Radio Sci. 20,

1593-1607.

Dragert H, TS James and A Lambert (2000), Ocean Loading Corrections for Continuous GPS: A Case Study at the Canadian Coastal Site Holberg. Geophysical Research Letters, 27, No. 14, pp. 2045-2048.

Eresmaa, R and H Järvinen (2006), An observation operator for ground-based GPS slant delays, Tellus, 58A, 131–140.

European Space Agency (2005c), Galileo – the European program for global navigation services, 2nd edition. ESA Publications Division, Noordwijk, Netherlands.

European Space Agency, Galileo Joint Undertaking (2006), Galileo open service. Signal in space interface control document (OS SIS ICD).

Falcone M (2006), Galileo overall architecture. Course on Galileo held after the 3rd ESA Workshop on Satellite Navigation User Equipment Technologies, NAVITEC 2006, ESTEC, Noordwijk, The Netherlands, December 14.

Feng Y, Rizos C, Higgins M (2007), Multiple carrier ambiguity resolution and performance benefits for RTK and PPP positioning services in regional areas. In: Proceedings of ION GNSS 20th international technical meeting of the satellite division. pp 25–28.

Fjeldbo G, AJ Kliore, and VR Eshelman (1971), The neutral atmosphere of Venus as studied with the Mariner V radio occultation experiments. Astron. J., 76, 2, 123-140.

Gao Y and X Shen (2001), Improving convergence speed of carrier phase based Precise Point Positioning. Proceedings of ION GPS 2001, 12–14 September, Salt Lake City, Utah, pp. 1532–1539.

Gao Y, Shen X (2002), A new method for carrier-phase-based precise point positioning, NAVIGATION J Inst Navig 49(2):109–116.

Ge M, Gendt G et al. (2008), Resolution of GPS carrier-phase ambiguities in Precise Point Positioning (PPP) with daily observations. J Geod., 82: 389-399. doi: 10.1007/s00190-007-0187-4.

Geng J, Teferle FN and Shi C et al. (2009), Ambiguity resolution in precise point positioning with hourly data. GPS Solut., 13(4): 263–270.

Geng J, Meng X, Dodson AH, Teferle FN (2010), Integer ambiguity resolution in precise point positioning: method comparison, J Geod., 84:569-581 doi: 10.1007/s00190-010-0399-x.

Geng J, Teferle FN, Meng X, Dodson AH (2010c), Towards PPP-RTK: Ambiguity resolution in real-time precise point positioning. Adv Space Res. doi:10.1016/j.asr.2010.03.030.

Ghoddousi-Fard R., Dare P., Langley R. B. (2009), A web-based package for ray tracing the neutral atmosphere radiometric path delay. Computers & Geosciences 35 (2009) 1113–1124

Ghoddousi-Fard R, Dare P, Langley RB (2009), Tropospheric delay gradients from numerical weather prediction models: effects on GPS estimated parameters. GPS Solut., 2009, 13:281-291.

Green R. M. (1985), Spherical Astronomy, Cambridge University Press, 87.

Guo P, Yan HJ, and Hong ZJ et al. (2005), The standard retrieval algorithm of neutral atmosphere by GPS occultation. CAA, 29(3), 331-342.

Gutman SI, Benjamin SG (2001), The role ground-based GPS meteorological observations in numerical weather prediction. GPS Solutions, 4(4), pp.16-22.

Hajj, GA, ER Kursinski, and LJ Romans et al. (2002). A technical description of atmospheric sounding by GPS occultation. J. of Atmos. and Sol. Terr. Phys., 64, 451-469.

Han Y, Lv ZW, and Xu J et al. (2017), Retrieval of precipitable water vapor from BDS and GPS observations. Journal of Navigation and positioning, 5(1), 39-45.

Hasse J, Vedel H, and Ge M et al. (2000), Radiosonde and GPS Zenith Total Delay (ZTD) variability in the Mediterranean. COST Acrtion 716 workshop – Towards Operational GPS Meteorology.

Hein GW, Avila-Rodriguez JA, and Wallner S et al. (2006a), MBOC: the new optimized spreading modulation. Recommended for Galileo L1 OS and GPS L1C. Inside GNSS, 1(4): 57–66.

Hein GW, Avila-Rodriguez JA, Wallner S (2006b), The DaVinci Galileo code and others. Inside GNSS, 1(6): 62–75.

Herring TA (1992), Modeling Atmospheric Delay in the Analysis of Space Geodetic Data, in Refraction of Transatmospheric Signals in Geodesy, Proc. of the Symp. Hague, May 19-22, Netherlands Geodetic Commission Publications on Geodesy, New Series No36, 157-164.

Heroux P, Y Gao, and J Kouba et al. (2004), Products and applications for Precise Point

Positioning-Moving towards real-time. Proceedings of ION GNSS 2004, 21–24 September, Long Beach, California, pp. 1832–1843.

Hobiger T, Ichikawa R and Takasu T et al. (2008), Ray-traced troposphere slant delays for precise point positioning. Earth Planet Space, 60, e1-e4.

Hofmann-Wellenhof B, H Lichtenegger and J Collins (2001), GPS: Theory and Practice. Fifth revised. Springer, Wien, New York.

Hofmann-Wellenhof B, Legat K, Wieser M (2003), Navigation – principles of positioning and guidance. Springer, Wien, New York.

Hofmann-Wellenhof B, H Lichtenegger, E Wasle (2008), GNSS – Global Navigation Satellite Systems GPS, GLONASS, Galileo, and more, Springer, Wien, New York.

Hopfield HS (1969), Two-quartic Tropospheric Refractivity profile for Correcting Satellite Data. JGR, 74, 4487~4499.

Hopfield (1971), Tropospheric effects on electromagnetically measured range: Prediction from surface weather data. Radio Science, 6, 357-367.

Hothem L (2006), The GPS modernization program and policy update. Paper presented at the XXIII International FIG Congress, Munich, Germany, October 8–13.

Hotine M (1969), "Mathematical Geodesy", Environmental Science Services Administration Monograph 2, Washington, D.C., 209

Ichikawa R et al. (1995), Estimations of atmospheric excess path delay based on three-dimensional, numerical prediction model data, J. Geod. SOc. Japan, 41,379-408.

Janes HW, Langley RB, and Newby SP (1991), Analysis of tropospheric delay prediction models: comparisons with my-tracing and implications for GPS relative positioning, Bull. Geod., 65, 151-161.

Januszewski J (2009), Visibility and Geometry of Glonass Constellation. Artificial Satellites, 44(2), pp. 53-65.

Jensen A (2002), Investigations on the use of numerical weather predictions, ray tracing, and tropospheric mapping functions for network RTK. In Proceedings of the 15th International Technical Meeting of the Satellite Division of the Institute of Navigation (ION GPS-2002).

Ji S, Chen W, Ding X, et al. (2010), Ambiguity validation with combined ratio test and ellipsoidal integer aperture estimator. Journal of Geodesy 84:597–604.

Ji S, Xu Y and Chen W et al (2014), Comparison of standalone performance between COMPASS and GPS. Journal of Navigation, 1-12.

Kleusberg A (1990), A review of kinematic and static GPS surveying procedures. In: Proceedings of the Second International Symposium on Precise Positioning with the Global Positioning System, Ottawa, Canada, September 3-7: 1102-1113.

Kouba J, Y MireaulL, F Lahaye (1995), Rapid Service IGS Orbit Combination - Week 0787, IGS Report No 1578, IGS Central Bureau Information System

Kouba J, Heroux P (2001), Precise point positioning using IGS orbit and clock products, GPS Solut., 5(2):12–28. doi:10.1007/PL00012883

Kuo YH, X Zou and YR Guo (1996), Variational assimilation of precipitable water using a nonhydrostatic mesoscale adjoint model, Mon. Weather Rev., 124, 122-147.

Kuo, YH, SV Sokolovskiy, RA Anthes, F Vandenberghe (2000), Assimilation of GPS radio occultation data for numerical weather prediction. Terrestrial Atmospheric and Oceanic Science, 11 (1), 157–186.

Kursinski ER, GA Hajj and WI Bertiger et al. (1996a), Initial results of radio occultation observations of Earth's atmosphere using the global positioning system. Science 271, 1107-1110.

Kursinski ER (1997), "The GPS radio occultation concept: theoretical performance and initial results", Ph. D. thesis, CIT, Pasadena, California.

Kursinski ER, GA Hajj, SS Leroy and B Herman (2000), The GPS radio occultation technique, Terrestrial, Atmospheric and Oceanic Sciences (TAO), 11(1), 53-114.

Laurichesse D, Mercier F, and Berthias JP et al. (2009), Integer ambiguity resolution on undifferenced GPS phase measurements and its application to PPP and satellite precise orbit determination. Navig J Inst Navig 56(2):135–149.

Li M; Liu XM; and Feng XG (2015), The Application of the CORS in the Research of Digital Urban Municipal Supervision and Management, Advanced Materials Research, Vols. 1065-1069, pp. 3446-3449.

Li J (2016), Application of the Object-based Verification Method for High Resolution NWP. Desert and Oasis Meteorology, 10 (5), 1-9.

Li X, Ge M, Douša J, Wickert J (2014), Real-time precise point positioning regional augmentation for large GPS reference networks. GPS solutions 18:61–71.

Li X, Zhang X, Ge M (2011), Regional reference network augmented precise point positioning for instantaneous ambiguity resolution. Journal of Geodesy, 85:151–158.

Li XL (2014), Constrution and application of CORS. China University of Geosciences, Master thesis.

Liu Y, Guo P, Liu M (2010), Improvement of Atmospheric Hydrostatic Delay Correction at Low Elevation Angle. ACTA ASTRONOMICA SINCA, 51(3),309-316.

Marini JW (1972), Correction of Satellite Tracking Data for an Arbitrary Tropospheric Profile. Radio Sci., 7, 223-231.

McCarthy DD (1996), International Earth Rotation Service. IERS conventions.

Melbourne WG (1985), The case for ranging in GPS-based geodetic systems. In: Proceedings of first international symposium on precise positioning with the global positioning system, Rockville, US, pp373–386.

Mendes V (1999), Modeling the neutral-atmosphere propagation delay in radiometric space techniques, Ph.D. dissertation. Technical Report 199, Department of Geodesy and Geomatrics Engineering, University of New Brunswick, Fredricton, New Brunswick.

Monico J, Alves D, Dalbelo F, Camargo P, Sapucci L, and Souto Fortes L (2006), Atmospheric models applied to DGPS and RTK network in Brazil: preliminary results. In: Proceedings of the 19th International Technical Meeting of the Satellite Division of the Institute of Navigation (ION GNSS 2006): 1151-1158.

Muellerschoen RJ, YE Bar-Sever, WI Bertiger, DA Stowers (2001), NASA's Global DGPS for High Precision Users.GPS World,12,No.1,pp.14-20.

Nardo A, Huisman L, Teunissen PJG (2014), GPS + GLONASS CORS Processing: The Asian-Pacific APREF Case. International Association of Geodesy Symposia, Vol. 139. Springer, Berlin, Heidelberg

NCAR (2006), Weather Forecast Accuracy Gets Boost with New Computer Model. 25 August.

Niell AE (1996), Global mapping functions for the atmosphere delay at radio wavelengths, J. Geophy. Res., 101(B2), 3227-3246.

Niell AE (2001), Preliminary evaluation of atmospheric mapping functions based on numerical weather models, Physics and Chemistry of the Earth, 26, 475-480.

Nievinski F, Cove K, Santos M, Wells D, and Kingdon R (2005), Range-extended GPS kinematic positioning using numerical weather prediction model. In the Proceedings of ION 61st Annual Meeting The MITRE Corporation & Draper Laboratory: 902-911.

Nie JL, Zhang SC, et al. (2010), Precise Point Positioning Based on Tropospheric Refraction CORS, Journal of Geodesy and Geodynamics, 30(2).

Nordman M, Eresmaa R (2007), Using Numerical Weather Prediction Model Derived Tropospheric Slant Delays in GPS Processing: a Case Study. Geophysica, 43(1–2), 49–57.

Pany T (2002), Measuring and modeling the slant wet delay with GPS and the ECMWF NWP model. Phys. Chem. Earth (A/B/C) 27, 347–354.

Paris DT and Hurd FK (1969), Basic Electromagnetic Theory, McGraw-Hill, New York.

Prasad R, Ruggieri M (2005), Applied satellite navigation using GPS, Galileo, and augmentation systems. Artech House, Boston London.

Qi LB (2015), Operational progress of High-Resolution Numerical Model on severe Convective weather warning. Meteorological Monthly, 41(6), 661-673.

Rashid ZAA, Momani MA, and Sulaiman S, et al. (2006), GPS ionospheric TEC measurement during the 23rd November 2003 total solar eclipse at Scott Base Antarcita. Journal of Atmospheric and Solar-Terrestrial Physics, 68(11); 1219-1236.

Rocken C, R Anthes, and M Exne et al. (1997), Analysis and validation of GPS/MET data in the neutral atmosphere. J. Geophys. Res., 102 (D25), 29849-29866.

Rocken C, JM Johnson, and JJ Braun et al. (2000), Improving GPS surveying with modeled ionospheric corrections, Geophysical Research Letters, 27, 3821-3824.

Rizos C (2006), The research challenges of IAG Commission 4 “Positioning & Applications”. Paper presented at VI Hotine-Marussi symposium of theoretical and computational geodesy, Wuhan 29 May–2 June, 2006.

Rizos C (2007), Alternatives to current GPS-RTK services and some implications for CORS infrastructure and operations, July 2007, Vol. 11; Issue 3, 151–158.

Saastamoinen J (1972a; 1972b; 1973), Contributions to the Theory of Atmospheric Refraction. Bull. Geod., V105-107, 279-298, 383-397, 13-34.

Santos M, Nievinski F, and Cove K et al. (2005), Range-Extended Post-Processing Kinematic (PPK) in a Marine Environment, ION GNSS 18th International Technical Meeting of the Satellite Division, 13-16 September 2005, Long Beach, CA.

Shaw ME (2005), Global Positioning System: a policy and modernization review. Presented at United Nations, International Committee on GNSS, December 1–2.

Sokolovskiy SV (2001), Tracking tropospheric radio occultation signals from low Earth orbit. Radio Sci., 36 (3), 483-498.

Spilker J (1996a), GPS navigation data, Parkinson BW, Spilker JJ(eds): Global Positioning System: theory and applications. American Institute of Aeronautics and Astronautics, Washington, DC.

Spilker J(1996b), GPS signal structure and theoretical performance, Parkinson BW, Spilker JJ(eds): Global Positioning System: theory and applications. American Institute of Aeronautics and Astronautics, Washington, DC.

Shen LL; Wang L; Wu MQ (2013),The Design and Realization of Online Land Patrol System Based on CORS, China Satellite Navigation Conference (CSNC) 2013 Proceedings pp 149-157.

Shen XH, Su Y and Hu JL et al. (2017), Development and Operation Transformation of GRAPES Global Middle-range Forecast System, Journal of Applied Meteorological Science, 28(1), 1-10.

Shu FC, Guo L, and Liu M, et al.(2009), Ionospheric TEC Measurement with VLBI and GPS During the Total Solar Eclipse of 22 July 2009. Review Science and Technology, 27(15). 19-24.

Schueler T (2001), On ground-based GPS tropospheric delay estimation. PhD thesis, University of Bundeswehr, Munchen.

Simth EKJ and Weintraub S (1953), The Constants in the Equation for Atmospheric Refractive Index at Radio Frequencies, Proc. IRE, 41, 1035~1037.

Solheim F, Vivekanandan J, Ware R and Rocken C (1999), Propagation delays induced in GPS signals by dry air, water vapor, hydrometeors, and other particulates, .Z. Geoph. Res., 104, D8, 9663-9670.

Song SL, Zhu WY and Chen QM et al. (2011), Establishment of a new tropospheric delay correction model over China aera. Physics, Mechanics & Astronomy, 54(12), 2271-2283.

Tang JY (2013), Developing and applying analysis of Beidou navigation satellites regional system. GNSS World of China, 38(5), 47-52.

Teunissen PJG, Kleusberg Eds. (1996), GPS for geodesy, 2nd edition. Springer, Berlin Heidelberg New York.

T Teunissen PJG, Kleusberg Eds. (1998), GPS for geodesy, 2nd Ed., Springer.

Thayer GD (1967), A rapid and accurate ray tracing algorithm for a horizontally stratified atmosphere, Radio Sci., 1(2), 249– 252.

Thayer GD (1974), An Improved Equation for the Radio Refractive Index of Air, Radio Sci., 9, 803-807.

Vedel H, Mogensen KS, Huang XY. (2001), Calculation of Zenith Delays From Meteorological Data Comparison of NWP Model, Radiosonde and GPS Delays, Phys. Chem. Earth(A), 26,No. 6-8, pp.497-502.

Wang XL, Ji JX, Li YF (2009), The applicability analysis of troposphere delay error model in GPS positioning. Aircraft Engineering and Aerospace Technology, Vol. 81 Iss: 5 pp. 445 - 451.

Wang XL, Zhang Q and Zhang SC (2017), Using ECMWF and GPS data to research and analyze a typical frontal rain. Journal of Geodesy and Geodynamics. 2017, Vol. 37(5), 478-481.

Wang XY, Zhu WY, et al. (1999), Preliminary Results of Precipitable Water Vaopr Monitored by Ground-Based GPS. Chinese Journal of Atmospheric Science, (23)5, 605-612.

Ware R, M Exner, D Feng, and M Gorbunov et al. (1996), GPS Sounding of the Atmosphere: Preliminary Results. Bulletin of the American Meteorological Society, 77, 19-40.

Wei EH, Liu XX and Liu JN (2017), Accuracy evaluation and analysis of signal Point Positioning with Beidou and GPS, Bulletin of Surveying and Mapping, 5, 1-5.

Witchayangkoon, B. (2000), Elements of GPS precise point positioning, PhD thesis, The University of Maine.

Wübbena G (1985), Software developments for geodetic positioning with GPS using TI-4100 code and carrier measurements. In: Proceedings of first international symposium on precise positioning with the global positioning system, Rockville, US, pp 403–412.

Wubbena G, Bagge A, SchmitzM (2001), Network-based techniques for RTK applications. Paper presented at the GPS Symposium, GPS JIN 2001, GPS Society, Japan Institute of Navigation, November 14-16.

Wu JT, Wu, SC, and Hajj GA et al. (1993), Effects of Antenna Orientation on GPS Carrier Phase. Manuscripta Geodaetica, (18): 91-98.

Xu GC (2003), GPS Theory, Algorithms and Applications. Spring-Verlag Berdelberg, New York. 315 pages.

Xu Y, Ji S, Chen W, Weng D (2015), A New Ionosphere-free Ambiguity Resolution method for Long-range Baseline with GNSS Triple-Frequency signals. Advances in Space Research, 56(8): 1600-1612.

Xu Y (2017), Integration of Multiple-constellation GNSS for Long-rang Real-time Kinematic Positioning. PhD thesis, The Hong Kong Polytechnic University.

Yan HJ (1995), On the Corrections of Tropospheric Refractive Delay (I)：The Classical Theories, Progress in Astronomy, 13(4), 380-391.

Yan HJ (1996), On the Corrections of Tropospheric Refractive Delay (II): The Recent main research topics and progress, Progress in Astronomy, 14(3), 181-191.

Yan HJ (1998), Improvement of astronomical refraction by mapping function, CAA, 22(4), 487-496.

Yan HJ, Lin QC (1999), Possibility of Establishing Global Mapping Function of Atmospheric Refractive Delays. ANNALS OF SHANGHAI OBSERVATORY ACADEMIA SINICA, (20), 61-70.

Yan HJ (2000), The Mapping Function and the Generator Function Theory of Neutral Atmospheric Refraction, Progress in Astronomy, 18(2), 104-113.

Yang YM, Zhu XS, Liu M, et al.(2008), Statistical Analysis of Atmospheric Precipitable Water Vapour Observed by GPS in Yangtze River Delta Region. Plateau Meteorology, 27 Suppl. 150-151.

Yang JM, and Qiu JH (2002), A method for estimating Precipitable Water and effective water vapor content from ground humidity parameters. Chinese Journal of Atmospheric Sciences, 26(1), 9-22.

Yao YB, Zhang S and Kong J (2017), Research progress and prospect of GNSS space Environment science. Acta Geodaetica et Cartographica Sinica, 46(10), 1408-1420.

Ye QX, Yang LH, et al. (2008), Application of GPS/Pwv Data to Forecast Strong Convection Weather in Shanghai, Torrential Rain and Disasters, 27(2). 141-148.

Zamberge JF, DC Jefferson and G Blewitt et al. (1993). "Jet Propulsion Laboratory IGS Analysis Center Report, 1992.", Proceedings of the 1993 IGS Workshop, University of Bern.

Zamberge, J.F., R. Liu (1995a), Densification of the IERS terrestrial reference frame through regional GPS networks. Workshop proceedings, in preparation.

Zumberge (1995b), IGS Annual Report for 1994.

Zumberge JF, Heflin MB, and Jefferson DC et al. (1997), Precise point positioning for the efficient and robust analysis of GPS data from large networks. J Geophy Res 102(B3): 5005–5017.

Zhang XH (2006), The precision analysis for dynamic Precise Point Positioning, GNSS World of China, Vol. (1), 7-11.

Zhu WY, Zhang HP, et al. (2004), Monitoring of Small-scale Ionospheric Heterogeneities Using Local GPS Network. Chinese Journal od Geophysics, 47(6), 942-947.

Zou X, Ge M, Tang W, et al (2013), URTK: undifferenced network RTK positioning. GPS solutions 17:283–293.

Zumberge JF, Heflin MB, and Jefferson DC (1997), Precise point positioning for the efficient and robust analysis of GPS data from large networks. J Geophy Res, 102(B3): 5005–5017.